

GLOBAL WAVEMODES
OF DISSIPATIVE FLUID MODELS
IN STRONGLY THREE DIMENSIONAL PLASMAS:
CALCULATION AND INTERPRETATION.

BEN FYNNEY MCMILLAN

OCTOBER 2004

A THESIS SUBMITTED FOR THE DEGREE OF
DOCTOR OF PHILOSOPHY AT
THE AUSTRALIAN NATIONAL UNIVERSITY

The work presented in this thesis is my own except where explicitly stated otherwise.

A handwritten signature in black ink, consisting of a series of connected, fluid strokes. The signature is positioned below the text and is not clearly legible as a specific name.

1 Acknowledgments

I would like to thank the people who encouraged and helped me during my PhD in rough order of appearance. Firstly, I never would have begun a PhD in plasma physics without Boyd Blackwell's help and encouragement, and his enthusiasm for all things technical and otherwise. Henry Gardner, who I also met before my PhD proper, has been a reliable friend and sympathiser, and offered me a great deal of good advice. Bob Dewar has obviously played a central role, as my main supervisor: his insights into the complexities of plasma physics have been an inspiration. Thanks also go to the kindness and patience of the most far-flung member of my supervisory panel, Robin Storer, who guided my numerical work, and put me up in a beautiful apartment near the beach when I was in Adelaide. Robin started the SPECTOR3D project, and the code described in the thesis contains aspects of the original implementation.

I would like to thank the staff at the APAC national facility who provided us with supercomputer access: Margaret Kahn, in particular, spared no effort to help me when I ran into technical trouble, and David Singleton was also helpful. Some work in the thesis was partially supported by the Australian Research Council. Thanks to Steve Hirshman for the use of the VMEC code. Thanks also to Tony Cooper for use of TERPSICHORE, providing us with the LHD test cases, and for arranging a fleeting visit to Lausanne on short notice.

I would be lost without my friends at the research school, and in particular it is a pleasure to have had the company of David Pretty, Ivan Blajer, Ane Anesland, and all the people from AMPL, SP3, and EME. My last regards go to Johanna, without whom my time here would have been far more lonely.

Contents

1	Acknowledgments	5
2	List of abbreviations	10
3	Introduction	11
3.1	Motivation	11
3.2	Scope of the thesis	12
4	MHD physics in stellarators	15
4.1	The ideal MHD equations	15
4.2	Steady state solutions	16
4.3	General stability theory	18
4.4	Local stability	19
4.5	The case for global stability analysis	19
4.6	Resistive instabilities	20
5	Linear waves in plasma fluids.	23
5.1	Behaviour of non-normal systems: transients.	23
5.2	MHD, Quantum Mechanics, and the short wavelength limit . . .	25
5.3	The semiclassical formalism	27
5.4	Random Matrix Theory	28
6	A Comparison of incompressible resistive MHD limits.	31
6.1	Summary	31
6.2	Introduction	31
6.3	Wavemodes in incompressible MHD limits	33
6.4	Numerical results of varying incompressibility	34
6.5	Generic spectra in resistive MHD	35
6.6	WKB analysis of a small shear equilibrium in the limit $\gamma \rightarrow \infty$.	37
6.7	Characterising the Stokes points	40
6.8	Phase matching: a solution near the singularities	42
6.9	Finding wavemodes	44
6.10	WKB in a small shear incompressible case	45
6.11	Effects of the $\gamma \rightarrow \infty$ approximation	46
6.12	Conclusions	48
7	Spector3D	51
7.1	Introduction	51
7.2	Formulation of Spector3D	52
7.3	Coordinate system and equilibria	53

7.4	Numerical equilibria and interpolation	54
7.5	Integrating the resistive MHD equations	55
7.6	The finite element method applied to linearized resistive MHD	57
7.7	Boundary conditions	60
7.8	Symmetries and mode coupling	61
7.9	Calculation of the matrix elements	62
7.10	Ampere's law	63
7.11	The Equation of motion	64
7.12	Equation of state	65
7.13	Code generation	65
7.14	Solution of the eigenvalue equation	65
7.15	1D test cases	67
7.16	2D test cases: Solov'ev equilibria	71
7.17	Resistive ballooning modes in near axisymmetric devices	73
7.18	Heliotron E	80
7.19	LHD	85
8	Stellarator stability to global kinetic ballooning modes	93
8.1	Summary	93
8.2	Introduction	93
8.3	The ballooning mode formalism	95
8.4	Kinetic corrections to Ideal MHD ballooning	98
8.5	Einstein–Brillouin–Keller quantisation	103
8.6	Quantisation in near-integrable systems	104
8.7	Semiclassical analysis of ballooning modes	105
8.8	An application of the semiclassical theory to the H-1 stellarator	108
8.9	The topology of the Lagrangian surfaces	111
8.10	The integrable case	113
8.11	Box quantisation and the Weyl formula	114
8.12	Applying the Weyl formula to drift stabilised ballooning modes	116
8.13	A quantisation of the mixed regime	117
8.14	Conclusions	121
9	Conclusions	123
9.1	A Review	123
9.2	On the use of linear eigenspectra	124
9.3	On further application and enhancement of Spector3D	125
9.4	On semiclassical approaches to ballooning modes in 3D systems	126
A	The matrix elements of Spector3D	136

B Splining of Equilibrium quantities	144
C Eigenvalue solvers for SPECTOR3D	145
C.1 The Jacobi–Davidson eigenvalue solver	145
C.2 Convergence of the eigenvalue solvers.	147
C.3 Storage costs and computational issues.	149

2 List of abbreviations

CAS3D	A 3D ideal MHD stability code [4].
CASTOR	Complex Alfvén Spectrum of Toroidal Plasmas: A 2-D resistive MHD spectral code [3].
EBK	Einstein–Brillouin–Keller (method): A method for semiclassical quantisation in the integrable limit.
FLR	Finite Larmor Radius: Of a model in which the limit Larmor radius $\rightarrow 0$ is not taken, or of an effect which is absent in that limit.
KAM	Kolmogorov–Arnold–Moser (theorem or tori): see section 8.5.
LHD	Large Helical Device: Currently the largest stellarator in the world, located in Japan.
MHD	Magnetohydrodynamics
NCSX	National Compact Stellarator eXperiment: a heavily optimised low aspect ratio stellarator under construction in the USA.[1]
PIES	Princeton Iterative Equilibrium Solver: see section 4.2.
SPECTOR3D	SPECTrum of TOroidal Resistive 3D plasmas: The linearised resistive spectral code described in this thesis.
TERPSICHORE	A 3D ideal MHD stability code [2].
VMEC	Variational Moments Equilibrium Code: see section 4.2.
WKB	Wentzel–Kramers–Brillouin (method): A semiclassical technique for solving one-dimensional differential equations.

3 Introduction

3.1 Motivation

Maintaining our standard of living requires a vast supply of energy, most of which is provided by fossil fuels. The use of fossil resources will become unviable in the near future, and it is unclear whether any of the current alternatives will be able to make up the shortfall. We must therefore either find new ways of harnessing energy or make drastic changes to the way we live.

Controlled nuclear fusion is a possible technological solution: it promises a concentrated, environmentally sustainable, and economic form of power generation. This prospect has spurred one of the longest focused scientific endeavors in recent history. Currently, the only plausible reactor candidates are based on the magnetic confinement of hot, high density plasmas. These confinement devices can be classified in terms of the shape of the magnetic field used to confine the plasma: we will be concerned not just with the devices known as *stellarators* and *tokamaks*, which are currently the focus of most of the research into magnetically confined plasmas, but hybrid devices which in a sense lie somewhere in between. It seems likely that in the near future a device from one of these subclasses, possibly the proposed ITER tokamak, will produce a sustained burning plasma, and liberate large quantities of nuclear energy with only modest external power input.

The size and complexity of such fusion devices will largely determine the cost per unit energy of fusion power: both size and complexity must be minimised. To fit in well with existing energy infrastructure, it is also desirable for reactors to be relatively small in capacity, and ideally they should produce about as much power as conventional power stations. There are technical barriers to fulfilling these requirements, stemming from plasma physics and from the nuclear engineering of the hardware surrounding the plasma.

A detailed understanding of how these plasmas behave has been shown to be essential to the design of devices and to improvements in fusion performance criteria. However, fusion relevant plasmas are unlikely to ever be completely described in a unified framework derived from first-principles, as they are far more rich and complex than other systems which have traditionally been considered intractable to analysis, like strongly turbulent fluids. Of course, this seldom discourages theorists, especially given the practical demand for a functioning reactor, and much progress has been made. In particular, fluid models of the plasma have been able to explain many of the constraints on plasma performance, and they are the topic of our thesis.

3.2 Scope of the thesis

The thesis investigates the dynamics of three-dimensional magnetically confined plasmas, focusing on the linear behaviour of the plasma about an equilibrium as predicted by fluid models.

Of the many such fluid models relevant to magnetically confined plasma, ideal magnetohydrodynamics (MHD), which models the plasma as a perfectly electrically conductive fluid in a magnetic field, probably gives the most concise expression of the physics which underlies confinement. Due to the simplicity and elegance of its underlying equations, a great deal of analytical and numerical study has been possible even in spatially complex plasmas, like stellarators. However, ideal MHD is only strictly applicable over a narrow range of timescales. It also predicts unphysical behaviours at short length scales, where the lack of any wavelength cutoff allows singularities, which can be particularly troublesome in strongly three dimensional configurations. Including more physics in the plasma model can resolve these limitations, but complicated models are difficult to analyse in strongly shaped geometries. For this reason, it is generally necessary to find a compromise between a good local representation of the plasma behaviour and a good description of the global spatial plasma dynamics. In this thesis we examine the physics of several plasma models which somewhat extend ideal MHD, and explore techniques for the global analysis of these models in spatially complicated plasmas like stellarators.

As background, we first review the basis for linear stability analysis of magnetic confinement devices. Section 4 discusses the theoretical and practical solutions to the equilibrium problem, and the energy considerations which lead to ideal and resistive instabilities. We then examine the relationship between the physical plasma behaviour and the results of normal mode analysis. This might seem trivial, but for both ideal and resistive MHD the relationship is not entirely obvious; features like the *resistive Alfvén paradox* and continuum damping illustrate that the most straightforward interpretation of the MHD spectrum is not adequate. In section 5 we show how this difficulty is related to the non-normality of the MHD spectrum, and the pseudospectrum is discussed as a method for relating the spectrum to the behaviour of the initial value problem.

As an additional motivation for a fully three-dimensional analysis of our wave problem, in section 5.2 we consider what qualitative differences are to be expected between wave analysis in axisymmetric plasmas and fully three dimensional configurations as a result of *wave chaos*. The absence of a continuous symmetry means that the toroidal wave number is no longer a good quantum number and this prevents us from using a simple EBK quantisation based

on exact symmetries to find asymptotically correct eigenmodes. We overview two alternatives to direct numerical calculation for obtaining information about spectra which can be used in the absence of a full set of good quantum numbers: *trace formulae* and *quantum chaos theory*. These techniques suggest that three dimensionality may introduce a form of disorder into the spectra and wavemodes of fluid models.

We began our investigation by implementing a numerical approach to solving the linearised incompressible resistive MHD equations in three dimensional toroidal geometry. Benchmarking of the code highlighted the need to understand our incompressible model more clearly, leading to the investigations in section 6. There we consider the semi-analytical and numerical spectra of a range of fluid models applied to cylindrical plasmas in order to explore how well the physical problem is represented.

As a consequence of these results, and further numerical considerations related to spectral pollution, we decided to reformulate SPECTOR3D as a compressible resistive stability code; the resulting formulation offers better representation of the physics at the expense of reduced spatial resolution. The formulation is described in section 7, along with some test cases which demonstrate the proper functioning of the code. The application of our code to physical problems is of considerable interest, and we start by considering cases where the toroidicity does not qualitatively change the wavemodes of interest, but may have some effect on marginal stability points or growth rates. The first plasma configuration considered is a theoretical equilibrium of the LHD stellarator, where we demonstrate the effects of resistivity and toroidal coupling on MHD modes, as well as reproducing the published ideal MHD results. An application to tearing modes is presented next, for the Heliotron E stellarator, where previous studies have used one dimensional analytical arguments to determine stability. As the next step, we consider wavemodes which are not primarily composed of one set of poloidal and toroidal wavenumbers, but are strongly spatially localised. These modes often fall within the ballooning approximation, and require considerable Fourier space resolution to resolve at all. For this reason they are also a much more stringent test of the practical limitations of the code than the previous test cases. In subsection 7.17 we consider a sequence of tokamak-like equilibria with increasing ripple terms, in order to examine any toroidal localisation due to toroidal coupling. The equilibria chosen may be unstable in the ideal MHD limit to either $m/n = 1/1$ kink modes or ballooning modes according to the choice of parameters, and in the resistive MHD case, we expect that interchange and tearing modes may also be unstable. In three dimensional ideal MHD, it is likely that the most unstable ballooning mode is non-normalisable, and only approached numerically in the infinite resolution limit. However, re-

sistive MHD desingularises the spectrum, and so for high enough resolution we should be able to resolve the most unstable mode accurately. The modes we find become fully toroidally localised as we increase the toroidal coupling.

Although numerical techniques for plasma modelling have generated many useful results and can in principle fully describe the stability or dynamics of a plasma, analytical and semianalytical study are vital complementary techniques; they typically offer more physical insight, and they are often valid in limits where numerical approaches suffer from resolution constraints. In the ballooning approach, the long wavelength of instabilities along the magnetic field lines compared to the wavelength across the field is exploited as an ordering parameter; this has been very successful in determining the local stability of both stellarators and tokamaks. The stability analysis can be extended to global modes by considering quantisation; this is straightforward in tokamaks because the toroidal symmetry leads to a conservation of the toroidal wavenumber, and ensures a complete set of quantum numbers. In stellarators, however, the toroidal wavenumber is no longer a good quantum number. One important consequence is that in the ideal MHD ballooning limit, semiclassical ray tracing predicts an unbounded growth of wavenumber, and normalisable solutions cannot be constructed. The model we choose to address in section 8, which includes stabilisation due to finite Larmor radius effects, does not suffer from this problem, because the stabilisation is proportional to wavenumber. This conservative system admits a variational form, even though wave frequencies can become fully complex, and we show how Lagrangian methods lead to a standard semiclassical formalism. We demonstrate that even in cases with strong asymmetry it is possible to apply quantisation by considering the closed semiclassical orbits in ballooning space. Surprisingly, it is possible to justify a quantisation which is based on near-integrability in cases where chaos appears at first glance to be dominant. For some cases, however, where chaos is particularly important, it is necessary to use statistical arguments to provide an estimate for the quantities of interest.

4 MHD physics in stellarators

4.1 The ideal MHD equations

The ideal MHD model is one of the simplest models of plasma behaviour, and can be derived from the low order moments of the Vlasov equation:

$$\frac{\partial \rho}{\partial t} + \nabla \cdot (\rho \mathbf{v}) = 0 \quad (1)$$

$$\rho \frac{d\mathbf{v}}{dt} = -\nabla \cdot P + \mathbf{J} \times \mathbf{B} \quad (2)$$

$$\frac{dP}{dt} + \gamma P \nabla \cdot \mathbf{v} = 0 \quad (3)$$

$$\mathbf{E} + \mathbf{v} \times \mathbf{B} = 0 \quad (4)$$

$$\frac{\partial \mathbf{B}}{\partial t} = -\nabla \times \mathbf{E} \quad (5)$$

$$\mu_0 \mathbf{J} = \nabla \times \mathbf{B} \quad (6)$$

$$\nabla \cdot \mathbf{B} = 0 \quad (7)$$

We have \mathbf{B} , \mathbf{J} , \mathbf{E} , and \mathbf{v} representing the magnetic field, current density, electric field and fluid velocity, respectively. Also, P represents the (isotropic) pressure, γ the ratio of specific heats, and ρ is the mass density of the plasma. Note the use of the convective derivatives which are defined as $d/dt = \partial/\partial t + \mathbf{v} \cdot \nabla$.

4.2 Steady state solutions

We first consider the case of a static equilibria, with $\mathbf{v} = 0$, and $d/dt = 0$. We also have $E = 0$ and therefore

$$\nabla P = \mathbf{J} \times \mathbf{B}, \quad (8)$$

$$\mu_0 \mathbf{J} = \nabla \times \mathbf{B} \quad (9)$$

and

$$\nabla \cdot \mathbf{B} = 0 \quad (10)$$

In a fully three dimensional case, it is difficult to prove that nontrivial static solutions to these equilibrium equations exist. It has been shown [5] that there are 3D solutions with nested flux surfaces which can sustain a pressure difference between the plasma core and the edge, although the proof is not constructive, and the size of the domain of existence cannot be explicitly determined. From the theoretical perspective, it would be desirable to determine whether there are solutions to the MHD equations ‘nearby’ stellarator configurations of interest, but we do not know whether such a construction exists.

However, in practice, it is possible to find approximate solutions to these equations. This can be achieved using codes such as VMEC [6] and PIES [7], or analytical approaches like the stellarator expansion. The error in the resulting approximate equilibria can often be stated in terms of the residual in the force balance. We might hope that a small residual force indicated that we were close to a true solution, and the convergence of this procedure with increasing grid resolution could be taken to indicate the existence of a true equilibrium solution. Regardless of whether such convergence takes place, we find that these equilibria can be very accurate at moderate to large scales, where numerical resolution is not an issue. At sufficiently small scales the plasma is not accurately modelled by ideal MHD, and it is reasonable to tolerate small departures from equilibrium.

In spite of these issues, plasma can be efficiently confined in practise by a non-axisymmetric field, and there is strong evidence that the stationary plasma states of stellarators are consistent with MHD equilibrium. A numerically computed equilibrium can be compared directly with such experiments by measuring the shape of the plasma column, the profiles of surface functions or changes in the magnetic field; indirect comparisons can also be made using derived quantities like the stability limits and structure of gap modes. One direct study

compared the experimental measurements of the Shafranov shift to the predictions of MHD theory for heliotrons [8]: they were found to agree closely.

For the practical problem of finding analytic or numerical MHD equilibria, it is necessary to supply enough constraints on the equilibrium to fully specify the problem. Because MHD does not provide a full model of plasma behaviour, radial profiles which could in principle be calculated from knowledge of the experimental parameters need to be specified as constraints in an MHD equilibrium calculation. For equilibrium codes like VMEC, two independent radial profiles must be specified. Most MHD analysis of stellarators assumes that there is no net toroidal current present on any flux surface, and this zero toroidal current profile and a pressure profile are the two radial profiles most commonly used in stellarator analysis. The vacuum magnetic field structure also needs to be specified; for fixed boundary cases, the shape of an outer flux surface specifies the vacuum magnetic field structure uniquely.

For most present-day devices, the assumption that there is no net toroidal current is sufficiently accurate for studies of MHD behaviour: however, for many next generation devices we must consider the toroidal plasma current from the outset. It is possible for the toroidal current to contribute a significant proportion of the rotational transform in a reactor relevant stellarator, where bootstrap current or the secondary effects of heating can drive large currents. This is true in particular of configurations like NCSX, which is expected to have a large proportion of its rotational transform generated by bootstrap current when operated in the low collisionality regime.

Stellarator MHD equilibrium codes can roughly be divided into two groups, according to whether they assume the presence of a full nested set of flux surfaces:

One group of codes, of which VMEC [6] is the most well known example, represent the stellarator geometry using a coordinate system defined on a set of nested tori, corresponding to magnetic flux surfaces. The equilibrium problem is then solved by minimising the total energy of the configuration. This is implemented by varying the Fourier components of the set of unconstrained geometrical quantities and finding the minimising perturbation. Although the resulting equilibria contain no islands in the VMEC description, the actual reconstructed magnetic field may show the presence of islands, with singular currents arising at magnetic surfaces often heralding this feature.

In the other group of codes, which solve the unrestricted problem, are codes like PIES [7]. These codes resolve fully 3D equilibria, and can predict the existence of broken flux surfaces, where magnetic islands and stochastic regions can form. At each PIES iteration a plasma current consistent with some initial pressure profile and magnetic field structure is found (using force balance and

quasi-neutrality conditions). A new magnetic field can then be derived through Ampere's law. The old and the new magnetic field are then blended together, and the iteration repeats. The procedure usually converges, although it may do so rather slowly in some cases, especially when compared to codes like VMEC.

4.3 General stability theory

Ideal MHD stability considerations are important to the operation of magnetic confinement devices. Many ideal instabilities can lead to a complete loss of plasma confinement, or serve as a hard limit on plasma pressure, and the theoretical study of a magnetic confinement geometry usually begins with a test for stability against such modes.

Resistive MHD also plays an important role in assessing the stability of current-carrying devices, where tearing modes may disrupt the plasma on longer timescales, or lead to equilibria with rather different magnetic topology. It is not entirely clear whether more localised resistive modes limit the pressures in general confinement devices, but stabilising these modes (for example, by increasing the magnetic well) often appears to improve plasma confinement.

The analysis of MHD stability begins with the formulation of the linearised ideal MHD equations. These can be expressed compactly through the equation for the perturbed momentum,

$$\rho \frac{\partial^2 \boldsymbol{\xi}}{\partial t^2} = \mathbf{F}(\boldsymbol{\xi}), \quad (11)$$

where $\boldsymbol{\xi}$ is the displacement from equilibrium, and \mathbf{F} is the self-adjoint linear ideal MHD force operator. It is then possible to determine stability directly by time integrating an arbitrary small displacement of the plasma, or by considering the related eigenvalue problem with $\partial/\partial t \rightarrow i\omega$. However, because of the self-adjointness of \mathbf{F} , it is possible to express the stability of the system in terms of the sign of an energy functional; this is known as the energy principle. We consider the 'intuitive' form of this energy principle as described by [9] [10]:

$$\begin{aligned} \delta W_F = \frac{1}{2} \int_P d\mathbf{r} [& |\mathbf{Q}_\perp|^2 + B^2 |\nabla \cdot \boldsymbol{\xi}_\perp + 2\boldsymbol{\xi}_\perp \cdot \boldsymbol{\kappa}|^2 + \gamma p |\nabla \cdot \boldsymbol{\xi}|^2 \\ & - 2(\boldsymbol{\xi}_\perp \cdot \nabla P)(\boldsymbol{\kappa} \cdot \boldsymbol{\xi}_\perp^*) - J_\parallel (\boldsymbol{\xi}_\perp^* \times \mathbf{b}) \cdot \mathbf{Q}_\perp] \quad (12) \end{aligned}$$

where $\mathbf{b} = \mathbf{B}/B$, $\boldsymbol{\kappa} = \mathbf{b} \cdot \nabla \mathbf{b}$ is magnetic curvature vector, and $\mathbf{Q} = \nabla \times (\boldsymbol{\xi} \times \mathbf{B})$ represents the perturbed magnetic field. We have stability if for all $\boldsymbol{\xi}$ satisfying boundary conditions, $\delta W_F \geq 0$. This formulation is generally more amenable to analysis and computation than the initial value approach.

The integral in equation (12) can be split into those parts which are always positive, and thus stabilising, and others which may be able to drive δW negative. The last two terms describe the free energy available from the pressure gradients and parallel currents respectively. The most unstable mode can be found by minimising equation (12) with respect to variations in the test function ξ systematically. The integral can be minimised with respect to the parallel displacement by requiring that $\nabla \cdot \xi = 0$, implying that the compressibility of the plasma does not affect the sign of ideal MHD stability.

4.4 Local stability

Many of the dangerous modes of a toroidal plasma have very short wavelength perpendicular to the magnetic field lines, and they are therefore amenable to analysis along the field line using the *ballooning approximation* which will be considered in detail in section 8.3. This can be used to determine the stability of toroidal plasma model in the short wavelength limit. One important result of such an analysis is the Mercier criterion [10], which is a necessary criterion for stability which be expressed in terms of flux surface averages (denoted by angle brackets). One expression [11] for this criterion is

$$\frac{1}{4}S^2 + S \langle \mathbf{J} \cdot \mathbf{B} / |\nabla V|^2 \rangle - \Omega \langle B^2 / |\nabla V|^2 \rangle - \langle J^2 / |\nabla V|^2 \rangle \langle B^2 / |\nabla V|^2 \rangle - \langle \mathbf{J} \cdot \mathbf{B} / |\nabla V|^2 \rangle^2 > 0 \quad (13)$$

where S is a measure of the shear of the magnetic field, and Ω_0 is a measure of the magnetic well and V is the enclosed volume of a flux surface. The final term represents the destabilising effects of pressure through the perpendicular current. A similar resistive criterion D_I can be derived [12] which gives a considerably more conservative stability boundary, because shear does not stabilise resistive modes.

4.5 The case for global stability analysis

A global analysis, as opposed to a local analysis, of plasma stability, resolves the structure of instabilities throughout the volume of a plasma device. Such an analysis is necessary to comprehensively determine the stability of a toroidal device in addition to the local stability analysis, because the first modes to become unstable may have finite wavelengths. For tokamaks, for example, the internal kink modes, which deform the axis of the tokamak into a helical shape, and set in when the safety factor on axis goes below unity, are an important limitation on the achievable plasma parameters; local stability criteria alone are

not sufficient to address this concern. However, for stellarators with no toroidal current the local ideal MHD analysis gives a necessary criterion for stability, and the most dangerous internal instabilities occur at high n , where the ballooning formalism is valid, so it is not clear that global stability analysis is necessary at all.

However, what is observed experimentally when a plasma becomes MHD unstable depends crucially on whether the instabilities are localised in some very small region of the plasma, or are global and affect a large proportion of the plasma volume. The conventional wisdom is that global instabilities can lead to a complete and rapid loss of confinement, whereas local instabilities provide a soft limit to the maximum gradients which can be sustained. It is not straightforward to verify this, because although the global ideal MHD instabilities found in experiments can be reconciled with the linearised theory, the effects of localised instabilities are harder to measure experimentally. Interestingly, experiments sometimes perform significantly better than would be expected from linear MHD theory [13]. It seems that this is at least partly because of the physics missing from these simple models; in particular, we expect some of the neglected effects to be significantly stabilising for modes with small wavelengths perpendicular to the magnetic field [14] [15].

Therefore, if we wish to go beyond the simple classification of a plasma configuration as stable or unstable, and determine the likely effects of an instability, it is necessary to determine the spatial structure and growth rates of instabilities which arise. The important instabilities are of moderate wavenumber, rather than those at very small wavelength, where ideal MHD breaks down. For such modes, the spatial variation of plasma parameters becomes important.

One path to a global analysis is the semiclassical formalism. This can be used to determine the moderate wavelength ballooning spectrum for axisymmetric devices where quantised wavemodes can easily be constructed. For non-axisymmetric devices, the situation is less clear, because the eigensolutions of ideal MHD are generally not smooth, and quantisation is difficult to justify. For these cases it seems necessary to desingularise the ideal MHD model, as in [14].

Global stability can also be examined via numerics. A wavelength cutoff is inevitably introduced in the discretisation of ideal MHD as a consequence of finite gridspacing or Fourier resolution: this is generally not exactly equivalent to a physical cutoff, but it does desingularise the problem [16].

4.6 Resistive instabilities

Resistivity provides an interesting step away from ideal MHD because it relaxes the distinguishing characteristic of ideal MHD: the fluid is no longer

frozen into the field. It also changes the fundamental nature of the spectrum of linear perturbations, which becomes discrete, rather than continuous.

The extent to which resistive effects are important in a toroidal plasma can be quantified in terms of the resistive timescale τ_r , which measures the timescale on which plasma currents diffuse across from the center of the plasma to the edge: for magnetic confinement devices in the field of fusion research this timescale is not usually less than a millisecond, and typically much longer. The Alfvén timescale τ_A , on which the relevant ideal MHD behaviour takes place, is generally around a microsecond. Consequently we have $S \gtrsim 10^3$ and for hot plasmas S may be around 10^7 . Most MHD equilibria will dissipate on the resistive timescale, so when justifying a resistive stability analysis, we must remember that the linearisation is made around a quasi-equilibrium, rather than a true steady state. For this reason it is only meaningful to consider linear wavemodes in the system whose growth timescales are considerably smaller than the overall dissipation time, and the instabilities which satisfy this condition are strongly localised. The corresponding growth timescales τ can be somewhere in between τ_A and τ_R , so that as we take $S \rightarrow \infty$, the growth rate of the most unstable mode decreases, but the ratio $\tau/\tau_R \rightarrow \infty$.

The two most relevant resistive instabilities for the purpose of this study are the resistive interchange instability and the resistive tearing mode. Both of these modes have stricter local stability criteria than ideal modes, and can be considered analytically by using boundary layer techniques around the rational magnetic surface they resonate with [12]. However, in order to determine growth rates for finite S in realistic plasma configurations, numerical techniques are necessary.

5 Linear waves in plasma fluids.

5.1 Behaviour of non-normal systems: transients.

Although the normal mode picture provides an elegant and simple breakdown of many linear phenomena, its application to the ideal MHD model is not entirely straightforward. For modes of the Alfvén continua, normalised eigenmodes can no longer be constructed, and it is no longer possible to physically excite a single mode of the spectrum. Also, the ideal MHD model is singular, and the continua are destroyed by small physical perturbations. In resistive MHD, for example, there are no eigenmodes nearby most of the points in the ideal continuum, even when resistivity becomes vanishingly small.

Clearly a physical plasma is subject to dissipation, but experiments and time evolution studies show that the plasma has oscillatory behaviour at frequencies in the Alfvén continua. For the interpretation of the seeming discrepancy, we turn to pseudo-spectral methods, which help explain how to interpret the spectra. The key is to realise that the non-Hermitian spectrum of resistive MHD is strongly non-normal.

As a simple example of a non-Hermitian system, consider the simple set of linear equations:

$$\frac{d}{dt}x = \lambda_1 x + \sigma y \quad (14)$$

$$\frac{d}{dt}y = \lambda_2 y. \quad (15)$$

For $\lambda_1 = \lambda_2 = \lambda$, the solutions are given by $y = C \exp(\lambda t)$, $x = \sigma C t \exp(\lambda t) + D \exp(\lambda t)$. In this case, the non-Hermitian linear operator associated with the right hand side of the equation pair has a double eigenvalue, λ . As we expect, given some bounded initial conditions, the solutions are bounded in the case $\lambda < 0$, and the system is stable. However, for λ close to zero, the solution for x can potentially grow very large before exponential damping dominates. In fact, even where $\lambda_1 \neq \lambda_2$ there can be significant transient growth of the solution before exponential decay occurs.

This situation is generic for non-Hermitian linear systems which have small damping terms, like linearised resistive MHD. In the case of fluid flow in a pipe, transient effects are believed to explain sub-critical turbulence, where the onset of turbulence occurs significantly below the linear stability threshold [17]. The mechanism is a transient amplification of very small fluctuations by this non-normal effect, which are then non-linearly amplified before the overall small damping can set in.

To analyse such transient growth, the concept of the pseudospectrum [18]

has been useful. Several equivalent definitions exist, but we restrict ourselves to the following:

The ϵ -pseudospectrum of the linear operator A acting on the space X is the set of all $\lambda \in C$ such that

$$|Ax - \lambda x| < \epsilon \quad (16)$$

for some $x \in X$.

The definition suggests the idea of an ‘approximate eigenpair’ (λ, x) . It is possible to find a bound on the transient response of the system (Theorem 5 in [18]) through these pseudospectral quantities. Small values of ϵ at a frequency λ which is a reasonable distance from an exact eigenvalue λ_0 , so that $|\lambda - \lambda_0|/\epsilon \gg 1$ indicate that the system behaves for a while as if the approximate eigenvector, x , was a real eigenvector: for example, by behaving as though there were an instability for some time even in a stable case.

An investigation of the pseudospectrum of resistive MHD is related in [19]. In their cylindrical resistive MHD spectrum, they find that the eigenvalues and eigenvectors are extremely sensitive to a perturbation of the model. In the small resistivity limit, the entire stable annulus with $|\omega|$ in the Alfvén band is part of the ϵ -pseudospectrum for arbitrarily small ϵ , indicating that the individual eigenvalues are no longer meaningful. The transient response is therefore dominated in the small resistivity limit by this pseudospectrum, and the resistive eigenvectors are only relevant on long timescales, of $O(S^{1/2})$ compared to the Alfvén timescale.

In particular, this helps illuminate the *resistive Alfvén* paradox: it explains why resistive MHD and ideal MHD predict similar short term time evolution for smooth wavemodes, even though the spectra are entirely different.

The long timescale behaviour of the resistive MHD model is actually entirely different from the ideal model, and the eigenvalues reflect this. For short timescales, the behaviour of the resistive MHD system is approximately the same as for the ideal MHD system, given a smooth initial perturbation from equilibrium. The problem is that this is not at all evident from the spectra, which have few similar eigenvalues, so that we might expect completely different behaviour on all timescales. However, it is a mistake to try to use the time evolution of individual eigenmodes to characterise the time evolution of the entire system: most perturbations excite a large number of eigenmodes. In a strongly non-normal system, if we expand the initial perturbation in terms of the normalised eigenvalues, the coefficients can be much larger than the norm of the perturbation. In essence, the perturbation can then be viewed as a number

of very large wavemodes which happen to mostly destructively interfere at $t = 0$. The short time evolution is then determined by the collective interference of the wavemodes, which is dependent on the spatial structure of the eigenmodes, and cannot be predicted from the spectrum of eigenfrequencies alone. As long as we keep in mind that the raw eigenvalue spectrum does not in itself yield information about the transient behaviour, there is no contradiction in there being two entirely different spectra (from related models) which predict the same transient behaviour.

The question of linear stability can still be addressed using the eigenvalue spectrum: however, examination of the short-timescale response requires other techniques, such as a consideration of the initial value problem. It may then be necessary to consider non-linear effects if a strong transient amplification of the mode occurs.

The resistive MHD spectrum in a cylinder is found to be very non-normal in a conventional norm [19], but almost normal with respect to the energy norm (as we would expect for a slightly dissipative system). The transient effects may still be important path to nonlinearity, however, as it is quite possible for the mode's energy to become more spatially localised, and thereby more concentrated, or for the mode to form strong spatial gradients, by dephasing.

5.2 MHD, Quantum Mechanics, and behaviour in the short wavelength limit

Quantum mechanical waves have been so extensively and rigorously studied in physics that whenever any other wave system is under examination, parallels will inevitably be drawn to quantum mechanics. For the spectrum of several low-dimensional ideal MHD models there is a particularly strong relationship [20] with quantum mechanics because the relevant equations can be expressed in the Schrödinger form,

$$\frac{d^2\Phi}{dz^2} + [E - U(z)]\Phi = 0. \quad (17)$$

The spectrum of the Schrödinger equation is understood in great detail, and a comprehensive set of analytical tools exist to find it.

Even when there isn't an exact mapping between quantum mechanics and fluid theory, tools of wave analysis which were developed for quantum systems can often be put to service elsewhere. Semiclassical techniques, in particular, are useful in plasma systems, where the wavelengths of interest are often much smaller than the system scale lengths. Such analysis is built around the eikonal ansatz: it is assumed that the waves in the system can be represented by a

quickly oscillating wave component modulated by a slowly varying amplitude and wavenumber. It is then possible to solve the wave equations along *rays*, or *characteristics*, which are the paths in phase space which a wavepacket propagating in the system would follow. The set of ordinary differential equations which govern these paths, the *ray equations*, have a Hamiltonian form, and, like other Hamiltonian systems, may exhibit regular or chaotic behaviour. Semiclassical techniques can be used most effectively in systems where the ray dynamics are integrable or near-integrable systems: for such systems it is possible to find accurate eigenvalues and eigenvectors in the semiclassical limit. In chaotic systems, semiclassical methods can yield useful information on the time evolution of the system, and average quantities of spectra. In particular, the Weyl Formula can be used to estimate the density of eigenstates in a particular part of the spectrum. The exact positions of eigenvalues can be determined to high precision for some special chaotic models like the Hadamard–Gutzwiller model [21], via the trace formulae, but it is difficult to do this for real physical systems where an exponentially large number of orbits are required to achieve high precision.

A related perspective is random matrix theory which suggests that there is a statistical equivalence between the spectrum of chaotic physical systems and the spectrum of matrices with independent random elements. This equivalence implies that the fine details of the chaotic spectrum are essentially random and probably do not need to be accurately determined. Instead, we can concentrate on statistical characterisation, which is related only to the symmetries of our physical system. Random matrix theory is only rigorously justifiable in systems with *hard chaos*, where all the periodic semiclassical orbits are hyperbolically unstable, but in practise even gives a good description of the statistics of systems in which a small proportion of orbits are stable.

The possibility of chaos is a central feature differentiating stellarators from axisymmetric equilibria. In particular, chaos and chaotic effects are vital in the understanding of stellarator particle confinement: this point was recently underscored by the program of quasi-symmetrisation, where successful searches were made for stellarators with near-integrable, instead of chaotic, particle trajectories. However, it is collective behaviour, rather than individual particle dynamics, which is the dominant theme of plasma physics, and chaos may also have a role to play in wave phenomena; we will consider the wave chaos in stellarators which is predicted by linearised fluid models. To this end, we review the background to the techniques of semiclassical chaos and random matrix theory, which may not have come to the attention of many in the stellarator community, and are central to the study of wave chaos.

5.3 The semiclassical formalism, the Weyl formula, and trace formulae

The WKB solution to a wave problem is based on the eikonal ansatz, in which solutions take the form [22]

$$\Phi(q, t) = \sum_j e^{iR_j(q, t)/\hbar} \quad (18)$$

where the sum allows for solutions to overlap (e.g. to form a standing wave). The small parameter $\hbar \rightarrow 0$ in the short wavelength limit. In optics, this is known as the ray approximation, and the phase fronts can be considered to be transported by particles which travel at the group velocity, undergoing refraction and reflection. In quantum mechanics, the wavefronts are transported along the path of the classical particles. This is called a semi-classical solution because the ‘quantum’ parameter only enters the solution in the scale length of the fast phase variation, and the rest of the solution can be determined entirely from classical particle propagation. The formalism excludes effects like diffraction and tunnelling, where the scale length determines whether the wave is able to propagate into classically forbidden regions.

We outline the derivation of this formalism for a general wave problem

$$i\hbar\mathbf{K}\frac{\partial}{\partial t}\Phi = \mathbf{H}\Phi \quad (19)$$

where \mathbf{K} and \mathbf{H} are operators containing combinations of spatial derivatives up to finite order and smooth functions. We require that each spatial derivative is accompanied by a factor of \hbar in order to appear at leading order.

It can be shown by direct substitution into the wave equation of interest that our ansatz is an approximate solution up to $O(\hbar)$ if the phase $R_j(q, t)$ varies on the system scale. The resulting equations can be expressed to leading order as

$$\left(i\hbar\hat{\mathbf{K}}(\nabla\mathbf{R})\frac{dR}{dt} + \hat{\mathbf{H}}(\nabla\mathbf{R}) \right) \Phi = 0 \quad (20)$$

Here $\hat{\mathbf{K}}(\nabla\mathbf{R}), \hat{\mathbf{H}}(\nabla\mathbf{R})$ are defined by replacing spatial derivatives in \mathbf{K} and \mathbf{H} by the gradient of the phase.

An estimate for the average density of states in a spectrum is given by the Weyl formula. For wave modes propagating in a box the Weyl formula reduces to the observation that the number of states below some frequency cutoff is approximately proportional to the volume of the box. For a more general problem, we find that the total number of states can be estimated from the phase space volume in which the waves can propagate. Specifically, the

number of modes N in the frequency interval $[0, \omega_{\text{cutoff}}]$ is given by

$$N = \frac{1}{(2\pi)^n} \int_V d\mathbf{x}d\mathbf{k} \quad (21)$$

where n is the dimensionality of the space, and we integrate over the region of phase space V where the local dispersion relation $\Omega(\mathbf{x}, \mathbf{k}) \in [0, \omega_{\text{cutoff}}]$.

5.4 Random Matrix Theory

Random matrix theory posits that wave systems that are strongly chaotic in the semiclassical sense have a spectrum which is statistically equivalent to the spectrum of particular classes of random matrices. This has been confirmed by statistical investigation of numerical spectra, as well as by experimental investigations of the spectra of various systems, like the acoustic resonances in a quartz block [23], and nuclear energy levels [24]. Random matrix theory is usually used to explore the fine structure of the spectrum, at the individual wavemode scale, and is therefore complementary to a trace formula approach, which usually converges poorly in this limit. One important feature of the physical spectrum of chaotic systems which is modelled correctly by random matrix theory is the phenomenon of *level repulsion*. In chaotic systems energy levels are seldom close together, whereas in integrable systems degeneracies and near degeneracies are quite common; the strong mixing of quantum numbers in chaotic systems usually breaks such degeneracies. The strength of this level repulsion can be characterised by considering the probability density function for the spacing between neighbouring eigenvalues, which can be derived from random matrix theory for specific classes of matrix. There are three such classes of random matrices known to be relevant to physical spectra, and they can be classified according to their structure, and the invariance properties of the systems they model:

- **The Gaussian Orthogonal Ensemble.** These matrices model energy-conserving systems with time-reversal invariance.
- **The Gaussian Unitary Ensemble** These matrices model energy-conserving systems without time-reversal invariance.
- **The Gaussian Symplectic Ensemble** These matrices model dissipative systems.

Because stellarator symmetry can be shown to imply a time-reversal invariance for MHD [25] it is expected that MHD systems which exhibit chaotic features will have spectral features related to the Gaussian Orthogonal Ensemble.

This has been confirmed in numerical MHD spectra [26] by examining features of the spectrum, and in particular, by demonstrating that level repulsion occurs, corresponding to that expected for the Gaussian Orthogonal Ensemble. The presence of quantum chaos in numerical spectra confirms the semiclassical predictions of chaos in such spectra [16]. More generally, it supports the use of global semiclassical analysis in these three dimensional systems, where the singularity of ideal MHD makes it difficult to assign a meaningful interpretation to semiclassical results. Conversely, random matrix theory helps to shed light on numerical results, building confidence in the numerical treatment. A more physical consequence of this kind of chaos is the prediction of wavemodes which have complicated spatial structure, and do not necessarily conform to the usual ‘fingered’ structure seen for ballooning instabilities.

It is certainly interesting from a mathematical point of view that these statistical details of the MHD spectrum are predicted by a theory developed for quantum mechanics, and we hope that the analogy can be extended further to allow access to the rich vein of understanding known as *quantum chaology*. One phenomenon which is particularly interesting is the possibility of chaos playing a role in the mixing and decorrelate of externally driven long wavelength modes. We suggest that there is a link here to the study of decoherence in chaotic quantum mechanical systems.

Instead of pursuing further details of spectral statistics in this thesis, we will concentrate on the use of the semiclassical techniques to derive quantities of interest, and in particular, marginal stability criteria.

6 A Comparison of Incompressible Limits for Resistive Plasmas.¹

6.1 Summary

The constraint of incompressibility is often used to simplify the magnetohydrodynamic (MHD) description of linearized plasma dynamics because it does not affect the ideal MHD marginal stability point. In this paper two methods for introducing incompressibility are compared in a cylindrical plasma model: In the first method, the limit $\gamma \rightarrow \infty$ is taken, where γ is the ratio of specific heats; in the second, an anisotropic mass tensor ρ is used, with the component parallel to the magnetic field taken to vanish, $\rho_{\parallel} \rightarrow 0$. Use of resistive MHD reveals the nature of these two limits because the Alfvén and slow magnetosonic continua of ideal MHD are converted to point spectra and moved into the complex plane. Both limits profoundly change the slow-magnetosonic spectrum, but only the second limit faithfully reproduces the resistive Alfvén spectrum and its wavemodes. In ideal MHD, the slow magnetosonic continuum degenerates to the Alfvén continuum in the first method, while it is moved to infinity by the second. The degeneracy in the first is broken by finite resistivity. For numerical and semi-analytical study of these models, we choose plasma equilibria which cast light on puzzling aspects of results found in earlier literature.

6.2 Introduction

We devote our attention to the ideal and resistive MHD models, which, despite their dramatic simplification of plasma behaviour, are crucial to the design and operation of controlled fusion devices and are at the core of many astrophysical plasma models. Simplified models such as these have utility if they can be used to make testable predictions or if they yield insight into the internal processes of a system. We test two variants of incompressible resistive MHD with these criteria in mind. The starting point for the analysis of most plasma models is an understanding of the wavemodes that arise: this provides information about the linear response and stability of the system and provides a basis for much nonlinear analysis. We focus on the linear behaviour of the plasma in this paper. For the resistive MHD model, which includes dissipation, the wavemodes are non-normal: a full picture of linear plasma behaviour requires an analysis of the transient behaviour of the system, as well as the eigenvalue analysis which predicts asymptotic behaviours over long time scales. These are closely

¹Much of the material in this section was published in [27]. R.L. Dewar and R.G. Storer, as second and third authors, contributed a small proportion of the text, and had many useful suggestions. In particular, R. L. Dewar, derived equation (25). Thanks also go to the referees.

related via pseudospectral methods [19]. In this paper we restrict attention to eigenvalue analysis.

For many plasmas of physical interest it is true that the resistive term is small: typically this is quantified by a large magnetic Reynolds number. It might have been expected that for small enough resistivity, the resistive MHD model could simply be treated as a perturbation of the ideal MHD model. However, the change induced is actually a singular perturbation, which introduces higher spatial derivatives. One of the interesting effects of this property is that eigenfrequencies in the ideal model are not necessarily approached by the eigenfrequencies of any resistive modes, even for vanishingly small resistivity.

Many papers have been published on the stable resistive MHD spectrum and several of the early papers ([28]- [32]) focused on cylindrical models. These papers have established certain generic features of the resistive spectrum. The resistive spectrum is discrete, unlike the ideal MHD spectrum which has continua: on some intervals, every frequency corresponds to a generalised wavemode. In the resistive spectrum, a large number of fully complex eigenfrequencies can be found, and in general these lie along loci, or curves, on the complex plane. Generally as the resistivity is decreased to zero these lines become densely populated with eigenvalues.

Resistive MHD is a simple closure of the full kinetic equations, and as a result the plasma dynamics parallel to the magnetic field lines are often quite poorly represented [33]. For Alfvénic modes, which do not strongly compress the plasma, these parallel dynamics are generally unimportant. However, for the slow and fast magnetoacoustic waves, the parallel dynamics and the effects of compressibility are important; these waves are not necessarily well modelled by resistive MHD.

It is possible to find the compressible resistive MHD spectrum numerically (as in [31]) and ignore the slow and fast magnetoacoustic waves that are present. On the other hand, there are approaches which promise to isolate the Alfvénic portion of the spectrum and simplify the analysis. We present two of these incompressible approximations, in which the predicted motions of the plasma satisfy $\nabla \cdot \mathbf{v} = 0$ (at least approximately). One approach is to artificially set the ratio of specific heats γ to infinity (as in [30] and [32]). In the other, an anisotropic mass tensor ρ is used, with the component parallel to the magnetic field taken to vanish, $\rho_{\parallel}/\rho_{\perp} \rightarrow 0$. With this density tensor, ideal eigenmodes are incompressible, but to ensure exact incompressibility for resistive eigenmodes γ must again be set to ∞ . We can view these models as the extreme cases of a generalised resistive MHD model with two parameters, γ and $\rho_{\parallel}/\rho_{\perp}$. The two extreme cases are not equivalent, and the resulting spectra are qualitatively different. We investigate these two methods, and compare them with the com-

pressible resistive MHD model. We specialise to equilibria with zero background flow. Note that $\gamma \rightarrow \infty$ may be physically appropriate for particular conductive fluids and plasmas with $\beta \gg 1$.

First, we examine the plane waves of the homogeneous incompressible MHD model. Then we evaluate spectra in a simple cylindrical equilibrium for varying values of γ , and with and without an artificial anisotropic density. This illustrates the transition between the compressible and incompressible cases. We then discuss the spectra of more general plasma configurations. A WKB analysis of a generic incompressible model is then undertaken in order to understand the features of these spectra and to verify the numerics. We begin by solving the dispersion relation. Then the singular features of this function are explored by reducing it to a simpler form. To complete the groundwork for semi-analytic calculations, the behaviour of the wave equation near these singular points is examined. Finally, we use our WKB analysis to find the spectrum of an example case.

6.3 Wavemodes in incompressible MHD limits

The first step in the analysis of these incompressible limits is a determination of the wavemodes in a simple homogeneous plasma. To this end we follow [33] and derive wave frequencies. We begin by considering a wave with wavevector at some angle to the magnetic field $\mathbf{B} = B_0 \hat{z}$, so $\mathbf{k} = k_{\parallel} \hat{z} + k_{\perp} \hat{x}$, travelling in a plasma with sound speed $V_s = (\gamma p_0 / \rho_0)^{1/2}$ and Alfvén speed $V_a = (B_0^2 / \mu_0 \rho_0)^{1/2}$. We recover the Alfvén spectrum:

$$\omega_A^2 = k_{\parallel}^2 V_a^2, \quad (22)$$

and also two other solutions to the plasma equations:

$$\omega_{\pm}^2 = \frac{1}{2} k^2 (V_a^2 + V_s^2 + \frac{\rho_{\parallel} - \rho_{\perp}}{\rho_{\parallel} k^2} k_{\parallel}^2 V_s^2) \left(1 \pm (1 - \alpha^2)^{\frac{1}{2}} \right), \quad (23)$$

where

$$\alpha^2 = \frac{4 \rho_{\perp} k_{\parallel}^2 V_a^2 V_s^2}{k^2 \rho_{\parallel} (V_a^2 + V_s^2 + \frac{\rho_{\parallel} - \rho_{\perp}}{\rho_{\parallel} k^2} k_{\parallel}^2 V_s^2)^2}. \quad (24)$$

In low- β compressible plasmas, ω_+ corresponds to the fast magnetoacoustic wave, and ω_- to the slow magnetoacoustic wave.

In the limit $\gamma \rightarrow \infty$ (with $\rho_{\parallel} / \rho_{\perp} = 1$) we find $\omega_+^2 \rightarrow \infty$ and $\omega_-^2 \rightarrow k_{\parallel}^2 V_a^2$, so that the slow-mode is now degenerate with the Alfvén mode. In more general plasma configurations, the slow and the Alfvén wavemodes still occur at

very similar frequencies, and therefore can be strongly mixed. We show this does occur, so that generic spectra determined are composed of an unphysical combination of these types of wavemodes. In the limit $\rho_{\parallel}/\rho_{\perp} \rightarrow 0$ we again have $\omega_{+} \rightarrow \infty$, but $\omega_{-}^2 \rightarrow k^2 V_a^2 + k_{\perp}^2 V_s^2$, which is slightly larger than the fast magnetoacoustic frequency. In this case we have effectively suppressed the slow magnetoacoustic waves because they are now stable and very weakly coupled to the Alfvén modes.

If we set $\rho_{\parallel}/\rho_{\perp} \rightarrow 0$, we can show from the linearised equations that for general resistive MHD wavemodes $\rho_{\parallel} \rightarrow 0$ implies:

$$\mathbf{B}_0 \cdot \nabla (\nabla \cdot \mathbf{v}) = - \frac{\nabla P_0 \cdot \nabla \times (\eta \mathbf{j})}{(\gamma P_0)}, \quad (25)$$

where B_0 and P_0 are the equilibrium field and pressure, η is the resistivity and \mathbf{j} and \mathbf{v} are the perturbed current and velocity. So for the ideal case ($\eta = 0$) we have that $\nabla \cdot \mathbf{v}$ is a constant on all irrational surfaces, and, by continuity, for finite toroidal or poloidal mode number, we must have $\nabla \cdot \mathbf{v} = 0$. In the resistive case, we have small η , but possibly large d/dr so that resistive modes are not strictly incompressible. However, if we also require $\gamma \rightarrow \infty$ then the resistive modes are strictly incompressible.

6.4 Numerical results of varying incompressibility

In order to show the effect of incompressibility on the resistive MHD spectrum, we solved the compressible, resistive MHD equations numerically. We implemented a code based on the description in [34].

We examine a cylindrical, zero-shear model case, as described in [32], with $\beta \approx 4\%$. The incompressibility is explored by varying γ in the range 1 – 1000. The incompressible limits correspond to $\gamma \rightarrow \infty$, but in this case $\gamma \simeq 1000$ is high enough to demonstrate the limit. We define the magnetic Reynolds number $S = \tau_R/\tau_A$ where τ_A and τ_R are the Alfvén and resistive timescales. For a cylinder of radius r_p we have $\tau_A = r_p(\mu_0 \rho)^{1/2}/B_z$, and $\tau_R = r_p^2 \mu_0/\eta_0$. The magnetic field perturbations are of the form $\mathbf{b} = \exp(im\theta - i\kappa z/r_p - i\omega t) \mathbf{b}(r)$, with $\kappa = nr_p/R$, where by analogy with the toroidal case R can be interpreted in the sense that $2\pi R$ is the length of the plasma column, and n is the ‘toroidal’ mode number. We have $\beta \approx 4\%$, which allows the slow-mode spectrum to be shown on the same scale as the Alfvén spectrum in the compressible case. The resulting spectra are shown in figure 1. For this case $m = 1$, $\kappa = 0.35$, $nq = 1.2$ and $S = 1 \times 10^4$. Note that figure 1(e) corresponds to the limit $\gamma \rightarrow \infty$ and figure 1(f) corresponds to the limit $\rho_{\parallel}/\rho_{\perp} \rightarrow 0$.

In these cases the ideal Alfvén continuum degenerates to a point, at $\omega_A =$

0.057, but the ideal slow continuum is finite in extent because of pressure and field strength variation across the plasma. The slow continuum extends to the origin because the pressure is taken to be zero at the plasma boundary. Note the fork structure seen for the slow modes near the origin of figure 1(a). This fork structure is lost as γ is increased [figures 1(b)–(e)]. Finally, as $\gamma \rightarrow \infty$, most of the mode frequencies are in the vicinity of a semicircle of radius ω_A on the complex plane. From the figure, we see that there are many more modes near ω_A in the $\gamma \rightarrow \infty$ model, than in the more physical compressible model. It has been shown in [32] that for this incompressible the wavemodes are eigenfunctions of the curl operator, and most of them do not correspond directly to physical compressible wavemodes. In figure 1(e), the two loci of eigenvalues correspond to wavemodes whose eigenvalues under the curl operator are of opposite sign: the waves can be classified according to their helicity, but not usually according to whether they represent shear Alfvén modes.

For the $\rho_{\parallel}/\rho_{\perp} \rightarrow 0$ model, we find a spectrum [figure 1(f)] very similar to the compressible spectrum in figure 1(a), but with the notable absence of the slow-mode fork. The position of individual Alfvénic eigenvalues is in fact well preserved in this model. The only noticeable deviation is the eigenmode near the real axis, at $Re(\omega) \simeq 0.035$, which has a frequency shift of magnitude $\simeq 0.004$ as a result of setting $\rho_{\parallel}/\rho_{\perp} \rightarrow 0$. Since this Alfvén eigenmode is fairly close in frequency to the slow modes, it is not surprising that it is the one most strongly modified by an assumption of incompressibility.

6.5 Generic spectra in resistive MHD

For general plasma configurations with shear, the resistive Alfvén spectrum is usually found to form a fork (e.g. figure 2 or those in [28] - [31]) The rather different shape of the spectral loci in figures 1(a)-(f) is a consequence of the equilibrium having an Alfvén spectrum which degenerates to a point.

The fork structure in the resistive MHD spectrum has been qualitatively explained in terms of WKB analysis by examining turning points within the plasma, see [29] and [31]. The fork has three lines joining at a point below the ideal MHD continuum. Two lines run between the intersection point and either end of the Alfvén continuum. The third line runs around approximately in a quarter circle to touch the imaginary axis. In a simple model with toroidal current density constant across the plasma, there is an analytical solution for the $\gamma \rightarrow \infty$ resistive MHD spectrum [32]. We show that a perturbed variant of this constant current model, in which a slight shear is given to the magnetic field, is still amenable to the manipulations performed in [32]. By introducing shear we produce a model which has a finite width Alfvén continuum, in which we

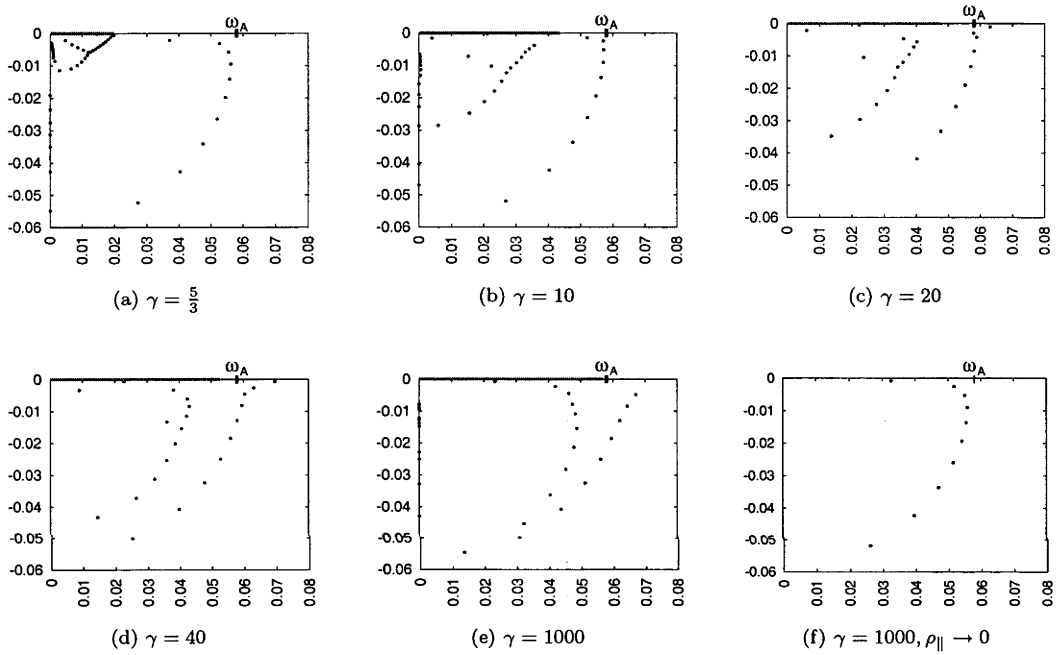


Figure 1: The compressible resistive spectrum of a constant current model ($\beta = 4\%$) for various values of γ . The frequencies ω are plotted in the complex plane with the real frequency along the horizontal axis and the complex frequency on the vertical axis. The ideal slow-mode continuum is represented by a grey line on the real axis.

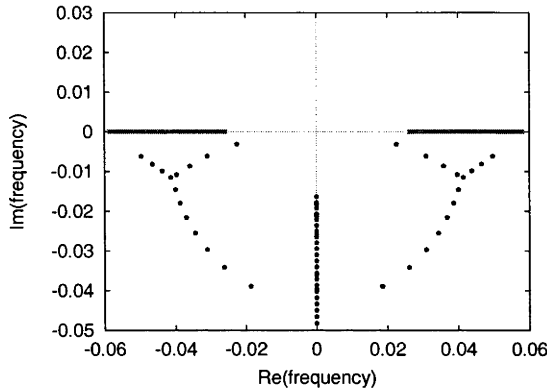


Figure 2: A typical eigenvalue spectrum for a compressible ($\gamma = \frac{5}{3}$) resistive MHD case showing the complex frequencies of damped and growing normal modes. In this low-pressure case, slow magnetosonic modes have eigenfrequencies very close to the origin and are not shown. The plasma model parameters are similar to the constant current case, but with a small shear: $m = 1$, $\kappa = 0.35$, $nq(r) = 1.2 \times (1 - 0.1r)$ and $S = 3 \times 10^3$. The ideal Alfvén continuum is represented by a grey line on the real axis.

might hope to recover the generic fork structure found in compressible results. We therefore solved this model using WKB analysis to explain the qualitatively different spectrum. In the remainder of this section we set $\rho_{\perp} = \rho_{\parallel} = \rho$.

6.6 WKB analysis of a small shear equilibrium in the limit $\gamma \rightarrow \infty$

The model case is derived from [32], which considers a cylindrical plasma with a constant axial field and no shear. This model has been studied earlier in [35],[36]. The equations used for this analysis are those of linearised, resistive, incompressible MHD, with $\gamma \rightarrow \infty$:

$$\rho\mu_0 \frac{\partial}{\partial t} (\nabla \times \mathbf{v}) = \nabla \times (\mathbf{B} \cdot \nabla \mathbf{b} + \mathbf{b} \cdot \nabla \mathbf{B}), \quad (26)$$

and magnetic field given by Ampère's law

$$\frac{\partial \mathbf{b}}{\partial t} = \nabla \times (\mathbf{v} \times \mathbf{B}) - \nabla \times \left(\frac{\eta}{\mu_0} \nabla \times \mathbf{b} \right). \quad (27)$$

The curl of the equation of motion is taken in order to suppress the perturbed pressure. Also, we specialise to an equilibrium state with no plasma velocity.

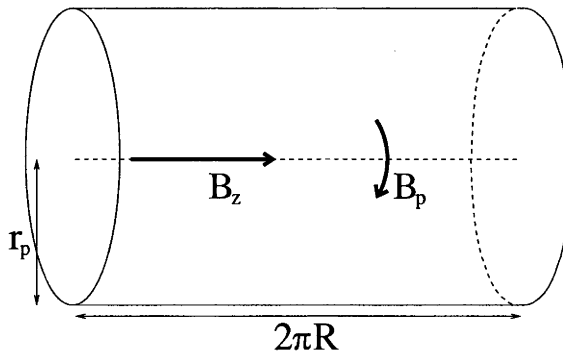


Figure 3: One period of the cylindrical model.

The idea is to introduce the shear as a small quantity, of the same order as the inverse wave number. The analysis is then the same as the shear-free case, up to two orders in the inverse wavenumber. The radial dependence is included in the dispersion relation in the radially varying quantities: $B_z(r)$, $B_p(r)$ and $q(r)$. We first take the large wavenumber limit by ordering $\nabla \simeq O(1/\epsilon)$. For significantly dissipative modes, maximal balance of Ampère's law (27) occurs for $\epsilon \simeq O(S^{-1/2})$. In a typical physical situation we might have $S > 1000$ and thus $\epsilon < 0.03$ is a good expansion parameter.

The magnetic field is expressed as $\mathbf{B} = \hat{z}B_z(r) + r\hat{\theta}B_p(r)$ with $d(\log[B_p(r)])/dr$ and $d(\log[B_z(r)])/dr$ both of $O(\epsilon)$, in order to satisfy the requirement of small shear. We again look at perturbations of the form $\mathbf{b} = \exp(im\theta - ikz/r_p - i\omega t)\mathbf{b}(r)$. For convenience we set \mathbf{b} as $O(1)$ and this then implies \mathbf{v} to be of $O(1)$ to complete the ordering. By using the relations $\nabla \cdot \mathbf{b} = \nabla \cdot \mathbf{v} = 0$, equations (26) and (27) can be reduced to:

$$\rho\mu_0\frac{\omega}{\tau_A}(\nabla \times \mathbf{v}) = \frac{B_p(r)}{r_p}[m - nq(r)]\nabla \times \mathbf{b} + \frac{2B_p(r)}{r_p^2}\kappa\mathbf{b} + O(\epsilon) \quad (28)$$

and

$$-\frac{i\omega}{\tau_A}\mathbf{b} = \frac{iB_p(r)}{r_p}[m - nq(r)]\mathbf{v} - \frac{\eta}{\mu_0}(\nabla \times \nabla \times \mathbf{b}) + O(\epsilon). \quad (29)$$

The safety factor $q(r)$ is given by $r_p B_z(r)/R B_p(r)$ and the non-dimensional resistivity $\eta = S^{-1}$.

In this form, the only differential operator is the curl operator. This motivates us to look for solutions which are eigenfunctions of this operator, suggesting the ansatz

$$r_p \nabla \times \mathbf{v} = \alpha \mathbf{v}, \quad r_p \nabla \times \mathbf{b} = \alpha \mathbf{b}, \quad (30)$$

which solves equations (28) and (29) provided

$$\alpha(r, \omega) = \frac{2[m - nq(r)]\kappa}{\frac{B_z(r)^2}{B_p(r)^2} i\omega [i\omega - S^{-1}\alpha(r, \omega)^2] + [m - nq(r)]^2}. \quad (31)$$

By taking the curl of equation (30) we get

$$\nabla \times \nabla \times \mathbf{v} = -\nabla^2 \mathbf{v} = \frac{\alpha^2}{r_p^2} \mathbf{v}, \quad (32)$$

since the velocity is divergence-free. This implies a relation for the z component of \mathbf{v}

$$\frac{1}{r} \frac{d}{dr} r \frac{d}{dr} v_z = - \left(\frac{\alpha^2}{r_p^2} + n^2 - \frac{m^2}{r^2} \right) v_z. \quad (33)$$

This is amenable to standard WKB analysis if α is large, and in this WKB limit equation (33) is equivalent to:

$$\frac{d^2}{dr^2} \mathbf{v}_z = -Q(r) \mathbf{v}_z, \quad (34)$$

with $Q(r) = \alpha^2/r_p^2$. This will break down near the origin ($r = 0$) where we will use a Bessel function matching. Equation (34) is solved approximately by:

$$\mathbf{v}_z \simeq a_{\text{out}} Q^{-\frac{1}{4}} e^{i\phi} + a_{\text{in}} Q^{-\frac{1}{4}} e^{-i\phi} \quad (35)$$

where the amplitudes a_{out} and a_{in} are slowly varying functions, and

$$\phi(r|c) = \int_c^r Q^{\frac{1}{2}}(r') dr' \quad (36)$$

Thus α/r_p is the radial wavenumber and equation (31) provides the dispersion relation.

6.7 Characterising the Stokes points

To find the WKB solutions, it is first necessary to examine the structure of the dispersion relation in the plasma region. In particular, singularities and zeros and the associated branch structure of the dispersion relation must be examined. Branch points of the dispersion relation are known as *Stokes points*. The dispersion relation (31) can be written as a cubic equation in α , with the coefficients as functions of $q(r) = r_p B_z(r)/RB_p(r)$, i.e.

$$\alpha^3 \frac{1}{S} \left(\frac{q(r)R}{r_p} \right)^2 + \alpha \left([m - nq(r)]^2 - \left(\frac{qR}{r_p} \right)^2 \omega^2 \right) = 2[m - nq(r)]\kappa. \quad (37)$$

We would like to discover the singularity structure of our dispersion relation. Solving equation (37) for α leads to very ungainly equations and proves not to be enlightening, so we look for a simpler relation which will be topologically equivalent. Let us consider the case where there is no magnetic surface resonant with the perturbation. In this case we have $[nq(r) - m] \neq 0$ within the plasma, and assuming also $q(r) \neq 0$ then we can divide through the equation by $2[m - nq(r)]\kappa$ and introduce a new variable $\bar{\alpha}$ so that

$$\bar{\alpha}^3 + x(r)\bar{\alpha} = 1, \quad (38)$$

with

$$\bar{\alpha} \equiv \alpha \frac{\{2[nq(r) - m]\kappa S\}^{\frac{1}{3}}}{(q(r)R/r_p)^{\frac{2}{3}}} \quad (39)$$

and

$$x(r) \equiv \frac{\{[nq(r) - m]^2 - [qR/r_p]^2 \omega^2\}}{\{2[nq(r) - m]\kappa S(qR/r_p)\}^{\frac{2}{3}}}. \quad (40)$$

The solution of equation (38) for $\bar{\alpha}$ is

$$\bar{\alpha} = -\xi \frac{2^{\frac{1}{3}} x}{(27 + \sqrt{729 + 108 x^3})^{\frac{1}{3}}} + \xi^* \frac{(27 + \sqrt{729 + 108 x^3})^{\frac{1}{3}}}{3 \cdot 2^{\frac{1}{3}}}, \quad (41)$$

where ξ is one of the cube roots of -1 :

$$\xi = -1, \quad \frac{1+i\sqrt{3}}{2}, \quad \frac{1-i\sqrt{3}}{2}. \quad (42)$$

We consider x as a new radial variable. The function $\bar{\alpha}$ is represented graphically by the Polyá plot in figure 4.

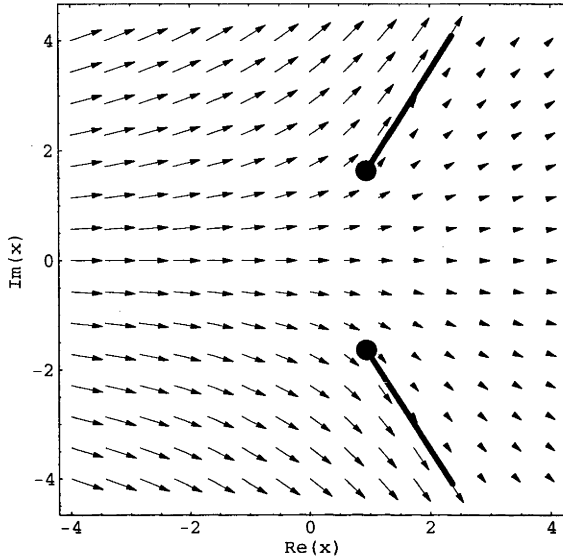


Figure 4: One branch of the multivalued function $\bar{\alpha}(x)$ ($\xi = -1$) shown on the complex plane as a Polyá plot. Branch cuts are indicated as thick lines. The vector $(\text{Re}[\bar{\alpha}], -\text{Im}[\bar{\alpha}])$ is displayed on a grid. The other two branches of $\bar{\alpha}(x)$ can be obtained by a rotation around the complex origin by $2\pi/3$ and $4\pi/3$ respectively.

By inspection of the form of equation (41) we have candidates for branch points at the three roots of $x^3 = -27/4$. However, only two of these candidate branch points appear on any single sheet of the function, as shown by figure 4. To demonstrate that there is a branch point absent from each sheet, we consider the $\xi = -1$ case, where we might expect a branch point at $x = -\sqrt[3]{27/4}$ from inspection of equation (41). At this point we have $\bar{\alpha} = 2^{2/3}$. We note that equation (38) can be rewritten as the inverse function of equation (41),

$$x(\bar{\alpha}) = \frac{1 - \bar{\alpha}^3}{\bar{\alpha}}. \quad (43)$$

It is easy to verify that there is a neighbourhood of $\bar{\alpha} = 2^{2/3}$, where x in an analytic function of $\bar{\alpha}$ and $dx/d\bar{\alpha}$ is nonzero. We can therefore construct an analytic inverse of this function, which will be equal to equation 41 in the

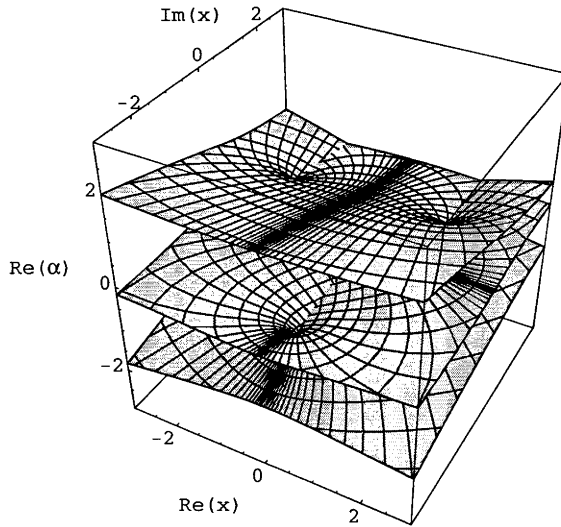


Figure 5: A surface plot of the multivalued function $\bar{\alpha}(x)$ demonstrating the interleaved Riemann sheets.

neighbourhood of $x = -\sqrt[3]{27/4}$, ruling out the possibility of a branch point existing there. Similarly, it follows that each of the other cases of equation (41) have only two branch points each. Around a particular branch points at some position x_0 , we do not have $\alpha \propto \sqrt{x - x_0}$, as is typical for many WKB analyses [37]. Instead, we have $\alpha \simeq C + D\sqrt{x - x_0}$.

6.8 Phase matching: a solution near the singularities

In order to proceed with WKB analysis, we need to determine the behaviour of solutions near the Stokes points, the branch points of the dispersion relation. In the neighbourhood of the branch point, we approximate the dispersion relation by:

$$Q(x) \simeq 1 + Ax^{\frac{1}{2}}. \quad (44)$$

This is unlike the more usual situation in WKB analysis where $Q(x) \simeq x$ around the Stokes points. The simplest treatment of the phase matching follows from considering $A \ll 1$ in which case the $A = 0$ case can be used as a zeroth order solution in a region around the Stokes point. Note that for $A = 0$, the dispersion relation is independent of x and there is no reflection of the wave. As we will

see, as $A \rightarrow 0$ the reflectivity goes to zero. The transmitted part of the wave will be decaying for finite A , so that we have partial absorption of the travelling wave.

Our wave equation is

$$\frac{d^2 y}{dx^2} = -(1 + Ax^{\frac{1}{2}})y, \quad (45)$$

with an $A = 0$ solution

$$y_0 = e^{\pm ix}, \quad (46)$$

which motivates the substitution

$$y = e^{-ix+u(x)}. \quad (47)$$

The other choice of sign leads to a second solution to the equation, which is growing for $x \rightarrow -\infty$. Substitution of equation (47) into equation (45) leads to

$$A\sqrt{x} - 2i\frac{du}{dx} + \left(\frac{du}{dx}\right)^2 + \frac{d^2 u}{dx^2} = 0. \quad (48)$$

We are looking for small departures from the $A = 0$ solutions and in this case we can choose $du/dx \ll 1$ so that to first order

$$A\sqrt{x} - 2i\frac{du}{dx} + \frac{d^2 u}{dx^2} = 0, \quad (49)$$

from which we can find $u'(x)$

$$u'(x) = e^{2ix} C - \frac{i}{8} A \left[4\sqrt{x} + e^{(2x-\pi/4)i} \sqrt{2\pi} \operatorname{erf}\left(e^{-3\pi i/4} \sqrt{2x}\right) \right]. \quad (50)$$

The coefficient of integration, C , must now be chosen such that we can match the solution on the left-hand side of the origin to the evanescent WKB solution. We have required $u'(x) \ll 1$, so an oscillatory $u(x)$ can be modelled as ϵe^{2ix} with $\epsilon \ll 1$ (plus a constant which can be safely ignored) in which case:

$$y(x) = e^{-ix+u(x)} = e^{-ix} e^{\epsilon e^{2ix}} \simeq e^{-ix} (1 + \epsilon e^{2ix}) = e^{-ix} + \epsilon e^{ix}. \quad (51)$$

These correspond to the WKB solutions, which are approximately of the form $c_1 e^{-ix} + c_2 e^{ix}$ near the origin. We require that the WKB solution matched on the

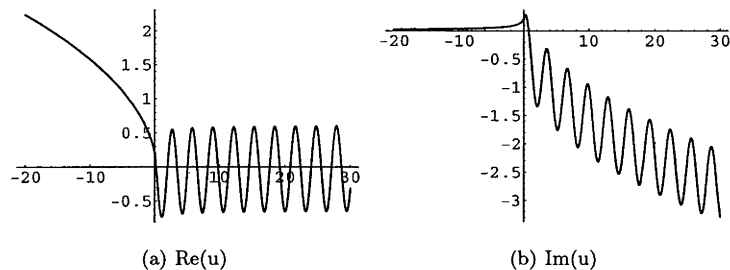


Figure 6: Real and imaginary components of $u'(x)/A$ versus x for $C = A(1 + i)\pi^{1/2}/8$. The function is oscillatory for $x \rightarrow +\infty$, but not for $x \rightarrow -\infty$.

left-hand side have $c_2 = 0$ because the corresponding term grows exponentially for large negative x . We therefore must have $\epsilon \rightarrow 0$ as $x \rightarrow -\infty$. Using the asymptotic expansion of $\text{erfc} = 1 - \text{erf}$, as given by equation 7.1.23 of [38], we find the $x \rightarrow -\infty$ limit of equation (50), allowing us to express this matching condition as:

$$C = \frac{A}{8}(1 + i)\sqrt{\pi}. \quad (52)$$

Then we have a solution for y which is asymptotically of the form:

$$y = P(x) \left(e^{-ix} + e^{ix} \frac{A\sqrt{\pi}(1 - i)}{4} \right) \quad (53)$$

for $x \gg 1$, with $P(x)$ a slowly varying function. The phase matching condition is given by finding the nodes of these waves, which fixes the WKB phase at $x = 0$:

$$\phi_0 = \frac{-i}{4} \log\left(\frac{(1 + i)A\sqrt{\pi}}{8}\right). \quad (54)$$

6.9 Finding wavemodes

Global modes are found in the usual way: we look for paths C in the complex plane joining the axis and boundary where $\int_B \alpha(x)dx$ is real for any sub-path B of C . These paths will be WKB solutions if the integral $\int_C \alpha(x)dx = \int_{[0,1]} \alpha(x)dx$ which can be guaranteed if there are no singularities of our differential equation coefficients in the region. In particular, this requires that the circular path $C - [0, 1]$ does not enclose any Stokes points. The quantisation condition is supplied by requiring the correct behaviour at boundaries. At the

origin the WKB wavemode must be matched to a Bessel function, and this gives the condition $\phi|_{x=0} = \pi(1/4 + m/2)$. At the outer boundary of the plasma, we require $v_r = 0$ (fixed plasma boundary), which leads to $\phi|_{x=1} = \pi/2$.

The rays corresponding to localised modes start at the axis or outer boundary of the plasma and have trajectories which trace along anti-Stokes lines to a Stokes point. They are then evanescent on one side of the continuing anti-Stokes line, so it must be possible to draw a path connecting the relevant segment of the Stokes point neighbourhood to the other boundary without crossing a Stokes line. For Stokes points of the form $Q(x) = a + bx^{\frac{1}{2}}$, which are present in this analysis, we have a complex phase matching criterion. The phase integral between the Stokes point and the boundary is then required to be complex for matching to occur. This means that we cannot follow anti-Stokes lines exactly, along which the phase integral is real, to join the boundary and the Stokes point. The complex portion of the phase leads to a correction to the path which must be taken into account, but which is logarithmically small in the semiclassical limit.

6.10 Application of the WKB method to the small shear incompressible case

For explicit studies, we use a small shear test case:

$$B_p(r) = \frac{B_{p0}}{1 - r\delta} = \frac{\frac{7}{24}}{1 - 0.1r}, \quad (55)$$

$$B_z(r) = 1, R = \frac{20}{7}, n = 10, m = 1, r_p = 1, q(r) = 0.12(1 - 0.1r) \quad (56)$$

The WKB trajectories in the complex τ plane were determined by solving the differential equation

$$\frac{dx}{d\tau} = \alpha(x)^*. \quad (57)$$

for real τ so that $\alpha(x)dx \in \mathcal{R}$. Where the ray crosses a branch cut, the branches on which α is evaluated on either side of the cut must be chosen so that α is continuous along the ray.

In figure 7, we draw the six qualitatively different kinds of paths which lead to quantisation:

- Two which join the axis and the plasma boundary,
- two which join the axis and a Stokes point
- and two which join the plasma boundary and a Stokes point.

These paths occur in pairs because there are two relevant branches of the dispersion relation. It is never possible in practice to form global modes on the other branch of the dispersion relation: the rays inevitably escape towards complex infinity in the positive imaginary direction.

The process of accurately determining these paths begins with the choice of two reasonable initial guesses for the frequency ω . For each guess, we find the ray from the Stokes point or (if we are searching for a path that joins the two boundaries) from the axis and determine where it crosses the line $\text{Real}(x) = 0$ or $\text{Real}(x) = 1$. We then use a secant search method to seek a value of ω where the path intersects at $\text{Im}(x) = 0$, and thus joins the originating boundary point either to the Stokes point or to the other boundary.

The eigenvalues are displayed in figure 8, together with the numerical result from a code based on [34]. The spectrum is qualitatively similar to a fork structure, but also shares the features of the original simple model. Note that the double loci (running parallel to each other in an arc) are still present in this model.

The nature of the difference between the two branches of the double locus can be seen in equation (30), and the form of the dispersion function for large enough α . Here we have two solutions for $\alpha(\omega)$ such that $\alpha_1 \simeq -\alpha_0$, and the two WKB solutions consist of waves of opposite helicity. Finite pressure gradients in this equilibrium result in waves of opposite helicity having slightly different frequencies.

6.11 Effects of the $\gamma \rightarrow \infty$ approximation

The reason why we see a pair of loci in 1(e), rather than the single locus usually depicted for compressible spectra (e.g. figure 1(a)) is that in this incompressible model (the limit $\gamma \rightarrow \infty$) there are two classes of wavemodes present which can be excited at the Alfvén frequency. In a uniform field these wavemodes are degenerate: they oscillate at the same frequency. However the two frequencies are split when the plasma contains currents perpendicular to the magnetic field (i.e. in non-force-free plasmas). In the compressible model at low β , these two degrees of freedom correspond to the slow (magnetosonic) and Alfvén wavemodes and the ratio between slow frequencies and Alfvén frequencies is of order $\beta^{1/2}$.

Force-free models are important special cases, in which pairs of loci of eigenvalues coincide. The $\gamma \rightarrow \infty$ approximation will still result in unphysical eigenmodes. We note the paper of Ryu and Grimm [30], which uses this incompressibility assumption to analyse a case with finite pressure gradients where we should see a double locus structure. We nevertheless see a simple fork struc-

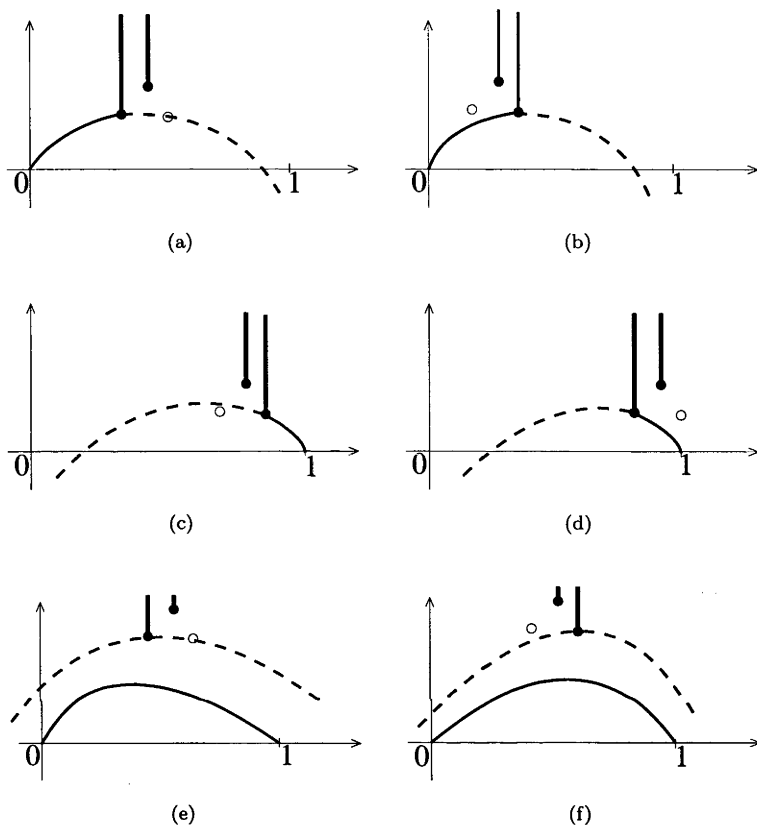


Figure 7: Stokes diagrams on the complex plane for the dispersion relation α , with a horizontal real axis and vertical imaginary axis. The plasma axis is at the origin and the plasma edge is on the real line at $Re(\tau) = 1$. Branch points are shown as closed circles where they lie on the sheet being plotted, and open circles where they do not. The branch cuts, shown as thick vertical lines, are chosen to avoid intersection with the rays, so that the ray propagates entirely on one sheet. The semiclassical rays are shown as solid curves, and the Anti-Stokes lines are plotted as dashed lines. Rays in subfigures 7(a), 7(c) and 7(e) propagate on a different sheet of the function than rays in subfigures 7(b), 7(d) and 7(f), and therefore see a different branch point structure.

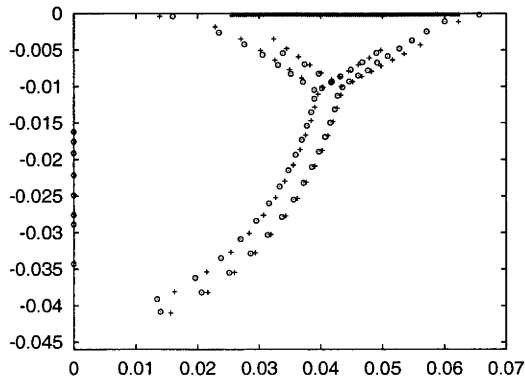


Figure 8: The resistive spectrum from numerical solution of the MHD equations (circles) compared to the WKB result (plus signs). The ideal Alfvén continuum is represented by a grey bar on the real axis. Plasma parameters are given by equation (56) and $S = 3 \times 10^4$.

ture. We believe that the splitting effect is rather small in this case, so that what looks like one fuzzy locus is in fact a double locus.

6.12 Conclusions

In plasma physics an assumption of incompressibility is often justified because the parallel dynamics of the plasma and the fluid compression across the field are much less important than the forces due to the magnetic field. For example, incompressibility does not generally affect ideal MHD marginal stability (but this does not extend to resistive MHD [39]).

Two incompressible resistive MHD models were compared with the physical compressible model by analysis of their spectra. For the first model, where the ratio of specific heat is taken to infinity, we expect from local analysis to find two types of wavemodes present at the Alfvén frequency. In the second model where we again set $\gamma \rightarrow \infty$, the parallel plasma inertia is set to zero, and we expect only one Alfvénic mode to be present in the spectrum, corresponding to the physical case. Numerical computation of the spectra of a magnetic shear-free plasma confirms that the second model reproduces most of the eigenmodes associated with the Alfvénic model correctly. The first model has twice as many modes present at the Alfvén timescale.

It is noted that in general most of the modes resolved do not correspond to Alfvén modes and have no physical significance. The shape of an incompressible spectrum for a more general model, with shear present, was determined numerically and by WKB analysis. The unusual nature of the local dispersion relation

leads to a complex structure of loci. The resulting spectrum included the ‘double locus’ of the zero shear model and also demonstrated the fork structure that is seen generically for stable resistive MHD spectra.

There are many qualitative features of the resistive Alfvén spectrum that can be reproduced by simply setting $\gamma \rightarrow \infty$. Unfortunately, physical wavemodes and frequencies are not well modelled in this approximation. The stable part of the ideal Alfvén spectrum is irreparably mixed with spurious modes in this limit. However, by using an anisotropic mass density tensor, an incompressibility constraint can be introduced while preserving the Alfvén modes.

7 Spector3D

7.1 Introduction

Stability with respect to large scale plasma perturbations is critical to the design and operation of fusion relevant experiments: instabilities often limit plasma performance, and can occasionally be so violent that they damage the surrounding hardware. The ideal and resistive MHD models capture much of the physics necessary to diagnose these relatively fast, large scale instabilities, and are simple enough that stability can often be explored analytically. However, numerical modelling is necessary to get a complete picture of plasma stability, especially in non-axisymmetric plasmas. Well tested codes for linear ideal MHD analysis of 3D configurations exist [4] [2], but there is a need for a 3D fluid stability code which includes other effects. For example, the NCSX experiment [1] is expected to generate a substantial proportion of its transform from bootstrap current, and its stability to tearing modes is of some interest. There are also equilibria for which ideal MHD seems to be overly pessimistic: in some configurations of LHD, where high wavenumber instabilities with small growth rates are predicted theoretically at relatively low values of β , there is no experimental evidence of hard β limits or strong MHD activity [13]. It has been suggested that stabilising kinetic effects may be playing a role here.

3D nonlinear fluid codes [40] currently exist, and a code of this type is necessary to examine the saturated or disruptive dynamics of the plasma. Even though linear behaviour away from an equilibrium can also be examined in a nonlinear code, they are not necessarily the best tool for this task as they usually have more limited spatial resolution. Also, nonlinear codes have difficulty describing the plasma at low levels of dissipation because numerical stability can only be guaranteed by imposing a gridsize dependent damping. Stability or spectral codes are generally faster and can represent plasmas with low levels of dissipation. Well developed ideal MHD linear codes have produced results with a high level of consistency and accuracy: TERPSICHORE, for example, has been included in an automatic configuration optimisation loop in the development of NCSX [41]. Linear codes are often used as a tool to bridge the gap between the limited domain where analytical considerations are sufficient and real world configurations.

In this chapter we present the formulation of a linear resistive MHD code, Spector3D, and describe the numerical method. We discuss the current form of Spector3D, and the reasons for this particular formulation. Benchmarking results will be presented against 2-D and 3-D ideal MHD codes, as well as against 2-D resistive MHD results, and against analytic models of tearing modes in 3-D

equilibria.

7.2 Formulation of Spector3D

Unlike in the ideal MHD case, we have no convenient variational form of the equations and must determine the response of the plasma to small amplitude perturbations by direct solution of the time evolution equations for the fluid and the fields. Specifically, the equations we wish to solve are the linearised, compressible, 3D resistive MHD equations, with no equilibrium flows, most conveniently written in dimensionless form:

$$\rho^* \frac{\partial}{\partial t}(\mathbf{v}) = (\nabla \times \mathbf{b}) \times \mathbf{B} + (\nabla \times \mathbf{B}) \times \mathbf{b} - \nabla p, \quad (58)$$

$$\frac{\partial p}{\partial t} = -\mathbf{v} \cdot \nabla P - \gamma P \nabla \cdot \mathbf{v}, \quad (59)$$

$$\frac{\partial \mathbf{b}}{\partial t} = \nabla \times (\mathbf{v} \times \mathbf{B}) - \nabla \times (\eta \nabla \times \mathbf{b}), \quad (60)$$

where \mathbf{v} , p and \mathbf{b} are the perturbed velocity, pressure and magnetic field, and P and \mathbf{B} are the background pressure and magnetic field. The dimensionless density profile $\rho^* = \rho(r)/\langle \rho \rangle$ is included in equation (58) in order to account for variations in plasma density across the radius. The quantity γ , the plasma compressibility, is usually set equal to 5/3, as for an ideal gas, but often its value does not strongly affect the quantities of interest, and it may then be chosen for numerical convenience. We can attempt to eliminate one component of \mathbf{b} in order to impose $\nabla \cdot \mathbf{b} = 0$, as in [34], but the need to include modes with $m = 0$ and $n = 0$ simultaneously (unlike in the 1 or 2-D case) leads to significant code complication, so although we initially implemented this method, we eventually decided to represent the perturbing magnetic field through the vector potential, so that $\mathbf{b} = \nabla \times \mathbf{a}$. We then rewrite Ampère's law as

$$\frac{\partial \mathbf{a}}{\partial t} = (\mathbf{v} \times \mathbf{B}) - \eta \nabla \times (\nabla \times \mathbf{a}). \quad (61)$$

This automatically leads to $\nabla \cdot \mathbf{b} = 0$ because the divergence of a curl is zero. Boundary conditions are given by the imposition of a conducting wall at the plasma edge, and analyticity at the origin.

7.3 Coordinate system and equilibria

Spector3D is restricted to the analysis of equilibria with a complete nested set of flux surfaces, but since a design requirement of most stellarators is that magnetic islands are not significantly large, this is not a major practical limitation. This restriction to stellarators with nested flux surfaces considerably simplifies the numerics, and allows us to use the efficient and well-characterised VMEC code [6] to produce stellarator equilibrium descriptions. Even in a fairly well-optimised stellarator there are small remnant islands which would be present in an exact and complete MHD equilibrium analysis; these islands manifest in the VMEC output as singular currents at rational surfaces. This is a general consequence of requiring a 3-D configuration to have nested flux surfaces ([42], page 148). These (unphysical) singular currents are especially significant where they resonate with the the plasma perturbation under consideration.

The assumption of nested flux surfaces allows us to choose an index, s , across these surfaces as our radial coordinate. We then have a certain freedom of choice in the toroidal and poloidal coordinate system. Further simplification and improved accuracy can be achieved by specializing to a straight field line coordinate system, in this case, Boozer [43] coordinates (there are other possibilities [42]). We use an external program (part of TERPSICHORE [2]) to convert equilibrium quantities from the VMEC coordinate system into Boozer coordinates, which are distinguished from other straight field line coordinates by the choice of the Jacobian:

$$\mathcal{J}_{\text{Boozer}} = \sqrt{g_B} = f(s) \frac{1}{|B|^2} \quad (62)$$

where $f(s)$ is constant on each flux surface. The poloidal coordinate, θ , and the toroidal coordinate, ζ , run from zero to 2π . The flux surface label s runs over the range $[0, 1]$ between the magnetic axis and the plasma edge. Because of the conventional choice of direction for the angles θ and ζ , and the conventional order assigned to the triplet (s, θ, ζ) , this is a left-handed coordinate system. One consequence is that the sign of the Jacobian is negative.

In Boozer coordinates, the contravariant and covariant representations of the magnetic field are

$$\mathbf{B} = \frac{\dot{\Psi}_{pol}(s)\mathbf{e}_\theta + \dot{\Psi}_{tor}(s)\mathbf{e}_\zeta}{2\pi\sqrt{g_B}} \quad (63)$$

and

$$\mathbf{B} = -\nu\mathbf{e}^s + \frac{I_{tor}}{2\pi}\mathbf{e}^\theta + \frac{I_{pol}}{2\pi}\mathbf{e}^\zeta \quad (64)$$

respectively, where the dot denotes a derivative with respect to the radial coordinate s . Checking that the two representations of the magnetic field are equivalent can be used to verify that the Boozer reconstruction of the equilibrium solution is sufficiently accurate. The covariant form is used to find the equilibrium current through $\nabla \times \mathbf{B}$:

$$\mathbf{J} = \frac{(\dot{I}_{pol}(s) - 2\pi \frac{\delta \nu}{\delta \zeta}) \mathbf{e}_\theta + (\dot{I}_{tor}(s) - 2\pi \frac{\delta \nu}{\delta \theta}) \mathbf{e}_\zeta}{2\pi \sqrt{g_B}}. \quad (65)$$

It can be shown by considering MHD pressure balance that ν satisfies

$$\mathbf{B} \cdot \nabla \nu = \dot{p} \left[\frac{\langle \sqrt{g_B}^{-1} \rangle^{-1}}{\sqrt{g_B}} - 1 \right], \quad (66)$$

which can be conveniently solved for ν in Fourier space,

$$\nu_{mn}(s) = 0 \quad \text{for } m, n = 0, \quad (67)$$

$$= 2\pi \dot{p} \frac{(\sqrt{g_B})_{mn}(s)}{i(m\dot{\Psi}_{pol}(s) - n\dot{\Psi}_{tor}(s))} \quad \text{otherwise.} \quad (68)$$

Here the Fourier representation of our quantities is set to

$$f(s, \theta, \zeta) = \sum_{m, n \in [-\infty, \infty]} f_{mn}(s) e^{im\theta - in\zeta} \quad (69)$$

for any scalar or vector function $f(s, \theta, \zeta)$. The denominator has a zero at rational surfaces, leading to a singular current unless $J_{mn} = 0$ on the relevant rational surface: we should be able to accurately resolve these currents in Boozer coordinates, unlike in other schemes these singular currents will not appear as explicitly.

7.4 Numerical equilibria and interpolation

The accuracy of any stability analysis is inevitably bounded by the accuracy of the equilibrium specification. The numerical equilibria used by Spector3D are produced by VMEC and a Boozer coordinate mapper, and in general are accurate to considerably less than machine precision. The input to the stability code consists of the metric tensor specified on a three dimensional grid with uniform spacing in radial position and in toroidal and poloidal angle, along with a set of flux surface quantities: the poloidal and toroidal magnetic fluxes, the pressure profile and the poloidal and toroidal current densities. Because of the possibly large number of radial grid points needed in the stability analysis, and the desirability of accumulating grid points around rational surfaces, we need to

have access to values of equilibrium quantities at arbitrary radial positions. This interpolation is achieved by using cubic splines to represent appropriately scaled equilibrium quantities, so that any singularities at the origin are accounted for. The accuracy of evaluation of equilibrium quantities is then second order with respect to the equilibrium grid spacing, which is consistent with the order of accuracy of the input.

Near the magnetic axis, the output from VMEC generally satisfies the equilibrium conditions of MHD less exactly than it does elsewhere, and so this region of the plasma requires careful treatment in order that the linearised equations represent the physics. In particular the first one or two grid points are problematic. Because VMEC uses the normalised toroidal flux as its radial coordinate, the region inside the second grid point corresponds to about ten percent of the plasma radius for a typical VMEC run with 100 grid points. This region is particularly significant for modes with small poloidal mode number, because of the scaling of the perturbation amplitude near the origin (see section 7.7). One method [44] for producing improved representations of the magnetic field near the origin is to use the known analytic behaviour of equilibrium quantities and smoothing splines to produce self-consistent magnetic surfaces. For cases where mode amplitudes near the axis are small it is relatively simple to place an artificial conductive boundary condition on a flux surface close to the axis.

7.5 Integrating the resistive MHD equations

It is usually simpler to justify a numerical discretisation of a set of differential equations via the integral (or weak) form of the equations rather than by proceeding directly from the equations themselves. The Finite Element Method is based on this approach, as is the rigorous justification for Finite Difference methods [45]. We consider a generalised vector differential eigenvalue problem

$$\lambda \mathcal{A} \mathbf{x} = \mathcal{B} \mathbf{x} \quad (70)$$

which represents the class of linear equations of interest. Apart from specifying the operators \mathcal{A} and \mathcal{B} it is also necessary to specify the spaces on which they act, in which the solutions $\mathbf{x} \in \mathbf{X}$ are found, satisfying appropriate boundary and smoothness conditions. The operators map into some space which we label \mathbf{Y} .

To produce the weak form of our eigenvalue equation, we first multiply the equation by some $\mathbf{y} \in \mathbf{Y}$, and integrate the equation over the relevant volume

to obtain

$$0 = \int dV \lambda \mathbf{y} \mathcal{A} \mathbf{x} - \mathbf{y} \mathcal{B} \mathbf{x} = \lambda a(\mathbf{x}, \mathbf{y}) - b(\mathbf{x}, \mathbf{y}). \quad (71)$$

And this suggests a reformulation of the differential equations as the problem:

Find a pair $(\lambda \in \mathcal{C}, \mathbf{x} \in \mathbf{X})$ with $\mathbf{x} \neq 0$ such that for all $\mathbf{y} \in \mathbf{Y}$ we have

$$\lambda a(\mathbf{x}, \mathbf{y}) = b(\mathbf{x}, \mathbf{y}) \quad (72)$$

This is known as a weak formulation of the differential equations.

The discretisation of the problem is achieved by considering finite dimensional subspaces $X_h \subset \mathbf{X}$ and $Y_h \subset \mathbf{Y}$ spanned by $(\phi_i, i \in 1..N)$ and $(\xi_i, i \in \{1..N\})$, and projecting the problem into these finite dimensional subspaces. This is known as the *Galerkin* method:

Find a pair $(\lambda_h \in \mathcal{C}, \mathbf{x}_h \in X_h)$ such that for all $\mathbf{y}_h \in Y_h$ we have

$$\lambda_h a(\mathbf{x}_h, \mathbf{y}_h) = b(\mathbf{x}_h, \mathbf{y}_h) \quad (73)$$

We can then expand the problem in terms of the coefficients of the basis vectors,

$$\mathbf{x}_h = \sum_{i=1, N} c_i \phi_i \quad (74)$$

for a set of complex numbers c_i . We then have a finite dimensional linear eigenvalue problem,

$$\lambda_h \sum_{i=1, N} c_i a(\phi_i, \xi_j) = \sum_{i=1, N} c_i b(\phi_i, \xi_j) \quad \text{for all } j \in \{1..N\}. \quad (75)$$

The subscript h is included here as a figure of merit to describe how finely our space is discretised; in our case it describes radial grid spacing and the effective scale length from the cutoff in Fourier space.

In order for the discretisation to be useful for spectral studies, the spectrum of the finite dimensional problem must a good approximation to that of the infinite dimensional problem, and to be specific about this requirement, we consider the criteria expounded in [46]:

1. If λ is an eigenvalue of equation (72), do eigenvalues λ_h of equation (73) exist such that $\lambda = \lim_{h \rightarrow 0} \lambda_h$?
2. Are all the limit points λ of λ_h as $h \rightarrow 0$ eigenvalues of equation (72) ?

3. Do the eigenfunctions \mathbf{x}_h of equation (73) tend towards the function \mathbf{u} of equation (72)?
4. Is it possible to obtain error estimates between the eigenelements of equation (72) and equation (73) ?

These considerations can be addressed theoretically for a wide class of model problems. The essential result is that if the discretised operator is a good approximation in some sense to the full operator, we can satisfy the above criteria. The precise criterion for a good discretisation can be expressed in terms of limits of the discretisation error, as $h \rightarrow 0$. To satisfy this condition, we must choose finite elements which are of high enough order to represent the derivatives in our operator. This is not a sufficient condition, however, and the discretisation must be chosen carefully in order to avoid ‘spectral pollution’, in which a large number of spurious eigenvalues are found which cannot be resolved by improving the mesh resolution. Previous work on ideal and resistive MHD suggests simple physically motivated conditions which can be used to find an appropriate discretisation, which we consider in the next section.

7.6 The finite element method applied to linearized resistive MHD

We now discretise our equations using a finite element method, with an overall formulation which is similar to the 2D resistive code CASTOR [3].

In this formulation, the perturbing quantities are expanded in a Fourier series in the toroidal and poloidal directions, and by finite elements across the radius. This expansion can be written as

$$f(s, \theta, \zeta) = \sum_{m,n,l} f_{m,n,l} F_l(s) e^{im\theta - in\zeta} \tag{76}$$

where l is an index for the one dimensional finite elements $F_l(s)$. In practise we must restrict the sum over m and n so that the sum is over a finite number of terms.

A good choice of discretisation is vital for this problem because of the phenomenon of ‘spectral pollution’. This occurs in the presence a non-compact spectrum: in our case the spectrum of fast magneto-sonic wavemodes is non-compact because the mode frequency increases with radial wavenumber. The pollution manifests as a very large number of spurious radially oscillatory eigenmodes in the numerical spectrum: it often becomes impossible to distinguish any physically relevant eigenmodes, and the effect cannot be resolved by increasing the radial resolution. The cause of this pollution is a spurious numerical

coupling between wavemodes of very different frequency [46]. Such coupling can be induced by ‘numerical divergence’, which is often a consequence of a poorly discretised representation of a divergence-free quantity. In our particular problem, we are particularly concerned that no compression of the magnetic field be introduced by our discretisation. It is therefore necessary for the large class of approximants which represent incompressible modes to satisfy $\nabla \cdot (\mathbf{v}B^2) = 0$ exactly. We also require that the magnetic field satisfy $\nabla \cdot \mathbf{b} = 0$, but this is always the case in our vector potential representation. For a poor choice of discretisation, it is possible that representations of incompressible wavemodes can only satisfy $\nabla \cdot (\mathbf{v}B^2) = 0$ at a small number of radial points per grid interval. The result is an oscillating value of $\nabla \cdot (\mathbf{v}B^2)$ in the representation of any smooth wavemode. Because the forces due to the oscillatory component are proportional to the wavenumber, the spurious forces may not converge to zero as we increase the grid resolution, and our approximation may never converge.

We examine the divergence of $\mathbf{v}B^2$ in terms of the contravariant components.

$$\nabla \cdot \left(\frac{\mathbf{v}}{\sqrt{g_B}} \right) = \nabla \cdot \left(\frac{\mathbf{v}^s \mathbf{e}_s + \mathbf{v}^\theta \mathbf{e}_\theta + \mathbf{v}^\zeta \mathbf{e}_\zeta}{\sqrt{g_B}} \right) = \frac{1}{\sqrt{g_B}} \left(\frac{\partial}{\partial s}(\mathbf{v}^s) + \frac{\partial}{\partial \theta}(\mathbf{v}^\theta) + \frac{\partial}{\partial \zeta}(\mathbf{v}^\zeta) \right) = 0 \quad (77)$$

We set $\mathbf{v}^s = v_1$, $\mathbf{v}^\theta = v_2$ and $\mathbf{v}^\zeta = v_3$, where v_1 , v_2 and v_3 are piecewise polynomial in radius, and Fourier expanded in the angular coordinates. It is then possible to satisfy equation (77) exactly for piecewise polynomial v_1 , v_2 and v_3 as long as the order of the polynomial v_1 is one higher than that of v_2 and v_3 . It is also useful to set the direction of one velocity component to be along the field line:

$$\mathbf{v}^i = \left(v_1, v_2 + \dot{\Psi}_{pol} v_3, \dot{\Psi}_{tor} v_3 \right) \quad (78)$$

For the representation of the magnetic field, it is desirable that we be able to take the necessary derivatives induced by Newton’s law. We require that the magnetic field be smooth, and be divergence-free. This can be achieved by representing the vector potential \mathbf{a} in covariant components, piecewise polynomial in radius, with a_s one order lower than a_θ and a_ζ .

$$\mathbf{a}_i = (a_1, a_2, a_3) \quad (79)$$

We then have seven scalar variables ($v_1, v_2, v_3, p, a_1, a_2, a_3$) representing the physical quantities ($\mathbf{v}, p, \mathbf{a}$), which are discretised using finite elements. The finite elements must be chosen with the correct order of smoothness so that we can take the spatial derivatives which are present in equations (58), (59) and

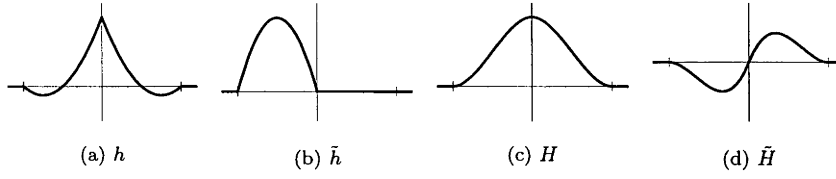


Figure 9: Finite element basis functions for radial discretisation.

(61). In particular, we require the second order derivatives of a_2 , a_3 and v_1 , but only the first order derivatives of the other variables. This can be satisfied by representing v_1 , a_2 and a_3 by cubic spline functions, and v_2 , v_3 , p and a_1 by quadratic Hermite polynomials. The perturbed pressure is represented by a quadratic Hermite polynomial. The cubic Hermite elements are

$$H_j(s) = \begin{cases} 3 \left(\frac{s-s_{j-1}}{s_j-s_{j-1}} \right)^2 - 2 \left(\frac{s-s_{j-1}}{s_j-s_{j-1}} \right)^3, & s_{j-1} \leq s \leq s_j, \\ 3 \left(\frac{s_{j+1}-s}{s_{j+1}-s_j} \right)^2 - 2 \left(\frac{s_{j+1}-s}{s_{j+1}-s_j} \right)^3, & s_j \leq s \leq s_{j+1}, \\ 0 & s_j \notin [s_{j-1}, s_{j+1}], \end{cases} \quad (80)$$

and

$$\tilde{H}_j(s) = \begin{cases} (s-s_j) \left(\frac{s-s_{j-1}}{s_j-s_{j-1}} \right)^2 & s_{j-1} \leq s \leq s_j, \\ (s-s_j) \left(\frac{s-s_{j+1}}{s_{j+1}-s_j} \right)^2 & s_j \leq s \leq s_{j+1}, \\ 0 & s_j \notin [s_{j-1}, s_{j+1}], \end{cases} \quad (81)$$

and the quadratic Lagrange elements are

$$h_j(s) = \begin{cases} 2 \left(s - \frac{s_j+s_{j-1}}{2} \right) \frac{(s-s_{j-1})}{(s_j-s_{j-1})^2} & s_{j-1} \leq s \leq s_j, \\ 2 \left(s - \frac{s_{j+1}+s_j}{2} \right) \frac{(s-s_{j+1})}{(s_{j+1}-s_j)^2} & s_j \leq s \leq s_{j+1}, \\ 0 & s_j \notin [s_{j-1}, s_{j+1}], \end{cases} \quad (82)$$

and

$$\tilde{h}_j(s) = \begin{cases} 4 \frac{(s-s_{j-1})(s_j-s)}{(s_j-s_{j-1})^2} & s_{j-1} \leq s \leq s_j, \\ 0 & s_j \notin [s_{j-1}, s_j]. \end{cases} \quad (83)$$

We note that other choices of discretisation are possible, and several variants of the formulation were devised and implemented. In particular, in the original code implementation we represented the perturbed magnetic field \mathbf{b} , directly, with satisfactory results, but using the vector potential leads to a more elegant formulation.

7.7 Boundary conditions

For the sake of simplicity, we have implemented a fixed boundary code. Physically this is equivalent to placing an infinitely conductive wall at the last closed flux surface. This boundary condition is given by requiring that the velocity normal to the wall and the electric field parallel to the wall vanish:

$$\mathbf{n} \cdot \mathbf{v} = 0, \quad (84)$$

$$\mathbf{n} \times \mathbf{E} = \lambda \mathbf{n} \times \mathbf{a} = 0, \quad (85)$$

as we have chosen $\lambda \mathbf{a} = \mathbf{E}$. Because of the choice of the finite element basis, these can be expressed as the essential boundary conditions

$$\mathbf{a}_\zeta|_{r=1} = \mathbf{a}_\theta|_{r=1} = \mathbf{v}^r|_{r=1} = 0 \quad (86)$$

Near the magnetic axis we need to impose analyticity on the perturbed quantities. To find the appropriate condition, we Taylor expand the Fourier sum near the magnetic axis. The cut torus of the stellarator can be continuously deformed onto a straight cylinder, with the magnetic axis and the cylindrical axis brought together, so the analyticity condition is the same as that of a vector valued function in cylindrical coordinates,

$$\mathbf{v}(r, \theta, z) = \sum_{m=-\infty}^{\infty} \sum_{k=0}^{\infty} \left(\hat{\mathbf{r}} A_{mk}(z) r^{2k+|m-1|} e^{im\theta} + \hat{\boldsymbol{\theta}} B_{mk}(z) r^{2k+|m-1|} e^{im\theta} + \hat{\mathbf{z}} C_{mk}(z) r^{2k+|m|} e^{im\theta} \right) \quad (87)$$

and for the purposes of analyticity the cylindrical coordinate z is equivalent to the toroidal angle ζ . Scalar functions take the form

$$p = \sum_{m=-\infty}^{\infty} \sum_{k=0}^{\infty} D_{mk}(z) r^{2k+|m|} e^{im\theta}. \quad (88)$$

The VMEC coordinate system has $r \simeq s^{1/2}$, $\mathbf{e}_s \simeq s^{-1/2}\hat{\mathbf{r}}$ and $\mathbf{e}_\theta \simeq s^{1/2}\hat{\boldsymbol{\theta}}$ so that the contravariant components of a vector can be written

$$v^s = \sum_{m=-\infty}^{\infty} \sum_{k=0}^{\infty} A_{mk}(z) s^{k+1/2+||m|-1|/2} e^{im\theta}, \quad (89)$$

$$v^\theta = \sum_{m=-\infty}^{\infty} \sum_{k=0}^{\infty} B_{mk}(z) s^{k-1/2+||m|-1|/2} e^{im\theta}, \quad \text{and} \quad (90)$$

$$v^z = \sum_{m=-\infty}^{\infty} \sum_{k=0}^{\infty} C_{mk}(z) s^{k+|m|/2} e^{im\theta} \quad (91)$$

and the covariant components can be expressed as

$$v_s = \sum_{m=-\infty}^{\infty} \sum_{k=0}^{\infty} D_{mk}(z) s^{k-1/2+||m|-1|/2} e^{im\theta}, \quad (92)$$

$$v_\theta = \sum_{m=-\infty}^{\infty} \sum_{k=0}^{\infty} E_{mk}(z) s^{k+1/2+||m|-1|/2} e^{im\theta}, \quad \text{and} \quad (93)$$

$$v_z = \sum_{m=-\infty}^{\infty} \sum_{k=0}^{\infty} F_{mk}(z) s^{k+|m|/2} e^{im\theta}. \quad (94)$$

The most singular term is the $m = \pm 1$ components of v_s and v^θ , which contain a factor of $s^{-1/2}$. In our implementation we do not resolve these singularities at the origin, as we found good convergence in radial grid-number for test cases based on analytic equilibria, indicating that a polynomial approximation of these singularities near the origin did not introduce large errors.

7.8 Symmetries and mode coupling

In the case of axisymmetric equilibria, the continuous rotation symmetry (or corkscrew symmetry in the helical case) leads to a ‘good quantum number’, and the problem of stability separates so that each toroidal wave number, n , can be considered individually. Stellarators do not have an (exact) continuous symmetry, and therefore the coupling between different toroidal wave numbers must be considered. However, most stellarators have a finite rotational symmetry group, whose size is the number of field periods of the device. This is central to the understanding of stability in stellarators, as pointed out in [47]:

It is not obvious at first glance that there is a stability problem (for stellarators) since at least some of these (equilibrium) codes determine the equilibrium by finding the minimum potential energy of the system. Such equilibria should be stable by definition unless the chosen minimization fails to lead to the lowest energy state. In actual practice, most equilibrium configurations are prescribed to

have periodic behaviour over the magnetic field period ... Thus, the equilibrium should be stable with respect to any perturbation that does not destroy this helical periodicity. For this reason, stability is usually thought of as the question of whether relaxation of this periodicity constraint can lead to a lower energy state.

The nested flux surface condition is an additional constraint on the minimisation in equilibrium codes, and can be broken by resistive perturbations, which may access a lower energy state by introducing magnetic islands. However, an ideal perturbation with a toroidal wavenumber which is a multiple of the number of field periods of the device will not break either the discrete symmetry or the nested flux surface condition, and should therefore not be relevant from the point of view of stability analysis. In this work we will limit our consideration of resistive modes to those which break the discrete symmetry of the device, in order to avoid problems that might arise when our perturbing wavefunction is resonant with the singular currents of a numerical equilibrium.

In Fourier space, the discrete symmetry induces a condition on pairs of toroidal wavenumbers which must be satisfied for corresponding pairs of basis functions to be coupled together by inhomogeneities in the equilibrium. As a result the toroidal wavenumbers separate into classes known as mode families. For a pair of Fourier components with toroidal wave numbers n and n' to couple we require $n = n' + ik$ for some integer i , with k equal to the number of field periods of the device. Most stellarators also possess 'stellarator symmetry' [25] which corresponds to a simultaneous reversal of the toroidal and poloidal angles of the device, and corresponds to a time reversal symmetry in the field line Hamiltonian. This does not induce a restriction on the coupling in Fourier space, however we would expect that eigensolutions which are resonant with the toroidal field variation (coupling to $n = 0$ or $n = k/2$) could be classified as either symmetric or antisymmetric under stellarator symmetry.

7.9 Calculation of the matrix elements

The matrix elements of A and B are calculated by substituting the finite element representation of the variables and weighting functions into the integrated formulation of equations (58), (59) and (60). The integrals can be manipulated easily by hand in the usual coordinate-free vector notation. However, in order to perform the final evaluation in our curvilinear coordinate system, the geometry must be explicitly included in terms of the metric tensor g_{ij} , and its Jacobian J . The operators needed for these calculations can be expressed simply in these coordinates so long as the operands are in the correct representation (Chapter

2 of [42] presents the formalism nicely.):

$$(\nabla \times \mathbf{a})^i = \frac{1}{\sqrt{g}} \epsilon^{ijk} \frac{\partial}{\partial x_j} a_k, \quad (95)$$

$$(\mathbf{a} \times \mathbf{b})_i = \sqrt{g} \epsilon_{ijk} a^j b^k, \quad (96)$$

$$(\mathbf{a} \times \mathbf{b})^i = \frac{1}{\sqrt{g}} \epsilon^{ijk} a_j b_k. \quad (97)$$

Other choices of operands will involve the metric tensor g_{ij} or its inverse. The choice of representation of the perturbing quantities in co- or contra-variant form and the choice of scaling factor therefore makes a significant impact on the simplicity of the expression for the matrix elements. Spectral pollution considerations suggest a particular choice for the representation of our perturbing quantities, and it is pleasing, but not coincidental, that this leads to one of the simplest expressions for the matrix elements.

Once we have the vector operator and equilibrium quantities explicitly described, we can perform the integration over the angles θ and ζ symbolically; we then express the result in terms of the Fourier transform of various equilibrium quantities. The radial integration uses a high order Gaussian scheme which is exact for our piecewise polynomial integrands (both the finite elements and splined equilibrium quantities are at most cubic).

7.10 Ampere's law

The integral from of Ampere's law is

$$\lambda \int dV \hat{\mathbf{a}} \cdot \mathbf{a} = \int dV \hat{\mathbf{a}} \cdot (\mathbf{v} \times \mathbf{B}) - \int dV \eta(s) \hat{\mathbf{a}} \cdot (\nabla \times \nabla \times \mathbf{a}). \quad (98)$$

For explicit calculations, all the operators are be given an explicit representation in co/contravariant formalism,

$$\begin{aligned} & \lambda \int dr d\theta d\zeta \sqrt{g} \hat{\mathbf{a}}^i \mathbf{a}_j \quad (99) \\ & = \int dr d\theta d\zeta \eta(s) \left(\epsilon^{lok} \partial_o \frac{g_{ki}}{\sqrt{g}} \hat{\mathbf{a}}^i \right) \frac{g_{lm}}{\sqrt{g}} (\epsilon^{mnj} \partial_n \mathbf{a}_j) + \hat{\mathbf{a}}^i \epsilon_{ijl} \mathbf{v}^j B^l, \quad (100) \end{aligned}$$

where there is an implied sum over each the sub- and superscripts, except i , so we have three equations, one corresponding to each component of the vector equation. We then replace the trial and weighting vectors with their discretised component representation. The combined finite element and double Fourier sum

which represents our vector \mathbf{a} is

$$\mathbf{a} = \sum_{m,n,l} (h_l(s)a_{1:mnt}, c_l(s)a_{2:mnt}, c_l(s)a_{3:mnt}) e^{im\theta - in\zeta} \quad (101)$$

for the trial vector and

$$\hat{\mathbf{a}} = \sum_{\hat{m}, \hat{n}, \hat{l}} (h_{\hat{l}}(s)\hat{a}^{1:\hat{m}\hat{n}\hat{l}}, c_{\hat{l}}(s)\hat{a}^{2:\hat{m}\hat{n}\hat{l}}, c_{\hat{l}}(s)\hat{a}^{3:\hat{m}\hat{n}\hat{l}}) e^{-i\hat{m}\theta + i\hat{n}\zeta} \quad (102)$$

for the weighting functions.

The complete sets of coupling functions are contained in appendix A. As an example of the calculation we isolate the term coupling $v_{1:mnt}$ and $\hat{a}^{2:\hat{m}\hat{n}\hat{l}}$:

$$v_{1:mnt}\hat{a}^{2:\hat{m}\hat{n}\hat{l}} \int dsd\theta d\zeta c_{\hat{l}}(r) \frac{\Psi_{tor}(s)}{2\pi} c_l(r) e^{i(m-\hat{m})\theta - i(n-\hat{n})\zeta} \quad (103)$$

The integral over θ and ζ is a double Fourier transform, and in the actual implementation, any surface functions which appear factor out, so that in general we need only take Fourier transform of various products of the metric tensor and the Jacobian.

7.11 The Equation of motion

The equation of motion reads:

$$\rho^* \frac{\partial}{\partial t}(\mathbf{v}) = (\nabla \times \nabla \times \mathbf{a}) \times \mathbf{B} + \mathbf{J} \times (\nabla \times \mathbf{a}) - \nabla p, \quad (104)$$

and the integral form is then

$$\lambda \int dV \rho^* \hat{\mathbf{v}} \cdot \mathbf{v} = \int dV \hat{\mathbf{v}} \cdot (\nabla \times \nabla \times \mathbf{a}) \times \mathbf{B} + \hat{\mathbf{v}} \cdot \mathbf{J} \times (\nabla \times \mathbf{a}) - \hat{\mathbf{v}} \cdot \nabla p \quad (105)$$

As before, we replace the operators by their explicit forms in curvilinear coordinates; this yields

$$\lambda \int dsd\theta d\zeta \rho^* \sqrt{g} \hat{\mathbf{v}}^i g_{ij} \mathbf{v}^j \quad (106)$$

$$= \int dsd\theta d\zeta (\hat{v}^j) \frac{1}{\sqrt{g}} \epsilon_{jkl} ([\epsilon^{kmn} \partial_m \mathbf{g}_{no} \epsilon^{opi} \partial_p \mathbf{a}_i] [\mathbf{B}^l]) \quad (107)$$

$$+ \sqrt{g} \hat{\mathbf{v}}^i \epsilon_{iok} \mathbf{J}^o \epsilon^{klj} (\partial_l \mathbf{a}_j) \quad (108)$$

$$+ (\delta_i J \hat{\mathbf{v}}^i) p \quad (109)$$

Integration by parts can be used to reduce derivatives on the perturbing quan-

tities to first order.

7.12 Equation of state

We have the equation of state:

$$\frac{\partial p}{\partial t} = -\mathbf{v} \cdot \nabla P - \gamma P \nabla \cdot \mathbf{v}, \quad (110)$$

with the integral form:

$$\lambda \int dV \hat{p} p = \int dV \hat{p} \mathbf{v} \cdot \nabla P - \hat{p} \gamma P \nabla \cdot \mathbf{v} \quad (111)$$

leading to a simple expanded form:

$$\begin{aligned} & \lambda \int dV d\theta d\zeta J \hat{p} p \\ & = - \int dV d\theta d\zeta \left[\hat{p} \frac{\partial P}{\partial s} \mathbf{v}^1 + \gamma P \left(\hat{p} \frac{\partial \mathbf{v}^1}{\partial s} + \hat{p} \frac{\partial \mathbf{v}^2}{\partial \theta} + \hat{p} \frac{\partial \mathbf{v}^3}{\partial \zeta} \right) \right] \end{aligned} \quad (112)$$

7.13 Code generation

To deal with the large number of terms which arise in the matrix elements of \mathbf{A} and \mathbf{B} with a lower likelihood of error, the code generation procedure is automated using Mathematica. This symbolic calculation requires a certain care in handling the co- and contra-variant components of quantities. We use capitalisation of the first letter of each symbol to denote this: contravariant vectors and operators with contravariant results are in capitals, and covariant quantities are lower case. These definitions are inserted into a Mathematica notebook together with the definitions of the equilibrium functions J , B and P and the metric tensor, the vector components of the perturbing quantities \mathbf{b} and \mathbf{v} and the linearised resistive MHD equations; we can then set up the Mathematica system to output (Fortran 77) code for each of the coupling coefficients. The code is converted to (Fortran 95) free source form by an external routine. Details of this procedure and the Mathematica code are in appendix A.

7.14 Solution of the eigenvalue equation

We can determine whether a system with a finite number of degrees of freedom is stable by considering the eigenvalues of the time evolution operator: if all the eigenfrequencies are in the lower half of the complex plane, the system is linearly stable. The discretised linear equations are a time evolution equation

```

choose a starting guess for the eigenvalue  $\lambda_0$ , and for the eigenvector  $\mathbf{x}_0$ 
 $i = 0$ 
for  $j = 0$  to  $n$  do
  Find the LU decomposition  $\mathbf{LU} = (\mathbf{B} - \lambda_i \mathbf{A})$ , where  $\mathbf{L}$  is lower triangular,
  and  $\mathbf{U}$  is upper triangular
  for  $k = 0$  to  $n$  do
     $i = i + 1$ 
    Solve  $\mathbf{x}_i = (\mathbf{LU})^{-1} \mathbf{A} \mathbf{x}_{i-1}$ 
    Find  $\mathbf{x}_A = \mathbf{A} \mathbf{x}_i$ , and  $\mathbf{x}_B = \mathbf{B} \mathbf{x}_i$ 
    The new guess for the eigenvalue is  $\lambda_i = (\mathbf{x}, \mathbf{x}_B) / (\mathbf{x}, \mathbf{x}_A)$ 
    If we have  $|\lambda_i - \lambda_{i-1}| < \epsilon$  we have convergence, so exit
    Normalise  $\mathbf{x}_i$  if necessary
  end for
end for

```

Figure 10: The shift and invert algorithm for solving the eigenproblem $(\lambda_0 \mathbf{A} - \mathbf{B})\mathbf{x} = 0$.

$d/dt \mathbf{A} \mathbf{x} = \mathbf{B} \mathbf{x}$, and we consider solutions \mathbf{x} to this equation whose time dependence can be expressed as $\exp(\lambda t)$, and whose complex growth rates λ satisfy $\lambda \mathbf{A} \mathbf{x} = \mathbf{B} \mathbf{x}$. The matrix \mathbf{B} is non-Hermitian, and the growth rates are, in general, fully complex. In order to solve the generalised eigenproblem by standard techniques, we convert the generalised eigenproblem to a standard one, and look for eigenvalues λ around a start eigenvalue λ_0 , $\sigma \mathbf{x} = (\mathbf{B} - \lambda_0 \mathbf{A})^{-1} \mathbf{A} \mathbf{x}$ with $\lambda = \lambda_0 + 1/\sigma$. We have implemented two iterative methods for solving these eigenvalue problems; invert and shift and the Jacobi–Davidson method. The invert and shift algorithm described in figure 10 is the simplest of the two. This iterative procedure has reliable convergence because the eigenvalues of interest, near the guess λ_0 , are the largest eigenvalues of $(\mathbf{B} - \lambda_0 \mathbf{A})^{-1} \mathbf{A}$. In the case where we have a full basis of (right) eigenvectors \mathbf{u}_k with eigenvalues σ_k , we can express our eigenvector guess as

$$\mathbf{x}_0 = \sum_k c_k \mathbf{u}_k \quad (113)$$

and after step i we have

$$\mathbf{x}_i = \sum_k (\sigma_k)^i c_k \mathbf{u}_k \quad (114)$$

so that the largest eigenvalue will eventually dominate the sum as long as our initial guess has a non-zero component in the direction of the corresponding eigenvector: a random initial guess almost always meets this requirement.

The Jacobi–Davidson method is a more sophisticated subspace procedure

which can find multiple eigenvalues at the same time. It does not need an exact matrix inverse, and there is a variant which solves the generalised non-Hermitian eigenvalue problem without first converting it to a standard eigenvalue problem: this means that the method does not require a computationally costly LU decomposition step. However, we implemented the simplest version of the procedure, in which we first convert to a standard eigenproblem. The details of this technique can be found in [48] and [49].

For problems with strong toroidal and poloidal coupling, many modes need to be considered, and the matrices can become very large. Because we have implemented only in-core solvers, this limits the problem size. For example, with 24 modes included, and 60 radial grid points, we need approximately 2.7 GB to store the matrix coefficients. This is close to the limit of feasible memory requirements for a single CPU in the Australian Partnership of Advanced Computing (APAC) supercomputer with AlphaServer SC ES45 nodes. Setting up the matrices and calculating a single eigenvector for such a case consumes of the order of 30 CPU minutes computer time on a single CPU of this supercomputer (as of 2004). On typical multi-CPU supercomputers, however, it is possible to access considerably larger amounts of memory. We therefore implemented a parallelised version of Spector3D, using the message passing protocol MPI, and the SCALAPACK and PBLAS libraries, which implement parallelised versions of the LAPACK and BLAS linear algebra libraries respectively. The banded inverse solver implemented in SCALAPACK uses a divide and conquer strategy, which introduces a restriction on the number of CPUs that can be used for a given relative matrix bandwidth for our code. For a radial grid resolution n , we can utilise up to $n/4$ CPUs, although there are diminishing returns above about $n/16$ CPUs which sets a practical limit. The Fourier space resolution is then limited by the single CPU memory size.

7.15 1D test cases

To check the correctness and accuracy of the code, we first examine the incompressible constant current model of [32], as detailed in section 6. The spectrum of this test case contains a variety of unstable and stable resistively modified global Alfvén modes, as well as a possibly large number of unphysical modes (again, see section 6). We select a few eigenvalues near the marginal stability point for accuracy and convergence tests.

For the purpose of comparison, we consider the example parameters used in figure 1 of that paper, with $m = 1$, $\kappa = 1.4$, $nq = 1.2$ and $S = 2 \times 10^4$. The relevant incompressible limit is given by $\gamma \rightarrow \infty$; in the numerics we can simply set this to some very large number, $\gamma > 10^6$. In this case we tabulate

the convergence of the frequencies $\omega = i\lambda$ of the three unstable modes, along with the frequencies of two slightly damped oscillatory modes:

Analytic	$i = 10$	$i = 30$	$i = 100$	$i = 300$
$0.316973i$	$0.312480i$	$0.316450i$	$0.316932i$	$0.316975i$
$0.199164i$	$0.190809i$	$0.198089i$	$0.199077i$	$0.199165i$
$0.114088i$	$0.099565i$	$0.112084i$	$0.113919i$	$0.114098i$
0.034428	0.064044	0.040721	0.035142	0.034533
$-0.0051255i$	$-0.005661i$	$-0.0051920i$	$-0.005116i$	$-0.005111i$
0.103563	0.115853	0.105873	0.103869	0.103655
$-0.0076193i$	$-0.008516i$	$-0.0770312i$	$-0.007577i$	$-0.007571i$

It is also interesting to compare the rest of the spectrum with the analytic result. Figure 11 shows that even for radial 200 grid points a significant fraction of the numerical eigenvalues have not converged to the neighbourhood of an actual eigenvalue. These are generally modes with very high radial wavenumber, and are correspondingly strongly damped, so they are less interesting from the physical perspective than the modes near the real axis. However, the cause of the poor convergence is still relevant from the point of view of code validation. It has been shown [19] [50] that the positions of such eigenvalues are extremely sensitive to small numerical errors; this is related to the strong non-normality of the MHD spectrum.

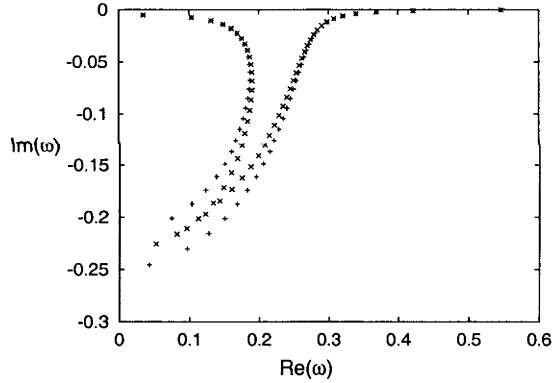


Figure 11: The frequencies $\omega = i\lambda$ of the stable modes of the 1D incompressible spectrum plotted in the complex plane. The spectrum from the numerics (\times) is shown together with the analytic result ($+$). Modes along the stable imaginary axis have been omitted.

We then considered the cylindrical test case described in section 4.2 of [31], in which a radial variation in toroidal current can lead to internal tearing modes. The peaked current profile is described by

$$\mathbf{j}(r) = \hat{\zeta} j_0 (1 - r^2/a^2)^{\nu}, \quad (115)$$

the toroidal magnetic field is set to $\mathbf{B} \cdot \hat{\zeta} = 1$, and the density profile is $\rho = 1$. For these profiles the ratio of safety factor at the plasma surface $r = a$ to the safety factor on axis is $q(a)/q(0) = v + 1$. The instabilities resolved in [31] are the $m = 2$ internal tearing mode and external kink, and we reproduce a tearing mode for the purpose of code verification and as a simple demonstration of tearing mode physics.

As with the constant current model, we have the toroidal closure modelled by a simple periodicity in the ζ direction, and we consider modes with toroidal mode number $n = 1$. We have the $m = 2$ tearing mode unstable for $2.20 \leq q(a) \leq 4.0$, as shown in figure 12, which is visually identical to that in [31]. On an enlarged scale (see figure 13) we can see that as $q(a)$ approaches the tearing mode marginal stability value of 2.2 from below there is still an instability with a significant growth rate, as we would expect considering that the resistive interchange stability condition is violated.

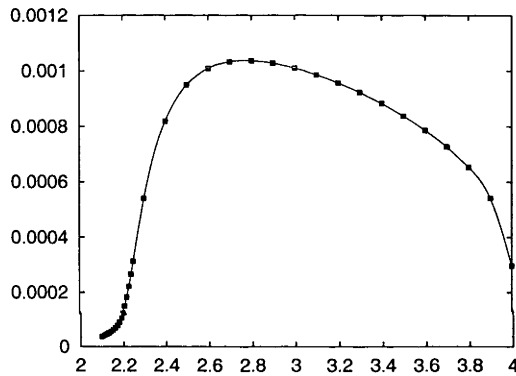


Figure 12: The fixed boundary growth rate λ of the most unstable mode of a cylindrical equilibrium versus $q(a)$, the safety factor at the plasma surface. The tokamak-like toroidal current profile is described in equation (115).

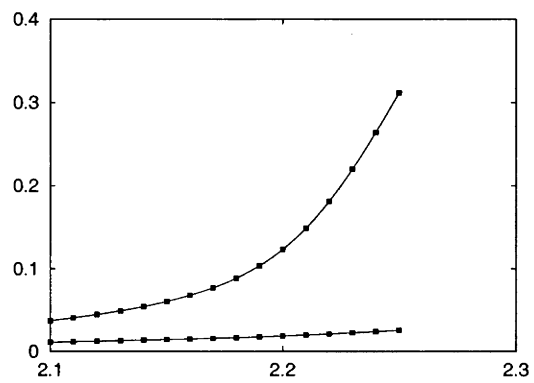


Figure 13: The scaled growth rate $\lambda \times 10^3$ of the two most unstable modes of a cylindrical equilibrium near the tearing mode marginal stability boundary, versus $q(a)$, the safety factor at the plasma surface. The tokamak-like toroidal current profile is described in equation (115).

7.16 2D test cases: Solov'ev equilibria

There exist a class of exact solutions to the MHD equilibrium equations known as *Solov'ev equilibria* [51]. In these equilibria the derivatives with respect to ϕ (poloidal flux) of the pressure and the integrated poloidal current are constant across the radius. The analytic solutions cover a range of aspect ratios and elongations and also allow a choice in β_p , the proportion of confinement generated by toroidal current. Some of these axisymmetric equilibria are similar to tokamak configurations of interest, making them a natural target for theoretical studies of tokamaks, and for the benchmarking of codes; several papers on two dimensional resistive and ideal stability codes have published the tables of growth rates for various Solov'ev configurations, and we present our results for these cases. The most well tested fixed boundary case is an equilibrium with no poloidal currents ($\beta_p = 1$), an ellipticity near the magnetic axis of 2, and an aspect ratio of 3. The remaining parameter is the safety factor (inverse rotational transform) on axis, which takes on values between $q(0) = 0.2 - 1.3$ in [52], but in particular the values $q(0) = 0.3, 0.7$ have tabulated results [3] for the most unstable eigenvalue in the $n = 2$ mode family. This is an internal kink mode, with the dominant m value dependent on the safety factor. The eigenvalues in these tables are normalised to the poloidal Alfvén time at the plasma edge, and thus are related to the (un-normalised) eigenvalue from Spector3D by

$$\gamma = \lambda \frac{\rho R q(1)}{B(0)} \quad (116)$$

where R is the major radius of the device, $q(1)$ is the safety factor at the plasma boundary, and $B(0)$ is the magnetic field strength on axis.

In order to produce the input required by Spector3D, we describe the analytical Solov'ev equilibrium in VMEC output format, then use the mapper code to recalculate this equilibrium description in Boozer coordinates. The radial parameter s is chosen equal to the normalised poloidal flux ϕ to allow accurate resolution of the equilibrium near the magnetic axis, where the standard VMEC description with $s = \psi$, the normalised toroidal flux, is rather sparse. It is also important to ensure sufficient poloidal resolution, particularly in the reconstruction of the equilibrium in Boozer coordinates. We use 30 poloidal modes to solve the magnetic differential equation whose solution gives the mapping from our input coordinate system into Boozer coordinates. The mapped equilibrium which is input into SPECTOR3D is described on 97 radial and 128 poloidal grid points.

For comparison we display eigenvalues resolved by other MHD codes against those of SPECTOR3D in table 1. Our eigenvalues are clearly not in as close

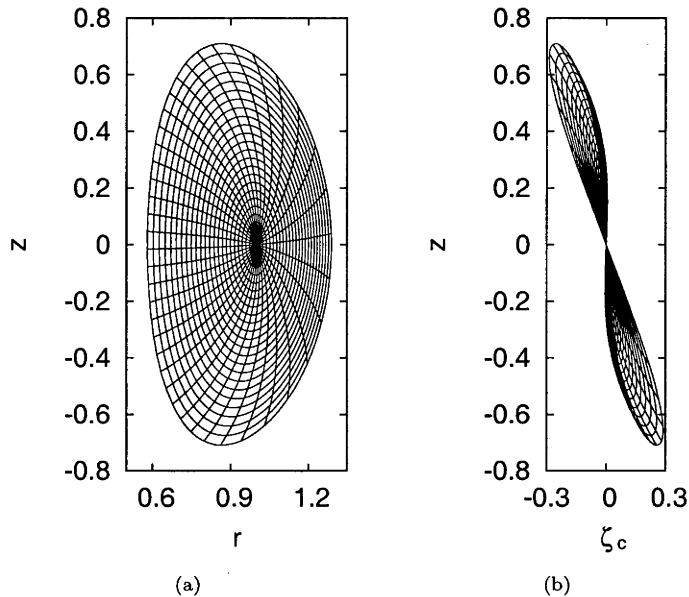


Figure 14: A Solov'ev equilibria in Boozer coordinates, with $R/a = 3$, an ellipticity of 2, and $q(0) = 0.7$. Lines of constant poloidal flux ϕ and Boozer angle θ_f are shown on a $\zeta_f = \text{constant}$ surface. The rightmost figure shows that the $\zeta_f = \text{constant}$ surface is not a surface of constant cylindrical angle ζ_c , despite this being an axisymmetric equilibrium.

agreement as those of the other codes, departing by approximately 7% in the second case. Although some effort has been expended to determine the source of the discrepancy, it does not appear to lie with limited numerical resolution in either the equilibrium or stability codes.

The next item of interest is the convergence behaviour. Figure 15 shows that the convergence with respect to the radial grid-number is quartic. This is in line with the high degree of convergence expected when approximating smooth eigenmodes with this relatively high order finite element scheme. Figure 16 shows that the convergence with respect to the number of poloidal Fourier

$q(0)$	SPECTOR3D	CASTOR	ERATO	MARS	TERPSICHORE
0.3	1.295	1.255	1.26	1.26	1.25
0.7	0.262	0.284	0.284	0.284	0.284

Table 1: Comparison of the eigenvalue λ of the most unstable $n = 2$ ideal instability of fixed boundary Solov'ev Equilibria with $\epsilon^{-1} = 3$, $n = 2$ and $E = 2$ as calculated by various MHD spectral codes.

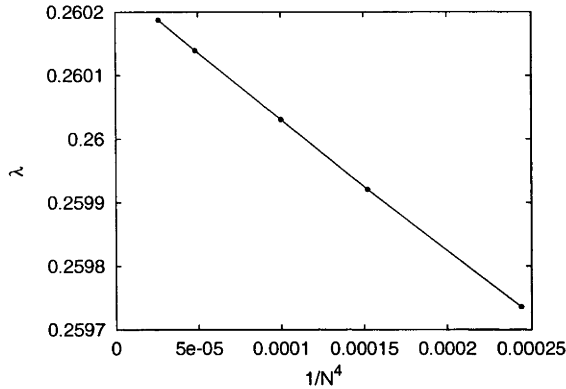


Figure 15: The convergence of the growth rate λ of the most unstable mode with respect to the number, N , of radial grid points included. This is an $n = 2$ instability in a fixed boundary Solov'ev equilibrium with $\epsilon^{-1} = 3$ and $E = 2$. The convergence is quartic, so that $\delta\omega \propto 1/N^4$.

components is exponential, but as other authors have pointed out [52] [3], a relatively large number of Fourier harmonics must be resolved in order to obtain a converged result: for the example here, with $q_0 = 0.7$, we require 16 Fourier components to obtain a relative error in eigenvalue of one part in 10^{-4} .

7.17 Resistive ballooning modes in near axisymmetric devices

For tokamak configurations without any poloidal currents, the 1/1 kink mode alone is enough to limit the maximum β which can be achieved. For configurations with poloidal currents, the pressure limiting ideal MHD instabilities are often not the simple interchange modes, as the Mercier criterion usually indicates stability, but ballooning modes. [53] [54]. These modes become unstable at high β when the large Shafranov shift generated by the strong plasma pressure gradients produces unfavourable curvature on the outboard side of the plasma. However, even at low β where these ideal modes are stable, their resistive versions, the resistive ballooning modes, can become unstable. For an axisymmetric device the most unstable resistive ballooning modes will also be localised on the outboard side of the plasma. We consider the transition between such an axisymmetric equilibrium, and a strongly toroidally shaped equilibrium, where toroidal localisation is expected. We are not attempting here to comprehensively explore the scaling behaviour with respect to β , S , and toroidal mode number: we simply wish to show the qualitative evolution of such modes as toroidal coupling is introduced, demonstrating the mode localisation.

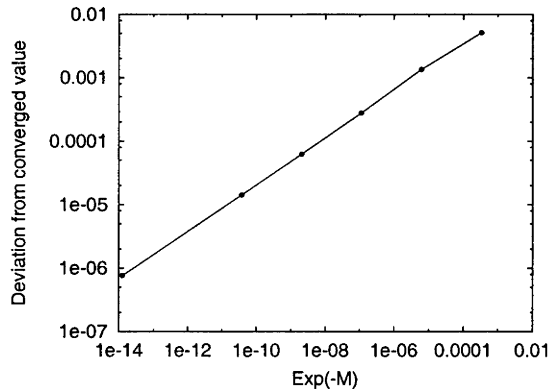


Figure 16: The convergence of the most unstable eigenvalue with respect to the number, M , of poloidal Fourier harmonics included. This is an $n = 2$ instability in a fixed boundary Solov'ev equilibrium with $\epsilon^{-1} = 3$ and $E = 2$. The deviation of the eigenvalues from the converged value, for which we use the $M = 40$ eigenvalue, is plotted. An exponential dependence is suggested by the constant slope of the interpolating line.

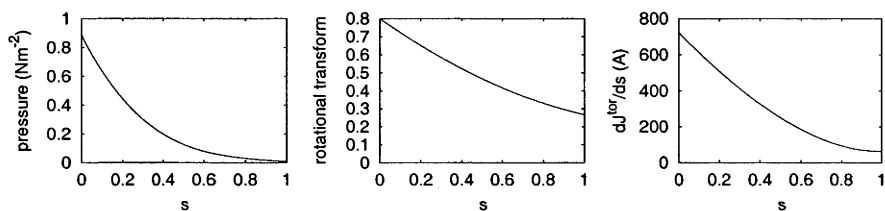


Figure 17: Surface quantities for the tokamak-like equilibrium of section 7.17.

The equilibria studied have aspect ratio $R/a = 4$, and are restrained by a conductive wall which is circular in cross section. The basis configuration has a safety factor profile which increases by a factor of three from the axis to the plasma edge ($q_a/q_0 = 3$), and has no poloidal currents; the corresponding pressure and toroidal current profiles are strongly peaked, with $J \simeq (1 - \Psi)^2$. We introduce three dimensionality into these configurations by imposing sausage-like deformations, with a toroidal mode number of 5, to the outermost flux surface (see figure 7.17); for moderate deformations this might represent the effect of the finite number of poloidal field coils, and for extreme values, the configuration is similar to a set of linked mirrors. The stronger field in the waist regions can provide an MHD anchor, and localise the mode toroidally. On the other hand, in the low field regions the magnetic field lines have more unfavourable curvature. Therefore, as we introduce the deformation, we ex-

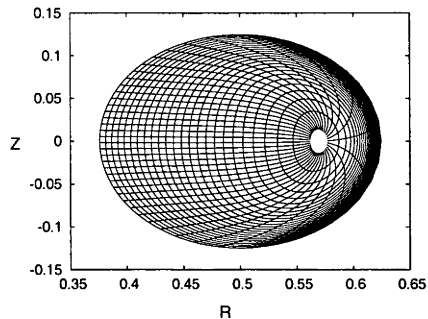


Figure 18: A cross-section of the flux surfaces of the tokamak-like equilibrium of section 7.17. Lines of constant Boozer angle θ are also plotted.

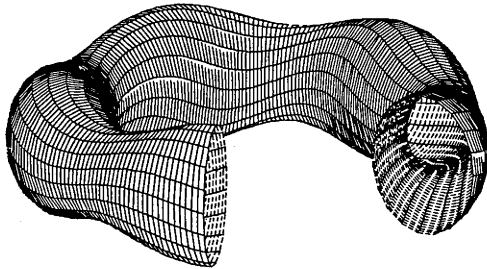


Figure 19: The outermost flux surface for a tokamak-like equilibrium with a strong toroidal field modulation.

pect the strongest resistive MHD instabilities to localise around a point on the outside of the torus in the low field region.

For these configurations, we found the most unstable mode with dominant toroidal mode number $n = 1$ for a range of values of the resistivity. The mode family which is toroidally coupled to $n = 1$ includes mode pairs with toroidal indices $n = 1 + 5k$ for integer k . The set of Fourier harmonics chosen for the stability analysis have toroidal index $n = -9, -4, 1, 6$ and 11 . We would expect to find large n instabilities which have higher growth rates than the $n = 1$ modes, so for the purposes of this study, we do not include any Fourier harmonics resonant with the field apart from those at $n = 1$. This allows us to examine the change in the dominantly $n = 1$ mode as we introduce toroidal shaping. The coupling between resonant $n = 1$ harmonics and resonant terms with $n \neq 1$, which have $\delta m > 5$ and $\delta n > 5$, is weak, as the equilibrium has no strong shaping with this mode number (unlike, perhaps, a helical equilibrium); the terms we do include are those with small jumps in mode number from the resonant $n = 1$ modes. For higher n instabilities, coupling between resonant modes with

different n would be more critical, and it would no longer be reasonable to exclude such Fourier components. Mode with a wide range of n and m would then need to be included, and this could be numerically infeasible.

We include compressibility in the study by setting $\gamma = 5/3$; this has a stabilising effect for these resistive modes via a coupling to the sound spectrum. Analytical ballooning theory indicates that there may be unstable modes with fully complex frequency in the compressible case. For the axisymmetric base configuration, the instability is strongest at $S \simeq 50$, well below the values of S expected to be relevant for magnetic confinement devices. Between this value and $S \simeq 3000$ the most unstable mode is ballooning-like with large amplitudes for the resonant and near resonant Fourier components, and no strong radial localisation of any of the Fourier components. There is clear poloidal localisation in the region of bad curvature in this regime, and the mode magnitude is largest at mid-radius, where there are strong pressure gradients. At $S \simeq 3000$ the most unstable mode begins to localise near the plasma edge, which is where it stays between this value of S and $S \simeq 10^5$, the highest value of S resolved in this case. The asymptotic scaling of the growth rate is linear with the resistivity, so that the growth rates are very small for realistic S in this configuration. However, it is unclear that the modes found localised near the plasma edge are of physical significance: the equilibrium may not be well resolved near the conducting boundary. Nevertheless, the linear bound on the growth rate still holds, indicating that for small resistivity the resistive modes should always have very small growth rates, and are experimentally unimportant. Linear scaling is found analytically and via ballooning theory for such low- n modes in [39].

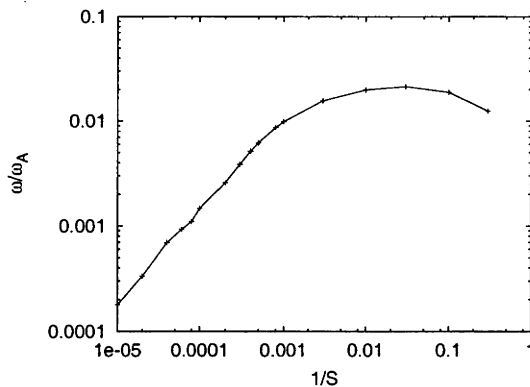


Figure 20: The growth rate, normalised to the Alfvén time, of resistive modes in an axisymmetric configuration as a function of the Lundquist number S .

For the non-axisymmetric cases, we resolve most of the Fourier components

which have toroidal mode numbers $n \in -9, -4, 1, 6, 11$ and poloidal mode numbers $m \in -2, -1, \dots, 6, 7$. The radial displacements associated with each Fourier component of the most unstable mode are plotted in figure 22. Keeping the value of S fixed at 10^3 , and introducing non-axisymmetric shaping into the equilibrium leads to a coupling into the toroidal sidebands which is roughly proportional to the degree of the shaping. For this q profile, and the particular choice of Fourier components, only the modes with $n = 1$ are resonant. However, the toroidal sideband coupling is sufficient for $\delta r/r_0 = 0.2$ to produce strong destructive interference in the waist region, as can be seen in figure 23. The growth rate (figure 21) increases somewhat with the introduction of non-axisymmetry, as the mode toroidally localises in region which have worse than average curvature.

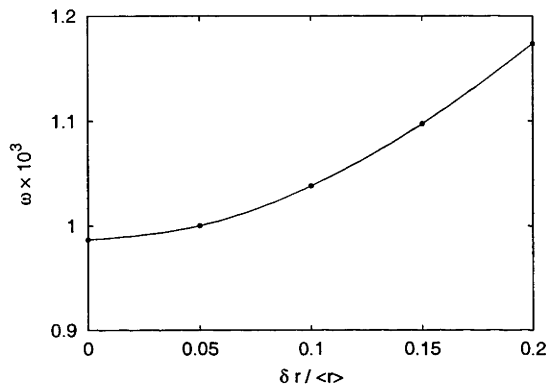


Figure 21: The maximum growth rate of an $m = 1$ unstable resistive ballooning-like mode with $S = 1000$ as a function of the toroidal ripple $\delta r / \langle r \rangle$.

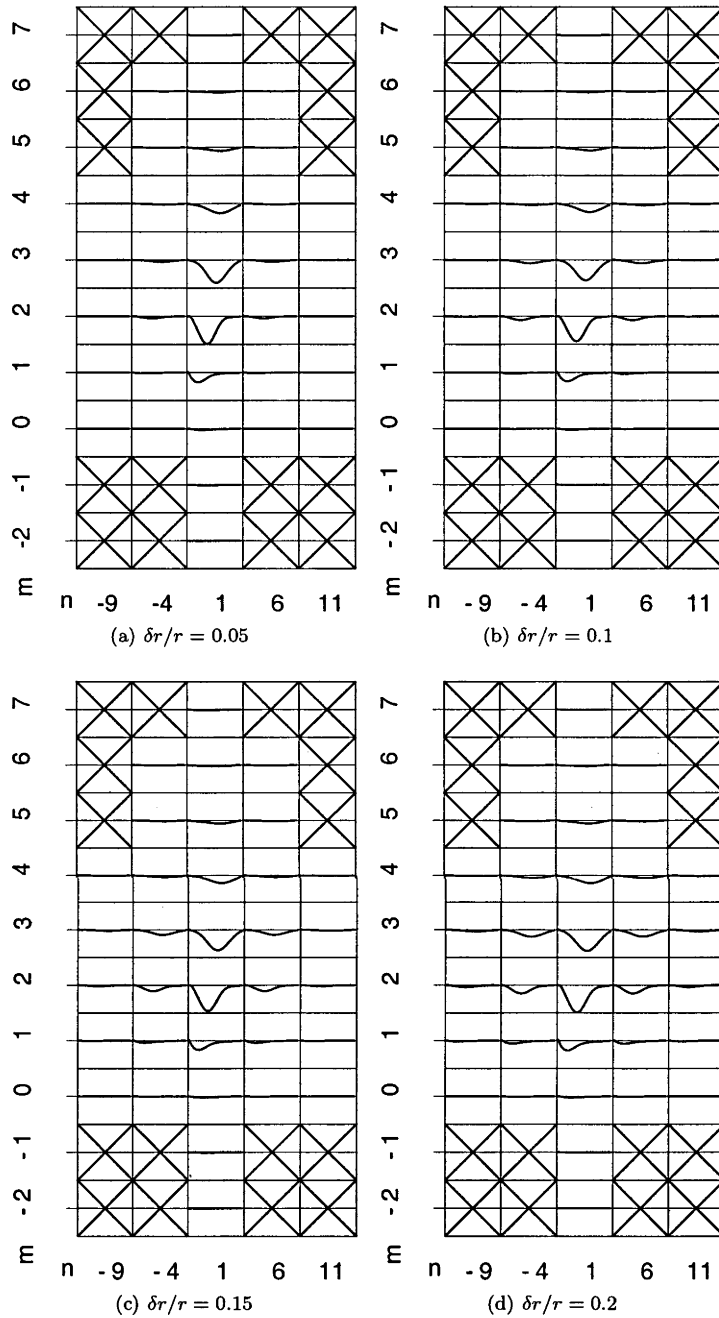


Figure 22: The sets of radial displacements for each Fourier harmonic (m, n) of the most unstable eigenmode resolved by SPECTOR3D for four different values of the shaping factor $\delta r/r_0$. Each grid square corresponds to one Fourier component, with rows all having the same poloidal mode number, and columns sharing toroidal mode number. Some grid squares are marked with crosses: these correspond to mode pairs which were excluded from the calculation. In the other grid squares, the radial plasma displacement is plotted as a function of minor radius, with the magnetic axis as the leftmost point, and the conductive wall as the rightmost. For this configuration we have $S = 1000$, $q_0 = 1.25$, $q_a = 3.75$ and $\beta = 0.3\%$.

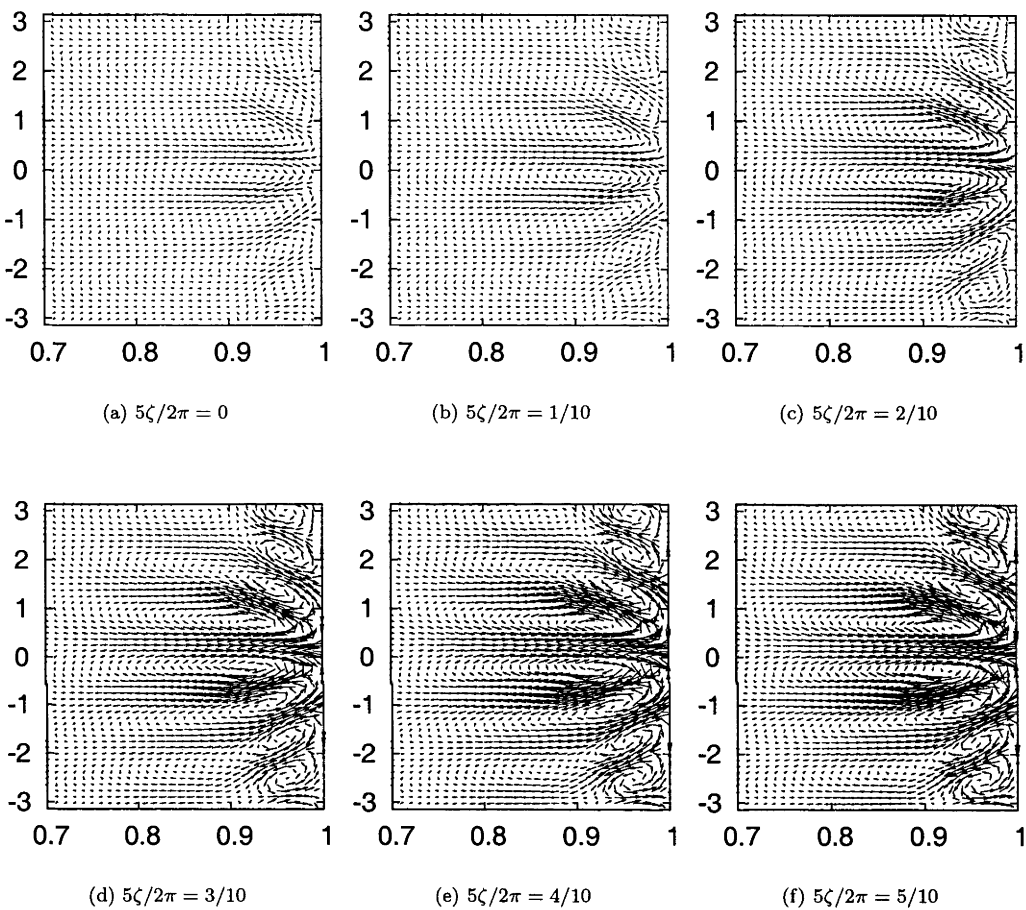


Figure 23: The radial and poloidal plasma displacements corresponding to a resistive ballooning mode in a tokamak-like configuration with strong toroidal ripple, $\delta r/r_0 = 0.2$. To show the toroidal variation in the mode strength, we plot the displacements on six plasma cross sections evenly spaced on a half field period (these are surfaces of constant Boozer angle ζ). The vertical axis is the poloidal Boozer angle θ and the horizontal axis is the normalised toroidal flux ψ . For this configuration $q_0 = 1.25$, $q_a = 3.75$ and $\beta = 0.3\%$. We set $S = 10000$.

7.18 Heliotron E

In [55], a technique based on averaging over both the toroidal and poloidal directions was used to analyse the ideal and resistive stability of a wide range of force-free large aspect ratio heliotron configurations. These configurations have varying vacuum rotational transform and toroidal current profiles, but can be constructed by varying a standard Heliotron E configuration. Most of the parameter space is occupied by truly hybrid devices in which a large proportion of the rotational transform is generated by the toroidal currents. These series of equilibria were later investigated with the semi-3D ideal MHD code STEP in [56]. The ideal MHD stability of these configurations with respect to kink modes was found to closely agree with the results of analysis in [55].

The vacuum rotational transform profiles considered are of the form $\iota = \iota_0^\delta(0.286 + 0.714\psi)$, where ψ is the normalised toroidal flux, and ι_0 takes some value in the range $[0, 2]$. We can closely reproduce these profiles by choosing an appropriate Heliotron configuration. The basis configuration is a standard Heliotron E configuration, with 17 field periods, and an almost planar magnetic axis. The flux surface cross sections are approximately elliptical, with the orientation of the ellipse rotating through an angle of π per field period. We modify this basis configuration to examine the parameter space of interest. The transform on axis, ι_0^δ , is a function of the flux surface shaping, and can be controlled by changing the magnitude of the helical deformation coefficients in the VMEC input. The most important shaping term is the $m = 1/n = 1$ component of the VMEC flux surface series, for which we impose $R = \epsilon$ and $Z = -1.05\epsilon$. The rotational transform at the edge is approximately proportional to ϵ , and the transform profile generated by this shaping closely matches the required profile. We then introduce a strongly peaked toroidal plasma current into these configurations, with $J = J_0(1 - \psi)^4$, with the pressure profile still constrained to be zero. Poloidal currents are then produced to provide force balance. We label the additional rotational transform produced at the edge of the plasma by the introduction of currents ι_0^σ , so that the total transform at the edge is $\iota_0 = \iota_0^\delta + \iota_0^\sigma$. The strongly peaked current profile leads to much larger transform increase near the center of the plasma than at the edge.

The most unstable ideal MHD modes found are the $m = 1/n = 1$ internal kink modes, which are associated with the rational surface where $\iota = 1$. In cases with small vacuum rotational transform $m = 2/n = 1$ and $m = 3/n = 1$ resistive tearing modes are predicted analytically. We consider these instabilities by resolving the $n = 1$ mode family (coupling to $n = -16, +1, +18, \dots$). Preliminary runs indicated that there was not much toroidal or poloidal coupling, and for the configurations chosen the non-dominant components of the mode were at most $\simeq 10\%$ as large as the dominant component. The toroidal coupling was

negligible for the cases with low vacuum transform, where the tearing modes are seen, but was approximately as important as the poloidal coupling for some of the cases there the $m/n = 1/1$ kink mode is present, as indicated by figure 24. Being able to resolve the toroidal and poloidal coupling in this case provides an important check for physically motivated arguments that suggest that such coupling should not have a large effect. For the parameter survey we only considered the $n = 1$ Fourier components of the perturbation, as the tearing modes were of most interest for our study. We chose poloidal mode numbers $m \in [-1, 8]$, and this was sufficient to resolve the limited poloidal coupling of the equilibrium. For zero resistivity we find only an $m = 1/n = 1$ internal kink mode. However for finite resistivity $m = 2/n = 1$ instabilities are seen in some regions of the parameter space as indicated by figure 27.

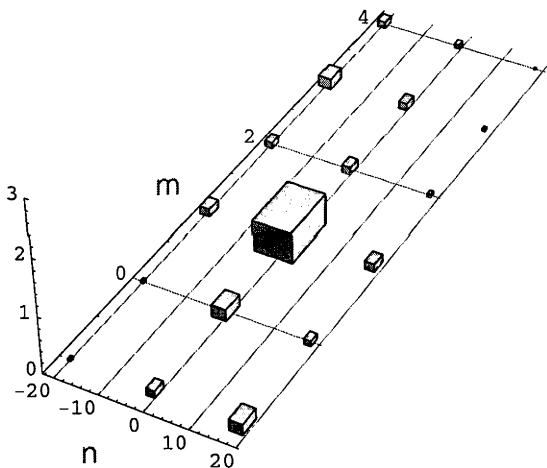


Figure 24: The strength of various Fourier components of the most unstable ideal MHD mode in a current carrying heliotron configuration as a function of poloidal and toroidal wavenumbers m and n . The vacuum transform ι_0^d is 0.5 and the current induced transform ι_0^c is 0.3. The volume of each box in the figure is proportional to the maximal radial displacement found for each Fourier component.

The instabilities of these configurations can be resolved accurately by SPECTOR3D even with a small number of Fourier modes, but a reasonable amount of radial resolution is required in cases with low resistivity, and we use 400 radial grid points for our equilibrium scans. In the resistive case, we perform a param-

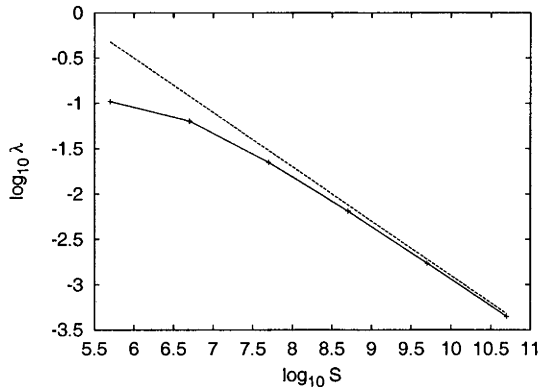


Figure 25: The growth rate of an $m = 2/n = 1$ tearing mode in a zero β current carrying heliotron as a function of the Lundquist number S . The straight line shows the predicted asymptotic dependence, $\omega \propto S^{-3/5}$. The vacuum rotational transform at the plasma edge, ι_0^δ , is 0.15, and the additional rotational transform at the plasma edge produced by toroidal currents, ι_0^σ , is 0.14.

eter scan in S for the configuration most unstable to tearing modes: the growth rates are plotted in figure 25, and a representative set of eigenfunctions is shown in figure 28. We are well into the asymptotic scaling regime for $S = 10^{-7}$, which is the value we choose for the scan over the rest of configuration space. The boundaries of the region unstable to internal $m = 1/n = 1$ modes agrees well with that found in previous literature [56] [55]. These modes become unstable when the resonant rational surface with $\iota = 1$ lies in a region of strong current gradient. As the toroidal current is increased, the $\iota = 1$ rational surface moves outwards in minor radius. A free boundary analysis would show that the plasma becomes unstable to an external kink mode when this surface moves beyond the plasma edge, but we have imposed a conductive wall at the plasma boundary and our model becomes stable. Resistive tearing modes are found only in the tokamak-like configurations where the vacuum rotational transform at the edge of the plasma, ι_0^δ , is 0.15.

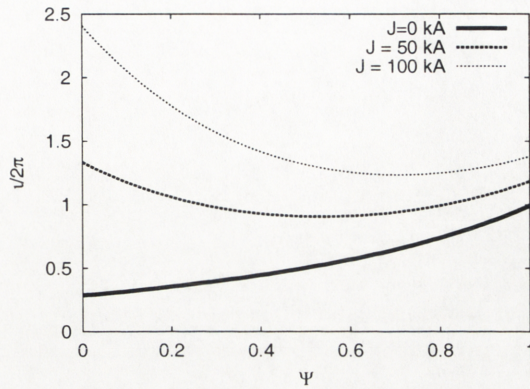


Figure 26: Rotational transform profiles for a current carrying heliotron with varying values of the total toroidal current J . The outermost flux surface shape is held constant.

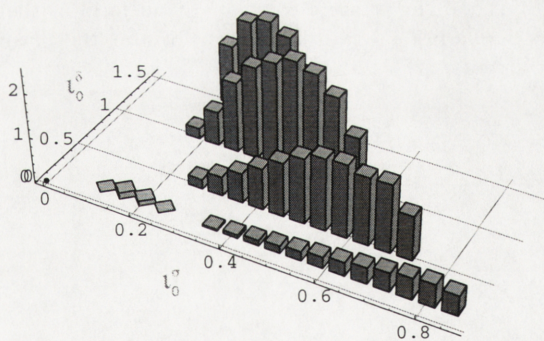


Figure 27: Kink mode ($m = 1, n = 1$, bars) and resistive tearing mode ($m = 2, n = 1$, diamond prisms), showing relative growth rates for configurations with varying vacuum rotational transforms, l_0^δ , and plasma current generated transform l_0^σ .

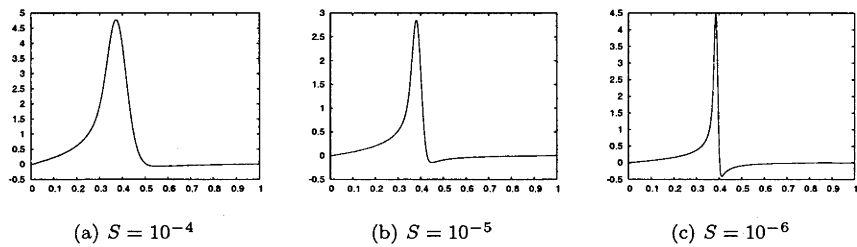


Figure 28: Radial plasma displacement of the dominant $m = 2/n = 1$ component of a tearing mode in a zero β current carrying heliotron as a function of normalised toroidal flux ψ . The vacuum rotational transform at the plasma edge, ι_0^δ , is 0.15, and the additional rotational transform at the plasma edge produced by toroidal currents, ι_0^σ , is 0.14.

7.19 LHD

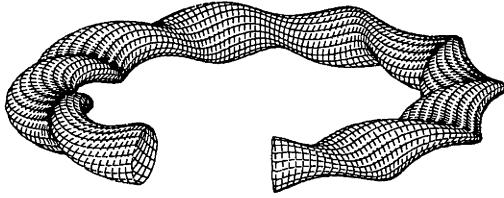


Figure 29: An outer vacuum flux surface of a 15cm inwards shifted LHD configuration. This serves as the plasma boundary for our LHD stability comparisons.

In this section we describe stability results for a set of configurations based on the LHD stellarator and used in earlier literature [47] for the comparison of various ideal MHD stability codes. First, we reproduce the published ideal MHD behaviour for small toroidal mode number. Then we consider the effects of resistivity applied to these test cases.

LHD is, at the time of writing, the world's largest stellarator; it has a major radius of 3.9m, and 10 field periods; the field is produced by a pair of helical coils and a set of poloidal field coils. It serves as a useful test case for high-dimensional codes because it has only a moderate amount of three dimensional shaping, reducing the requirements on poloidal and toroidal resolution. In the LHD configuration used for the comparison of stability codes coil currents are adjusted so that the magnetic axis is shifted 15cm inwards from its nominal position. An appropriate outer flux surface is then chosen to serve as the plasma boundary for a fixed boundary equilibrium calculation using the VMEC code. In order to ease comparison between the stability codes, which may not clearly resolve instabilities with small growth rates, a broad pressure profile was chosen, which induces a strong instability above a critical β . In this case, the largest pressure gradients occur nearer the edge of the plasma, where the magnetic field line curvature is strongly unfavourable. The resulting test case becomes Mercier unstable as β is increased. The codes under comparison in [47] are KSTEP, TWIST, TERPSICHORE, CAS3D, RESORM and CHAFAR. We give a brief overview of the most important differences in formulation amongst these codes and also between these codes and SPECTOR3D:

- Only TERPSICHORE and CAS3D are fully 3D codes, in the sense that they can resolve toroidal coupling. The other codes use toroidal averaging to reduce the stability problem to two dimensions.
- Most of the codes in this comparison make some modifications to the ideal MHD model for numerical convenience; TERPSICHORE and CAS3D (in

recent versions) can include the effects of compressibility, but in this comparison are incompressible and use a non-physical kinetic energy term, and other codes utilise reduced MHD or incompressibility assumptions. Such models have the same marginal stability point as ideal MHD, and the growth rates and eigenvalues of unstable modes are often very similar to those obtained by a full compressible ideal MHD analysis.

- Both fixed and free boundary conditions can be treated with many of these codes, unlike SPECTOR3D, which is a fixed boundary code.
- All the codes apart from RESORM, which includes resistivity in its formulation, are based on the ideal MHD equations.

The growth rates and wavemodes are strongly dependent on the details of the equilibrium. It is therefore helpful that we use the same equilibrium input format (VMEC output) as many of the codes in the study, and we have been able to obtain this output from one of the authors of the study. Furthermore, because we are using a module from TERPSICHORE for Boozer coordinate mapping, we can isolate the comparison between our code and TERPSICHORE to the stability sections of the codes.

The shape of the pressure profile is particularly important for the purposes of this comparison. We use the profile $p = (1 - \psi^2)^2$, where ψ is the normalised toroidal flux. This is the profile known as p_{II} in [47]. There are several other possibilities considered in [47], but because VMEC takes a polynomial function of the toroidal flux as its input for the pressure profile, this is the most convenient. Using $p = (1 - \phi^2)^2$, with ϕ the normalised poloidal flux, leads to a rather different set of instabilities, whose squared growth rates are different by approximately a factor of ten.

Two toroidal mode families are chosen for stability analysis, with $n_0 = 2$ and $n_0 = 3$. Because many of the codes under comparison use a form of toroidal averaging, a test case was specified where toroidal coupling was not likely to be important. The absence of strong toroidal coupling was confirmed in [47] by examining the results of the fully 3-D codes. We also resolve a certain amount of toroidal coupling with Spector3D, induced mostly by the helical flux surface shaping, with most of the toroidal coupling between components with $\delta m / \delta n = 2/10$, as shown in figure 31.

We omit toroidal coupling for the purposes of the rest of the comparison, and instead use our numerical resources to increase radial resolution, because the most unstable mode has a sharp peak, especially near the marginal stability point. We resolve poloidal wavenumbers in the range $[-2, 12]$ to include not only the perturbations resonant with the rational magnetic surface, but also the

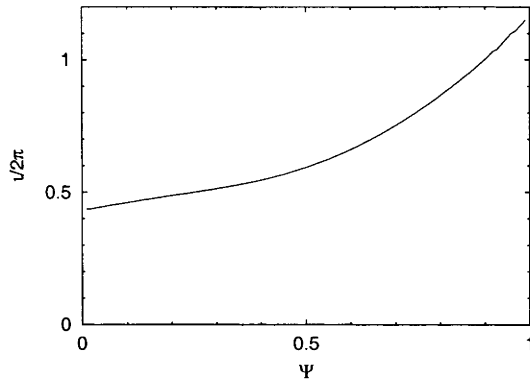


Figure 30: The rotational transform of the LHD testcase as a function of the normalised toroidal flux for $\beta_0 = 4.1\%$.

effects of the non-resonant modes which can be important when the equilibrium contains significant toroidicity. We choose 100 evenly spaced finite element grid points. For the $n_0 = 2$ case we determine the growth rates and wavenodes for a range of different β values. The stability parameter Λ we find is plotted alongside that from KSTEP and TERPSICHORE in figure 32 as a function of β_0 . We have $\beta_0 = 2p_0/B_0^2$, where p_0 is the non-dimensional pressure at the magnetic axis, and B_0 is the non-dimensional magnitude of the vacuum field at the major radius $R_0 = 3.74\text{m}$. The stability parameter Λ is related to the growth rate ω from SPECTOR3D through the relation $\Lambda = \omega^2[\rho R_0^2/B_0^2]$. As is conventional for stellarator stability analysis, ρ is taken to be constant across the radius. It can be seen that there is relatively good agreement among the three codes, even though we are finding the compressible growth rates, and the other codes are using reduced MHD or a model kinetic energy term. The radial displacements associated with the most important Fourier components of the instability are shown in figure 33, for a fixed boundary mode with a dominant $n = 2$ component. Near the critical β value these eigenmodes are very strongly radially localised, and are composed almost entirely of one Fourier component, but they become much smoother for higher β , where many Fourier modes contribute significantly.

To examine the effects of resistivity on the stability of this testcase, we find the most unstable eigenvalue (figure 35) as a function of β_0 for several values of the Lundquist number S . The ideal growth rates are shown for comparison. Unstable modes are found below the predicted ideal MHD marginal stability point with resolvable growth rates, localised in the region of strong pressure gradients: this is consistent with the local stability criteria plotted in figure

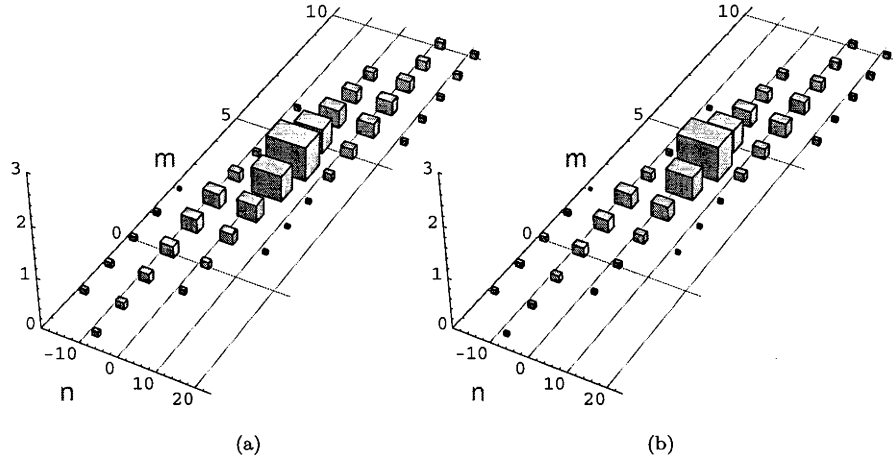


Figure 31: The strength of various Fourier components of the most unstable ideal MHD mode in LHD for $\beta_0 = 4.1\%$ (left), and of the most unstable resistive MHD mode with $S = 10^6$ for $\beta_0 = 3.0\%$ (right). The volumes of boxes in the figure are proportional to the maximal radial displacement found for each mode.

34. The eigenfunctions and eigenvalues of the strongly unstable ideal modes are not significantly altered by the addition of small values of resistivity, as is expected for these smooth, well isolated global instabilities. However, the effect of resistivity is mainly interesting where the ideal modes are stable, or almost stable. For this model, there are unstable resistive modes with significant growth rates for all values of β_0 for $S = 10^5$. However, for low resistivity ($S > 10^5$), the growth rates of these resistive modes is only significant above $\beta_0 \simeq 1\%$.

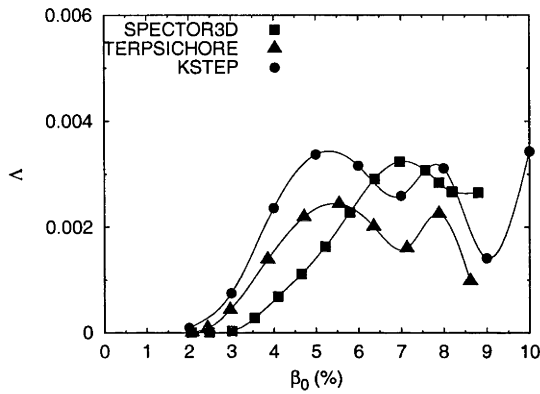


Figure 32: The largest instability value Λ as a function of plasma pressure β_0 for ideal modes with $n = 2$ in a LHD equilibrium with a broad pressure profile.

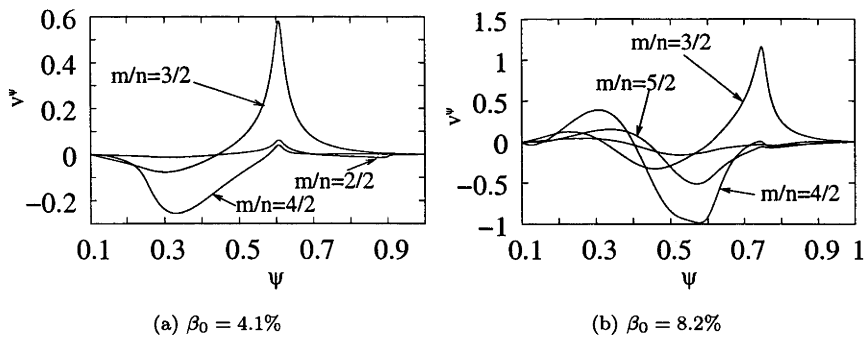


Figure 33: The radial displacements for the most significant Fourier components of the most unstable $n = 2$ mode in a broad pressure profile LHD configuration for various values of β_0 .

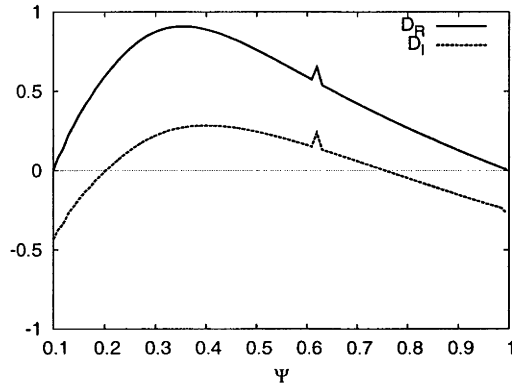


Figure 34: The Mercier criterion D_I governing ideal interchange stability and the resistive interchange stability criterion D_R , plotted versus normalised toroidal flux ψ , for a broad pressure profile LHD configuration with $\beta_0 = 2\%$. $D_I < 0$ and $D_R < 0$ are necessary criteria for ideal and resistive stability, respectively.

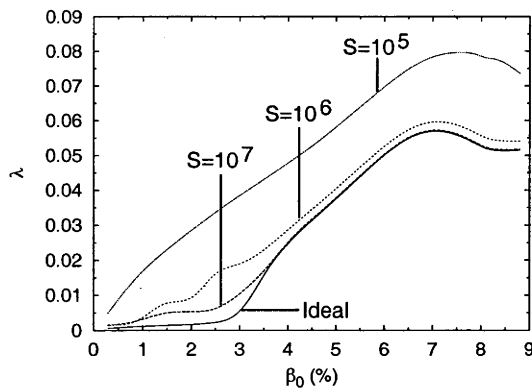


Figure 35: The largest instability growth rate λ resolved by SPECTOR3D as a function of plasma pressure β_0 for resistive modes with $n = 2$ in an LHD equilibrium with a broad pressure profile.

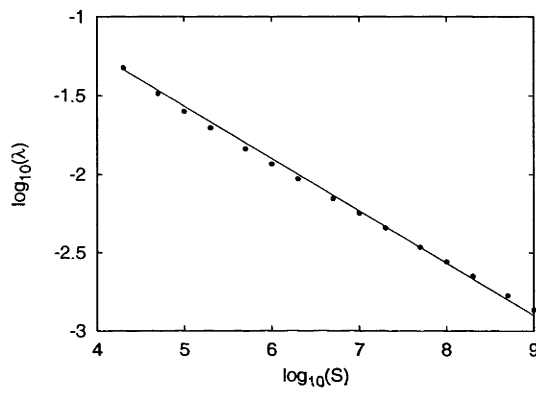


Figure 36: The largest instability growth rate λ (points) as a function of S for $n = 2$ modes in an LHD equilibrium with a broad pressure profile and $\beta_0 = 2\%$. The growth rate scaling conforms closely to the expected scaling for resistive interchange modes, $\omega \propto S^{1/3}$, which is the line plotted in the figure.

8 Stellarator stability with respect to global kinetic ballooning modes.

8.1 Summary

Ballooning modes are usually the most dangerous ideal MHD instabilities in stellarators, but the unstable ballooning modes often have such short perpendicular wavelengths that finite Larmor radius (FLR) effects are sufficient to stabilise the plasma. We use semiclassical techniques to analyse this effect. In tokamaks the ignorable toroidal coordinate leads to a simple quantisation of the ballooning mode, but this is not the case for stellarators. Although for stellarator models there is sometimes a quantisation which arises from a separation of scales, we present a method for determining marginal stability which is applicable to the non-integrable case.

8.2 Introduction

There are obvious physical reasons for considering the FLR stabilisation of the ideal MHD model, but there is also a compelling theoretical reason: MHD theory lacks an intrinsic scale length. This can be seen, for example, in the local dispersion relation for shear Alfvén waves in the interchange ordering, which is asymptotically independent of the wavelength perpendicular to the magnetic field. The independence of scale leads to singularities, which are particularly troubling in stellarators, where the unstable modes may have singular angular dependence over a range of flux surfaces [57]. In axisymmetric systems, such singularities cannot arise because only a finite number of Fourier harmonics can contribute significantly to the mode. The reason is that shear Alfvén waves of different toroidal wavenumber n do not couple together in axisymmetric systems and there is a natural cutoff in poloidal wavenumber space for each n which arises from the requirement that unstable modes are flute-like, with $m/n \approx q$. On the other hand, for non-axisymmetric systems there is no natural cutoff in poloidal wavenumber, as modes may couple to arbitrarily high toroidal wavenumber. In [57] ideal MHD ballooning modes were studied in a fully three dimensional configuration, and it was shown how the absence of such a cutoff complicates the analysis. For some cases this entirely confounds quantisation, but even where it is possible to extract a quantisation condition, the eigenmodes are predicted to be singular functions of the poloidal angle. Such generalised eigenmodes cannot be directly interpreted as motions of a real plasma; they arise here because the system can transport wave energy to arbitrarily short wavelength. This is not unusual: a well known example of this kind of energy transport occurs in

a stable cylindrical plasma with a radially varying Alfvén frequency, where an initially smooth perturbation evolves into a state with strong radial variation as the Alfvén modes dephase. At some point in this evolution, the wavenumber will grow large enough that the ideal MHD model becomes inadequate. In order for the model to be valid as $t \rightarrow \infty$ (which is the relevant limit for the eigenmode picture) non-ideal effects need to be included. Such effects desingularise the problem by introducing a (physical) wavelength cutoff, and may lead to a stabilisation or destabilisation of the plasma.

For tokamaks a straightforward semiclassical analysis is enough to find the eigenmodes and eigenvalues of kinetically stabilised ballooning modes; the toroidal symmetry leads to a good quantum number, and the rest of the dynamics occur in a one degree of freedom Hamiltonian system, which is necessarily integrable. In a nonaxisymmetric mirror configuration [14], it was shown how semiclassical quantisation could be extended to systems lacking a continuous spatial symmetry if a separation of timescales in the ray dynamics exists, so that the problem is nearly integrable. We extend the analysis to the regime where there is no separation of timescales, and chaos is present in part or all of the phase space.

For systems whose semiclassical ray orbits exhibit even quite substantial non-integrability, it has been shown that near-integrable semiclassical theory can provide very good estimates of eigenvalues [58]. The non-integrability does not need to be neglected, and the parameters which enter the formula can be easily and accurately measured. We apply this technique to a system in which almost half the semiclassical phase space is ergodic.

One of the signatures of strong semiclassical chaos is in the more subtle features of the spectrum, like those predicted by random matrix theory. This is the topic of [26], where they find that the eigenvalue spacing probability distribution function of a numerical ideal MHD spectrum agrees nicely with random matrix theory. However, for the purpose of marginal stability analysis, sufficient information about the distribution of eigenfrequencies in the strongly chaotic case can be derived by applying the Weyl estimate, which we review in section 8.11; this was utilised in [16] as a tool for ballooning mode stability analysis. In that paper an artificial cutoff was introduced, intended to model finite resolution in numerical studies of ballooning stability; we consider the more physical case.

We begin the analysis by exploring the drift stabilised MHD model and explaining how the use of semiclassical analysis can be justified in this system where fully complex wave frequencies arise.

8.3 A review of the ballooning mode formalism

The ballooning mode formalism is structured around the observation that many of the most dangerous unstable MHD modes are flute-like: they vary slowly along the magnetic field, but have short perpendicular wavelengths. It is often possible to find a sequence of increasingly unstable modes for which $k_{\perp} \rightarrow \infty$. The form of such perturbations can be captured by the semiclassical representation

$$\xi_{\perp} = \eta_{\perp} e^{iS} \quad (117)$$

with η_{\perp} varying slowly, and

$$\mathbf{B} \cdot \nabla S = 0. \quad (118)$$

The perpendicular wavenumber is defined via $\mathbf{k}_{\perp} = \nabla S$. In this section we will use the standard ballooning coordinate system described in [57] where the flux surface is parameterised by a poloidal angle θ and the field line label α . The field line label α runs between 0 and 2π over one toroidal traversal of the device. The choice of the safety factor q as the radial coordinate is also standard, as it simplifies the analysis. In this coordinate scheme we represent the perpendicular wave vector \mathbf{k} as

$$\mathbf{k} = k_{\alpha} \nabla \alpha + k_q \nabla q \quad (119)$$

We then proceed to systematically minimise the ideal MHD energy principle (12) for these flute like perturbations, after expanding η_{\perp} in terms of the small ordering parameter, $1/|k_{\perp}|a$, which is the ratio of the wavelength to the system scale length. The zeroth order of the expansion of equation (12) leads to $\mathbf{k}_{\perp} \cdot \boldsymbol{\eta}_{\perp 0} = 0$, allowing us to express $\boldsymbol{\eta}_{\perp 0}$ through a scalar Y ,

$$\boldsymbol{\eta}_{\perp 0} = Y \mathbf{b} \times \mathbf{k}_{\perp}. \quad (120)$$

The next contributions to equation (12) are at second order, leading to

$$\frac{1}{2\mu_0} \int dV \left[k_{\perp}^2 |\mathbf{b} \cdot \nabla X|^2 - \frac{2\mu_0}{B^2} (\mathbf{b} \times \mathbf{k}_{\perp} \cdot \nabla p) (\mathbf{b} \times \mathbf{k}_{\perp} \cdot \boldsymbol{\kappa}) \right] \quad (121)$$

where $\boldsymbol{\kappa} = \mathbf{b} \cdot \nabla \mathbf{b}$ is the field line curvature, and $X = YB$. These terms represent the balance between the destabilising effect of unfavourable curvature and the stabilising effect of field line bending.

Because S is constant on any particular field line, \mathbf{k}_{\perp} twists along a field line according to the shear of neighbouring magnetic field lines. X is the only

perturbing quantity that can be varied on field lines: only the derivative of X parallel to the field line is present in equation (121) so the minimisation can be considered separately on each field line; this leads to a one-dimensional differential equation for X . The solution to this equation is dependent on the choice of field line and the value of \mathbf{k}_\perp at toroidal angle $\zeta = \zeta_0$ (ζ_0 is arbitrary).

The next step is to determine whether solutions to this field line equation exist. In toroidal systems this reduces to determining whether the solutions are compatible with the toroidal and poloidal periodicity requirement. On rational surfaces it is possible to find ballooning eigensolutions, but in systems with shear the consequence of imposing the periodicity requirement on the phase S is that no solutions exist. However, this periodicity constraint is unnecessarily restrictive: it is possible for semi-classical solutions to have multi-valued representations which, when summed, satisfy the periodicity constraints even when the individual terms of the representation are not periodic.

The concept of a covering space is useful in describing the multi-valued semiclassical solution we wish to use to describe the ballooning perturbation. The idea is to choose a covering space (in this case an infinite plane), and deform it via a continuous mapping onto the space of the physical problem (a torus). We then solve the ballooning equation on the covering space, analogously to the demonstration in figure 37. The mapping we take (a simple periodic wrapping in both directions) maps an infinite number of points on the plane to a single point on the torus. The solution on the plane is then wrapped onto the torus, and the solution on each sheet of the wrapping is superimposed: this ensures the periodicity of the solution. The solution is then

$$\xi'_\perp = \sum_{m=-\infty}^{\infty} \sum_{n=-\infty}^{\infty} \eta_\perp(\theta - 2\pi m, \alpha - 2\pi n) e^{iS(\theta - 2\pi m, \alpha - 2\pi n)}. \quad (122)$$

where $S(\theta, \alpha)$ and $\eta(\theta, \alpha)$ are now defined on the infinite plane and we have suppressed the radial dependence. Lines of constant α are wrapped onto field lines in this mapping, and cover irrational surfaces densely. We require the function η_\perp be normalisable on the covering space to guarantee that the sum is meaningful.

We now consider a more explicit form of the ballooning equation [59],

$$\left(\frac{d}{d\theta} A \frac{d}{d\theta} - K - \omega^2 N \right) \eta = 0 \quad (123)$$

with coefficients given by

$$A = \frac{1}{J|\nabla\Psi|^2} + \frac{|\nabla\Psi|^2}{JB^2} [R + (\partial_{\mathbf{v}}q)(\theta - \theta_k)]^2, \quad (124)$$

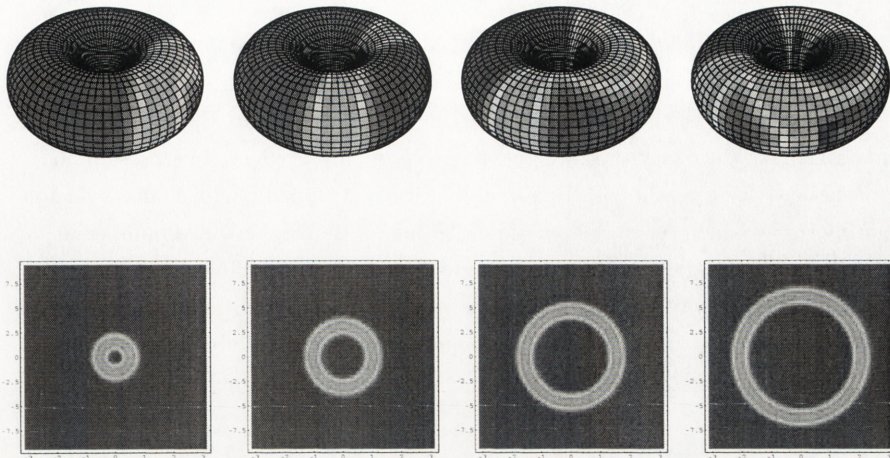


Figure 37: A wave propagating around a torus intersects with itself in a complicated fashion. The lower figure shows a simple circularly symmetric wave on the plane. Wrapping the plane around the torus and superimposing the amplitudes constructs the complicated structure of the wave on the torus. This illustrates the utility of the covering space, where solutions often have much simpler spatial structure due to the relaxation of the periodicity constraints.

$$K = \frac{2J\partial_{\Psi}p}{|\nabla\Psi|} \left\{ \kappa_n + \frac{|\nabla\Psi|^2}{B} [R + (\partial_{\Psi}q)(\theta - \theta_k)] \kappa_g \right\}, \quad (125)$$

$$N = J^2 A \quad (126)$$

where the local integrated shear is given by $R + \theta\partial_{\Psi}q = -\nabla\alpha \cdot \nabla\Psi / |\nabla\Psi|^2$, and the normal and geodesic components of the magnetic curvature vector $\kappa = \mathbf{b} \cdot \nabla\mathbf{b}$ are given by $\kappa_n = \kappa \cdot \nabla\Psi / |\nabla\Psi|$ and $\kappa_g = \kappa \cdot \nabla\Psi \times \mathbf{B} / |B\nabla\Psi|$ respectively. The background magnetic field and pressure are B and p , and J is the Jacobian. The phase fronts are sheared with the magnetic field as we proceed along a field line; $\theta_k = k_q/k_{\alpha}$ is the poloidal angle where the local ballooning phase fronts are perpendicular to $\nabla\alpha$.

Although this ballooning equation should in principle be solved along the entire infinitely long field line, numerical analysis on a finite segment of the field line is sufficient if the ballooning eigenfunction converges to zero along the field line sufficiently quickly. It can be shown that the convergence criterion is simply the Mercier criterion [10]: this is evident in many derivations of the Mercier criterion [33].

8.4 Kinetic corrections to Ideal MHD ballooning

In order to account for effects beyond ideal MHD, the ballooning ordering can be applied to more general plasma models. In particular, we utilise the results of [60], where the ballooning ordering is applied to the Maxwell-Vlasov equations and various limits are taken. Two separate effects are present in the kinetic ballooning model, corresponding to the trapped particle effects and the finite-gyroradius term. For modes with moderate toroidal wavenumber, it can be shown that the dominant non-ideal effect is the stabilisation due to the diamagnetic drift. We will ignore the relatively small additional stabilising effects of the curvature drift. In this regime, the kinetic ballooning equations are given in terms of the ideal MHD ballooning equation by the replacement:

$$\omega^2 \rightarrow \omega(\omega + \omega_*) \quad (127)$$

as in [60] (where the notation is slightly different) or [14], where

$$\omega_* = \frac{cT}{eBp} \mathbf{k} \cdot \hat{\mathbf{B}} \times \nabla p \quad (128)$$

is the diamagnetic drift frequency for the wave under consideration. We define the flux surface quantity Ω_i such that

$$\omega_* = \Omega_i k_\alpha \quad (129)$$

On each field line this kinetic effect is equivalent to a simple frequency shift, and the eigensolution of the ballooning equation along the field line is not modified by kinetic effects: we can calculate the local kinetic growth rates from the ideal growth rates by substituting equation (127) into the local ideal MHD dispersion relation. The region of ideal MHD instability is commonly fairly radially localised, and since ω_* varies on the equilibrium scale, it is set to a constant for the purposes of our analysis.

The formal semiclassical quantisation of a system begins with the calculation of the dispersion relation; the next step is to determine the ray equations which govern the transport of the local phase, and the equation which governs the transport of the amplitude. The ray and amplitude equations can be determined from general considerations [37] for any wave equation which admits an integral form, and in particular for the differential equations which we are interested in. The wave equation which is relevant here is the linearised form of the Vlasov–Maxwell equations, but we use the approximate dispersion relation given by the ballooning ordering. The semiclassical ray equations can be

expressed through the dispersion relation as

$$\frac{d\mathbf{y}}{d\tau} = \alpha[\mathbf{k}(\mathbf{y}), \mathbf{y}, \omega] \frac{\partial}{\partial \mathbf{k}} |\Lambda[\mathbf{k}(\mathbf{y}), \mathbf{y}, \omega]| \quad (130)$$

and

$$\frac{d\mathbf{k}}{d\tau} = -\alpha[\mathbf{k}(\mathbf{y}), \mathbf{y}, \omega] \frac{\partial}{\partial \mathbf{y}} |\Lambda[\mathbf{k}(\mathbf{y}), \mathbf{y}, \omega]| \quad (131)$$

where the choice

$$\alpha[\mathbf{k}(\mathbf{y}), \mathbf{y}, \omega] = \frac{1}{|\Lambda[\mathbf{k}(\mathbf{y}), \mathbf{y}, \omega]|} \quad (132)$$

gives the conventional form for geometrical optics. The same method [37] can in general be used to find the amplitude evolution, but it is more enlightening and more elegant to derive the amplitude evolution via Lagrangian techniques. The Vlasov–Maxwell equations can be derived via a variational principle [61] [62], and this implies the existence of several conserved quantities. Using the notation of [63], we can express the conservation conditions as

$$\frac{dT_{\mu\nu}}{dx_\nu} = -\frac{\partial \mathcal{L}}{\partial x_\mu} \quad (133)$$

with

$$T_{\mu\nu} = \frac{\partial \mathcal{L}}{\partial \eta_{\rho,\nu}} \eta_{\rho,\mu} - \mathcal{L} \delta_{\mu\nu}, \quad (134)$$

$x_0 = t$ and $(x_1, x_2, x_3) = (\alpha, q, s)$. There is an implied sum over indices which appear in pairs. The Lagrangian density \mathcal{L} is usually a function of $x, \boldsymbol{\eta}$ and $\partial\boldsymbol{\eta}/\partial x$ and derivatives of $\boldsymbol{\eta}$ with respect to time; the total derivative in equation (133) takes into account the x dependence of $\boldsymbol{\eta}$ and its derivatives in the Lagrangian density. We are interested in the $\mu = 0$ component of equation (133) which is typically associated with energy conservation. We show how this leads to a conservation of wave action for systems in which the Lagrangian can be (approximately) minimised by a semiclassical trial solution of the form

$$\boldsymbol{\eta} = \hat{\boldsymbol{\eta}}(\mathbf{r}) \exp[iS(\mathbf{r})\hbar - i\omega t], \quad (135)$$

with \hbar a small parameter and wavevector defined by $k = \nabla S$. The slow variation along the field can be captured entirely by the function $\hat{\boldsymbol{\eta}}$, so we set $\mathbf{k} \cdot \mathbf{B} = 0$ and specialise to flute-like modes.

The semiclassical ordering applies across the field line so that $\eta_{\rho,\nu} \simeq k_\nu \eta_\rho$

for $\nu \in 1, 2$. Expanding the $\mu = 0$ component of equation (133) leads to

$$\omega \left(\frac{d}{d\alpha} \frac{\partial \mathcal{L}}{\partial k_\alpha} + \frac{d}{dq} \frac{\partial \mathcal{L}}{\partial k_q} + \frac{d}{ds} \left[\frac{\partial \mathcal{L}}{\partial \eta_{\rho,s}} \eta_{\rho,s} \right] \right) - \mathcal{L} = -\mathcal{L}. \quad (136)$$

When the configuration is Mercier stable [33], the solutions $\hat{\eta}(\mathbf{r})$ asymptotically tend to zero along the field lines. In this case we can integrate along the field line to find

$$\frac{d}{d\alpha} \frac{d\bar{\mathcal{L}}}{dk_\alpha} + \frac{d}{dq} \frac{d\bar{\mathcal{L}}}{dk_q} = 0 \quad (137)$$

where $\bar{\mathcal{L}}$ is the field-line-integrated Lagrangian. The eigensolutions $\hat{\eta}$ are proportional to the ideal MHD ballooning eigenfunctions,

$$\hat{\eta}(\theta|\alpha, q, \theta_k, k_\alpha, \omega^2) = p(k_\alpha) \hat{\eta}_{\text{MHD}}(\theta|\alpha, q, \theta_k, \omega(\omega - k_\alpha \Omega_i)) \quad (138)$$

for which we choose the conventional normalisation

$$\frac{\partial \bar{\mathcal{L}}_{\text{MHD}}[\hat{\eta}_{\text{MHD}}(\omega^2)]}{\partial(\omega^2)} = 1. \quad (139)$$

We then normalise the ballooning eigenfunctions of the kinetic model, for which we have $\bar{\mathcal{L}}[\hat{\eta}_{\text{MHD}}(\omega)] = \bar{\mathcal{L}}_{\text{MHD}}[\hat{\eta}_{\text{MHD}}(\omega\{\omega - \Omega_i k_\alpha\})]$, in the same way:

$$1 = \frac{\partial \bar{\mathcal{L}}[\eta(\omega)]}{\partial \omega} = p^2(k_\alpha) \frac{\partial \bar{\mathcal{L}}_{\text{MHD}}[\hat{\eta}_{\text{MHD}}(\omega\{\omega - \Omega_i k_\alpha\})]}{\partial \omega} = (2\omega - \Omega_i k_\alpha) p^2(k_\alpha) \quad (140)$$

So that we require

$$p^2(k_\alpha) = 1/(2\omega - \Omega_i k_\alpha). \quad (141)$$

The semiclassical solution in configuration space is

$$\eta = a_q \exp[iS(\alpha, q)] \hat{\eta}(\theta|\alpha, q, \theta_k, k_\alpha, \omega^2) \quad (142)$$

where we use the notation $a_q = a_q(\alpha, q)$ for the amplitude in configuration space. An analogous representation is possible in momentum space with amplitude $a_p = a(k_\alpha, k_q)$. Minimising the Lagrangian with respect to the wave amplitude gives $\bar{\mathcal{L}}[\eta] = 0$; we can then insert the definition of the semiclassical solution

[equation (142)] into the Lagrangian to find the relations

$$\frac{d\bar{\mathcal{L}}[\eta]}{dq} = a_q^2 \frac{\partial \omega}{\partial q} \quad (143)$$

$$\frac{d\bar{\mathcal{L}}[\eta]}{d\alpha} = a_q^2 \frac{\partial \omega}{\partial \alpha} \quad (144)$$

$$\frac{d\bar{\mathcal{L}}[\eta]}{dk_q} = a_p^2 \frac{\partial \omega}{\partial k_q} \quad (145)$$

$$\frac{d\bar{\mathcal{L}}[\eta]}{dk_\alpha} = a_p^2 \frac{\partial \omega}{\partial k_\alpha} \quad (146)$$

since the Lagrangian is bilinear, and the phase and amplitude factor out. Equation (137) can then be expanded in its original form or with the order of differentiation swapped, to give conservation conditions both in momentum and configuration space,

$$\frac{d}{d\alpha} \left(a_q^2 \frac{\partial \omega}{\partial k_\alpha} \right) + \frac{d}{dq} \left(a_q^2 \frac{\partial \omega}{\partial k_q} \right) = 0, \quad \text{and} \quad (147)$$

$$\frac{d}{dk_\alpha} \left(a_p^2 \frac{\partial \omega}{\partial \alpha} \right) + \frac{d}{dk_q} \left(a_p^2 \frac{\partial \omega}{\partial q} \right) = 0. \quad (148)$$

This can be used to determine the time evolution of the amplitudes along the ray determined by equations (130) and (131),

$$\frac{da_q^2}{dt} = \frac{\partial a_q^2}{dq} \frac{dq}{dt} + \frac{\partial a_q^2}{d\alpha} \frac{d\alpha}{dt} \quad (149)$$

$$= \frac{\partial}{\partial q} \left(a_q^2 \frac{\partial \omega}{\partial k_q} \right) - a_q^2 \frac{\partial^2 \omega}{\partial q \partial k_q} + \frac{\partial}{\partial \alpha} \left(a_q^2 \frac{\partial \omega}{\partial k_\alpha} \right) - a_q^2 \frac{\partial^2 \omega}{\partial \alpha \partial k_\alpha} \quad (150)$$

$$= -a_q^2 \nabla \cdot \mathbf{v} \quad (151)$$

where $\mathbf{v} = (dq/dt, d\alpha/dt)$ is the ray velocity. The divergence has singularities at caustics, where the momentum description should be used, but otherwise is well behaved. The conserved quantity is actually the phase space density $a^2(\alpha, q, k_\alpha, k_q)$ defined jointly in momentum and position space; this quantity is analogous to the conserved brightness of a propagating light field. This advection of wave action is conceptually the same as its quantum mechanical counterpart, but the wave action of interest is not proportional to the square of the wave amplitude.

The form of the normalisation in equation (141) implies that the physical displacements associated with the semiclassical solution might be singular at the marginal stability point, where $2\omega - \Omega_i k_\alpha = 0$, even though the phase space density a^2 is conserved. Generally there is no physical singularity because wave

solutions do not simultaneously possess a well-defined momentum and position, so that the singularity is averaged out over a number of wavelengths. However, in the semiclassical limit, where $\hbar \rightarrow 0$, we would expect modes to become increasingly singular at this surface. This is typical of strongly non-normal wave systems where, even though there is an approximately conserved quantity, the physical displacements are not well bounded in the $\hbar \rightarrow 0$ limit. However, the equilibrium is unstable in this limit anyway.

It is relevant at this stage to consider how the use of a Lagrangian formulation is justified in this situation, in which fully complex frequencies can arise, even though there is no dissipation. Typically the eigenfrequencies of Lagrangian wave problems are either real (as in quantum mechanics) or lie on the axes of the complex plane (as in ideal MHD). This is because the time derivative occurs only in a single order in the Lagrangian of these systems. In our system both $\partial/\partial t$ and $\partial^2/\partial t^2$ occur, leading to the term $\omega(\omega - k_\alpha \Omega)$. The eigenvalue problem associated with the Lagrangian is of the form $\omega^2 \mathbf{A}\boldsymbol{\eta} + \omega \mathbf{B}\boldsymbol{\eta} + \mathbf{C}\boldsymbol{\eta} = 0$, which in general has complex eigensolutions even when the matrices \mathbf{A} , \mathbf{B} and \mathbf{C} are Hermitian. It is relatively straightforward to show that the terms in the Lagrangian are Hermitian: it is well known that the ideal MHD force operator is Hermitian, as is the additional term $i\omega\Omega_i \partial/\partial \alpha$ which in the semiclassical limit gives the contribution $-k_\alpha \omega \Omega_i$ to the dispersion relation.

Now that we have described the spatial variation of the semiclassical phase and amplitude, we have a complete description of the wave problem in the short wavelength limit, as any wave which satisfies the semiclassical equations will approximately solve the exact problem. In the integrable case it is possible to construct approximate eigensolutions to the wave equations via Einstein–Brillouin–Keller (EBK) quantisation: these converge to the exact solutions in the semiclassical limit. In the chaotic and near-integrable case, the time-dependent solutions of the wave equations are still straightforwardly accessible through the semiclassical technique, and can be shown to correspond in the semiclassical limit to the exact solutions, but it is difficult to construct the eigenfunctions explicitly. An indirect approach which considers the response of the system to periodic perturbations is more fruitful; the semiclassical trace of the Green’s function can be shown to converge (in a restricted sense) to the exact Green’s function. These approaches rely only on a conservative semiclassical formulation of the wave problem, rather than any special properties of quantum mechanics: this can be seen by examining the derivation of the trace formula, which is accessibly described in [22].

8.5 Einstein–Brillouin–Keller quantisation

For systems with a full set of quantum numbers, semiclassical rays propagate on topologically toroidal surfaces in phase space known as Lagrangian manifolds or Kolmogorov–Arnold–Moser (KAM) tori. In systems which are close enough to an integrable system, the KAM theorem guarantees that the phase space will consist almost entirely of a nested set of these KAM tori. A quantised wave function can be constructed if it is possible to assign well-behaved phase to each point on some KAM torus, consistent with the semiclassical ray equations which transport the phase along the Lagrangian surface. However, the projection of this manifold onto *configuration space*, the space associated with the positions q , is usually multivalued, and the semiclassical amplitude of the wave function diverges at the boundaries of the layers of the Lagrangian manifold. One approach to resolving the wave near the edges of the layers is to use a boundary layer approach, but this requires a new solution to our original set of differential equations. A more elegant approach is to consider the momentum space representation of the solution,

$$\Psi_p = A(\mathbf{p}) \exp\{-i\hbar S(\mathbf{p}, \mathbf{I}) + i\beta\}, \quad (152)$$

which approximates the Fourier transform of the configuration space solution. To satisfy the wave equation, the action $S(p)$ is defined by integrating the phase along the ray, so that

$$S(\mathbf{p}) = \int_{p_0}^p \mathbf{q}(\mathbf{p}) \cdot d\mathbf{p}. \quad (153)$$

This momentum representation of the semiclassical wavefunction is also multivalued and cannot be continued smoothly across the entire Lagrangian manifold. However, it can be shown that the points where the momentum space and position space representations break down never coincide. To find the complete semiclassical wavefunction it is therefore necessary to match the two representations together at various points: they are related via the Fourier transform

$$A(\mathbf{q}) \exp[i\hbar S(\mathbf{q})] \simeq \int d\mathbf{p}' A(\mathbf{p}') \exp[-i\hbar S(\mathbf{p}')] \exp[i\mathbf{p}\mathbf{q}']. \quad (154)$$

This Fourier transform can be evaluated in a region away from the boundary (where *caustics* form) via a stationary phase approximation. This gives a relationship for the phases $S(\mathbf{p})$ and $S(\mathbf{q})$,

$$\mathbf{p}(\mathbf{q})\dot{\mathbf{q}} - S(\mathbf{p}(\mathbf{q}), I) = S(\mathbf{q}). \quad (155)$$

Near the caustics it is possible to perform a canonical transformation on the coordinates $(\mathbf{p}, \mathbf{q}) \rightarrow (\mathbf{p}', \mathbf{q}')$ so that the phase $S(\mathbf{p}')$ corresponds to one of the finite set of *normal forms*. The Fourier transform of the momentum representation can then be found analytically. In the generic case where there is a fold in the Lagrangian surface, the action $S(p_{\perp}) \sim -p_{\perp}^3$ perpendicular to the fold, and the Fourier transform is an Airy function. The matching is completed by requiring the asymptotic oscillation of this function match the configuration space wavefunction; this implies that there is an additional phase change of $\pi/2$ whenever the ray crosses the boundary between two sheets of the Lagrangian manifold. This is included in the semiclassical phase through the *Maslov index* μ , which counts the number of folds encountered.

In the multidimensional case, the phase can be propagated along the surface and back to some original point by a continuous family of curves. In order for the phase to be well defined, we require that the phase propagated around the curve, S_1 , be equal to the original phase at that point, S_0 , plus some multiple of 2π for any such curve. However, this phase difference can be shown to be equal for any pair of topologically equivalent loops on the Lagrangian surface, so that it is sufficient to simply consider the N independent loops which form a basis on the surface; the two loops in figure 41, for example, are sufficient. We then have N independent quantisation conditions,

$$\int \mathbf{p} \cdot \mathbf{q} = 2\pi I_l = 2\pi\hbar \left(n_l + \frac{\mu_l}{4} \right). \quad (156)$$

which are the Einstein–Brillouin–Keller (EBK) quantisation conditions.

8.6 Quantisation in near-integrable systems

The discovery by Gutzwiller [64] of a semiclassical formula for the density of states in a system based on the periodic orbits of semiclassical rays opened up a new perspective on the quantisation of wave systems. Because periodic orbits are the foundation of dynamical systems theory, a semiclassical quantisation based on these orbits is a vital bridge between the dynamics of wave systems and those of low dimensional Hamiltonian systems. However, for integrable and near integrable systems, the formula of Gutzwiller cannot be applied, as it depends on the periodic orbits being well isolated in the phase space. This is the case for only a small proportion of the orbits of a near-integrable system, even in the $\hbar \rightarrow 0$ limit. Also, although EBK quantisation is also an effective method for quantising integrable systems, it cannot systematically address issues such as the bifurcation of periodic orbits or small departures from integrability.

A quantisation of integrable systems in terms of periodic orbits was provided

by Berry and Tabor. For near integrable systems, the theory was extended by Ozorio de Almeida [65] to include the effects of resonances which break the invariant tori, although the practical application of the theory was limited because of the strict conditions for the application of this theory. A simple and accurate method for applying the corrections was derived in [66]: the application of this method to the hydrogen atom in a magnetic field in [58], which is a canonical problem in semiclassical quantisation, was an important milestone.

Expressions like the Berry–Tabor and Gutzwiller formulae are known as trace formulae, because they can be derived by taking the trace of the Green’s function, $G(\mathbf{q}, \mathbf{q}', \omega)$, which measures the response at point \mathbf{q} of the system to periodic perturbations at point \mathbf{q}' . At eigenfrequencies, the system response is singular, and there is a corresponding pole in the trace $\int_{\mathbf{q}} d\mathbf{q} G(\mathbf{q}, \mathbf{q}, \omega)$. The actual evaluation of the trace in the short wavelength limit involves a stationary phase approximation, and the dominant contributions to the trace integral are from semiclassical rays which close on themselves in phase space, which are known as periodic orbits. This is the point where the Gutzwiller and Berry–Tabor formalisms diverge, because in the former, periodic orbits are assumed to be isolated in phase space, as is typical of chaotic systems, whereas in the latter, they occur in continuous families, spread across a rational invariant torus.

In the intermediate case where the periodic orbits are not sufficiently isolated to justify independent stationary phase approximations, but do not occur in continuous families, it is still possible to use a stationary phase argument to integrate the trace over the directions perpendicular to the Lagrangian surface, but the integral on the surface which contains the phase variation must be evaluated explicitly. An elegant method to perform such integrals was given by [66], where a formula is given in terms of periodic orbit quantities; this gives a smooth interpolation between the Gutzwiller and Berry–Tabor limits.

8.7 Semiclassical analysis of ballooning modes

Although there are some notable exceptions [67] it is difficult to find analytic representations of global ballooning wavefunctions in 2D and 3D systems.

The drift stabilised MHD ballooning model has a dispersion relation of the form:

$$D(k_\alpha, k_q, \alpha, q) = \Omega^2 - \omega(\omega - k_\alpha \Omega_i) = 0 \quad (157)$$

The term Ω_i models the drift stabilisation and will be taken to be constant across the plasma volume for the sake of simplicity. $\Omega \in \mathbb{R}$ is a function of (α, q) and $\theta_k = k_q/k_\alpha$; it is the wave frequency in the absence of FLR effects.

The semiclassical formalism uses a short wavelength ordering to analyse the propagation of wavefronts travelling at the group velocity in an inhomogeneous system. The trajectory in the phase space which describes the position and central wavelength of the wavefront as a function of time is known as a ray, and is governed by the ray equations:

$$\dot{\alpha} = \frac{\partial D}{\partial k_\alpha} = \omega \Omega_i - \frac{\theta_k}{k_\alpha} \frac{d(\Omega^2)}{d\theta_k} \quad (158)$$

$$\dot{q} = \frac{\partial D}{\partial k_q} = \frac{1}{k_\alpha} \frac{d(\Omega^2)}{d\theta_k} \quad (159)$$

$$\dot{k}_\alpha = -\frac{\partial D}{\partial \alpha} = -\frac{d(\Omega^2)}{d\alpha} \quad (160)$$

$$\dot{k}_q = -\frac{\partial D}{\partial q} = -\frac{d(\Omega^2)}{dq} \quad (161)$$

with $\theta_k = k_q/k_\alpha$. These differential equations are equivalent to those of a Hamiltonian system given by $H = \omega$, and consequently it is clear that the frequency of our wavefront is conserved if the dispersion relation is time-independent.

An important feature of these equations is that there is a scaling transformation $(k_\alpha, k_q, \alpha, \Omega_i, q) \rightarrow (sk_\alpha, sk_q, \alpha, \Omega_i/s, q)$ which conserves the ray trajectories up to a time reparameterisation $\tau \rightarrow s\tau$. The phase along these rays also scales with s , which we choose to equal Ω_i for the purposes of explicit ray tracing. The structure of the dynamics is independent of this scaling, which considerably simplifies the semiclassical analysis, and makes it reasonably straightforward to find mode spectra in Ω_i . In this kinetically stabilised theory, the parameter Ω_i will play an equivalent role to that of \hbar in quantum mechanics.

There are several practical complications to applying the semiclassical formulation to our ballooning system. One of these is the lack, in general, of integrability of the system. The other problem is that the frequency of the wavemode may not be real. In this case we have the partial derivatives of ω being in general complex. The dispersion relation has a quadratic dependence with ω , and real solutions are found when the coefficients of ω satisfy $(k_\alpha \Omega_i)^2 + 4\Omega^2 > 0$. Complex frequencies are possible for local modes which are ideal MHD unstable and have small enough wavenumber k_α . The semiclassical formalism can be extended to complex phase space for one dimensional cases, but the extension to higher dimensional models is less obvious. We circumvent this analysis by considering only the modes with real frequency and using the disappearance of these modes as an indication of the existence of modes with complex frequency. This is illustrated by figure 38. Growth rates of slightly unstable complex modes can be found if needed by analytical continuation of

the mode frequency.

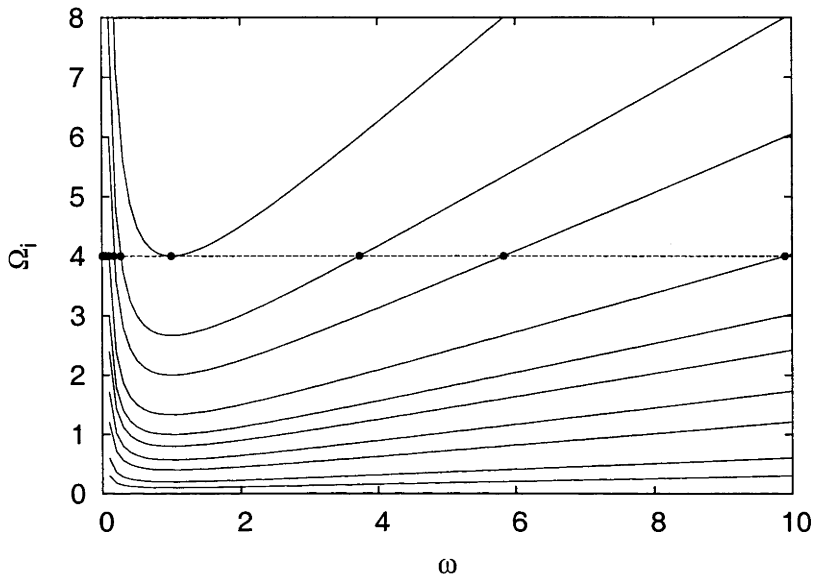


Figure 38: A schematic view of the spectrum of modes in terms of the frequency ω and the drift stabilisation parameter Ω_i . The spectrum of mode frequencies for a particular value of Ω_i is given by the intersections of the solid lines with a dashed horizontal line, with points at the eigenfrequencies. For $\Omega_i < 4$, modes disappear from the real spectrum in pairs as the stabilisation effect is reduced. This value corresponds to marginal stability.

The most unstable modes of this model are strongly spatially localised in the most unstable region, but have wavelengths as large as possible to reduce the stabilisation effect at small wavelength; their spatial extent is usually of the order of the mean wavelength in some directions. For this reason, semiclassical analysis, which is derived in the limit where the wavelength is much smaller than any other spatial variation, is not rigorously justifiable. However, it is generally found that the semiclassical quantisation of systems gives surprisingly good results even where the wavelength is of the order of the other scale lengths. For example, in both [58] and [21], the error even for the first eigenmode is within a few percent of the average spacing between eigenvalues. For this reason it is reasonable to expect that the marginal stability point with respect to varying diamagnetic drift frequency Ω_i as given by our semiclassical analysis will be considerably more accurate than an order of magnitude guess. A precise reproduction of the theoretical marginal stability point is unlikely to occur in an experiment, and one would be more interested in determining the nature of the drift stabilised modes, and obtaining a good estimate for the marginal stability

β value.

8.8 An application of the semiclassical theory to the H-1 stellarator

The H-1NF heliac is one of several stellarators which are not amenable to toroidally averaged calculations due to their strong helicity. There are several classes of ideal MHD ballooning modes which may exist in H-1NF equilibria, according to their toroidal and poloidal localisation: we consider the most unstable and most localised class of modes of the H-1NF equilibrium studied in [16], which has $\beta \simeq 1\%$, and a somewhat peaked pressure profile. These modes are localised toroidally, poloidally and radially, so that their amplitudes are strongest around a point inside the plasma on the outboard side of the magnetic axis. The primary object of our investigation is to find the marginal stability criterion, or, equivalently, the frequency of the most unstable mode. The value of β is chosen so that the ideal MHD unstable ballooning regions are localised toroidally, but occupy a substantial fraction of a field period. This is an interesting case because the constant Ω^2 surfaces of ideal MHD instability, while topologically spherical, are strongly shaped near marginal stability, and the marginally stable modes propagate in a reasonably large volume of the plasma: such moderate scale instabilities are believed to be the most likely candidate for a stability limit in stellarators. The limiting case, where the region of ballooning instability becomes very small, is also of interest because it corresponds to the marginal stability limit for $\Omega_i \rightarrow 0$.

To begin the analysis, we determine the ideal MHD local ballooning dispersion relation by integrating the ballooning equations along the field lines of the finite-beta computed equilibrium. For this case, the region of interest is in the neighbourhood of the most unstable spatial position. The dispersion relation is calculated on an evenly spaced grid in (α, q, θ_k) , and then a low-order polynomial fit is found which is accurate around the most unstable point in the plasma. This provides a fast evaluation of the dispersion relation, and consequently an efficient solution to the ray equations.

In [16], chaotic ballooning orbits are found in the ideal MHD limit, with an artificial wavelength cutoff, which is intended as a simple model for some FLR stabilisation effect, or the effect of finite numerical resolution in an Ideal MHD stability code. We would expect that using a more physical drift stabilisation term instead of this cutoff would lead to qualitatively similar results: however, there is a sense in which the physical drift stabilisation is smoother, and this tends to suppress the ray chaos slightly. In fact, we find that this substitution leads to almost integrable ray orbits in the equilibrium considered in [16]. A

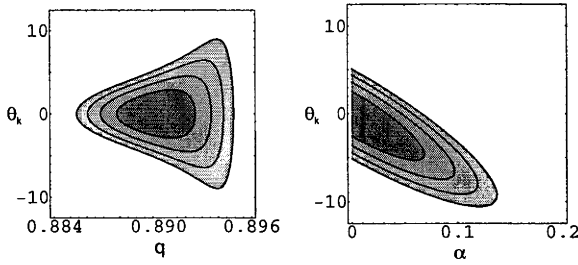


Figure 39: Contours of the ideal MHD instability value in phase space, with darker shades of gray indicating increasing instability. These topologically spherical surfaces in (θ_k, α, q) space surround the most unstable position of the plasma.

typical ray orbit for this case is displayed in figure 42.

To access the regime where the ray equations lead to chaos, we allow some of the parameters in the polynomial form of our dispersion relation to vary. We do not relate this directly to the variation of an experimental control parameter: a more complete study would determine the dispersion relation throughout the configuration space of H-1NF. Instead, we consider the generalised dispersion relation to be typical of ballooning stability about the most unstable point in a strongly shaped plasma. The new dispersion relation $\omega(\theta_k, \alpha, q)' = \omega(\theta_k/c, \alpha, q)$, allows us to control the sensitivity to the position of the mode along the field line. In the integrable case, the ratio of the two timescales is approximately proportional to c , so that we expect the separation of timescales to break down for some c .

We examine values of $c \in [1, 4]$, permitting ray orbits which display chaotic, mixed and integrable behaviour. In particular, we integrate the ray equations for the values $c = 1, 1.5, 2, 2.5, 3$ and 4 , using standard numerical techniques. Because the rays propagate on a three-dimensional surface, they are difficult to visualise, and it is more useful to consider the Poincaré plots generated by the intersections of these rays with a surface. In order to visualise this Poincaré surface, we map it into the 2-D plane of the plot with a one-to-one function, so that distinct features do not overlap. The Poincaré punctures of rays on KAM surfaces lie on curves, whereas those in the ergodic region fill an area of the plane as they propagate. Figure 40 shows the intersections of the rays with the surface $\alpha = 0$, demonstrating the transition between the case where almost all the phase space is occupied by KAM tori ($c = 1$), and the case where only a few small remnant tori are present ($c = 4$). This transition is typical of a Hamiltonian system with an incomplete set of conserved quantities, where the

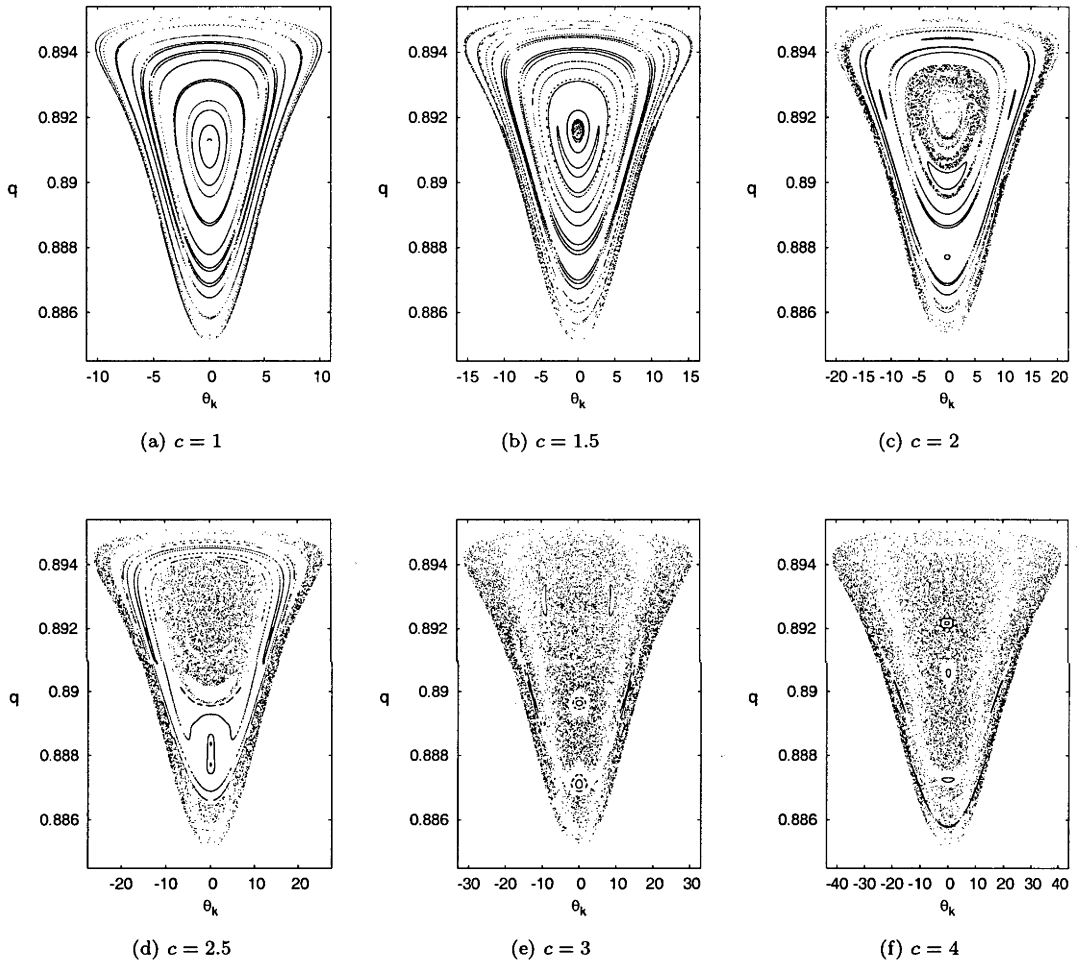


Figure 40: Intersections of semiclassical rays with the surface $\alpha = 0$ for several values of the scaling function c . These rays propagate on the surface $\omega^2 = -\Omega_{\min}^2$.

phase space generally consists of a mixture of nested tori and stochastic regions: a homoclinic web. The example familiar to those working with stellarators is their vacuum magnetic field structure: even when magnetic islands have been considered in the design, small remnant islands inevitably exist, with regions of stochastic field between. Likewise, in any region of stochastic magnetic field, there are small regions of order.

In the almost-integrable case $c = 1$, there is only a very small chaotic region of phase space, due to the existence of a separation of timescales, as in [14]. Quantisation can be achieved by finding the two action integrals on the KAM tori, although because of the separation of scales, it is a reasonable approximation to consider only one of the integrals.

In the mixed case, where there is no large separation of timescales, this approach fails. However, it is possible to analyse these near-integrable systems in the semiclassical approach, and we demonstrate a quantisation for the case where $c = 2$ and half the phase space is ergodic. The chaotic motion here can be thought of as a diffusive motion across the phase space, rather than a fast mixing of the trajectories: this is the kind of chaos present in stellarator magnetic fields just outside the last closed flux surface.

For the almost completely ergodic case, the structure of the dynamics becomes more complicated, and can no longer be approximately separated into two separate oscillations. We therefore do not attempt to extend the previous analysis to this case. Also, because there are remnant KAM surfaces even in the case where $c = 4$, we would expect the structure of the spectrum to deviate from the predictions of random matrix theory somewhat, which is only rigorously applicable in the case where the whole phase space is ergodic. Nevertheless, the Weyl estimate for the first unstable mode, as described in section 8.11, should still be reasonable in this limit where there is not a strong separation of timescales.

8.9 The topology of the Lagrangian surfaces

In the integrable case the Lagrangian surfaces of our semiclassical system are qualitatively similar to the torus shown in figure 41. The two loops $C1$ and $C2$ shown there can be used to quantise any such surface, leading to two quantisation conditions,

$$\int_{C1} \mathbf{p} \cdot d\mathbf{q} = 2\pi I_1 = 2\pi\hbar \left(n_1 + \frac{\mu_1}{4} \right) \quad \text{and} \quad \int_{C2} \mathbf{p} \cdot d\mathbf{q} = 2\pi I_2 = 2\pi\hbar \left(n_2 + \frac{\mu_2}{4} \right) \quad (162)$$

The two Maslov indices μ_1 and μ_2 arise because the projection onto configuration space shown there is multivalued, and it is necessary to determine matching

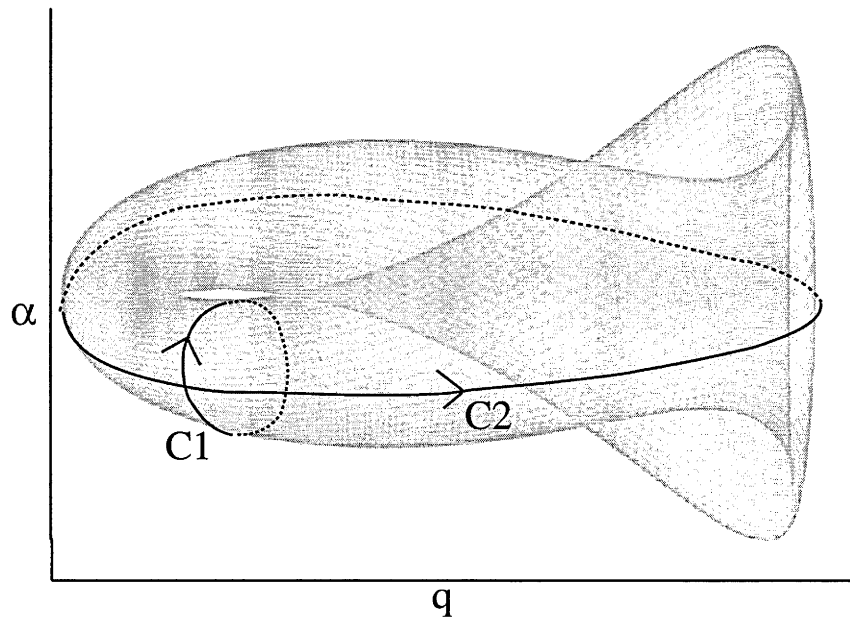


Figure 41: The Lagrangian surface associated with an integrable semiclassical ray of our model ballooning system with $c = 2$, projected onto configuration space. Two topologically distinct irreducible loops C_1 and C_2 are shown on the surface: any other loop can be generated by tracing a curve around M_1 loops of C_1 and/or M_2 loops of C_2 , and then deforming the curve on the Lagrangian surface.

criteria between the various sheets of this projection. They can be determined by counting the number of caustics which the irreducible loops cross. For this case the loops both have two crossings with positive sign so that $\mu_1 = \mu_2 = 2$.

8.10 The integrable case

Estimates for typical values of the phase integrals I_1 and I_2 can be given simply by considering the shape of constant ω surfaces in phase space, and finding the area of the projections onto the (α, k_α) plane and the (q, k_q) plane for I_1 and I_2 respectively, because the motion effectively separates in these directions, as can be seen in typical ray orbits like those of figure 42. A rough estimate is

$$I_1 \simeq \alpha^* k_\alpha^* \simeq \frac{2\alpha^* \omega}{\Omega_i} \quad \text{and} \quad (163)$$

$$I_2 \simeq q^* k_q^* \simeq \frac{2q^* \theta_k^* \omega}{\Omega_i} \quad (164)$$

where the starred quantities give an estimate of the size of the constant ω surface in that direction. Because these surfaces are roughly spherical in θ_k, q and α , the starred quantities θ_k^*, q^* and α^* go to zero with the same power near the most unstable point in the plasma, and $I_2/I_1 \rightarrow 0$ because I_2 involves a product of two quantities (as noted by [14]); consequently, the ray orbits will be integrable there. The ratio I_2/I_1 also approaches zero in the axisymmetric limit where the toroidal variation in $\omega \rightarrow 0$.

This quantisation problem was solved approximately for an integrable case in [14] by finding a KAM surface where the action integral (I_2) associated with the fast timescale is equal to π . The maximum value of I_2 on the constant energy surfaces occurs on the degenerate KAM torus that the others nest around. The other action, I_1 , varies much more quickly than I_2 on the energy surface, so there is a torus near this degenerate torus which has both I_1 and I_2 quantised for some values of ω_i , and which has approximately the same I_2 as the degenerate torus. It is practicable to quantise both I_1 and I_2 (especially since computational issues are now less of a restriction than in [14]), but as this should have only a small effect on the marginal stability condition, we only explicitly quantise the mixed case, where these effects are more important. For the full quantisation, marginal stability occurs where

$$\frac{\partial}{\partial \omega} \Omega_i = 0. \quad (165)$$

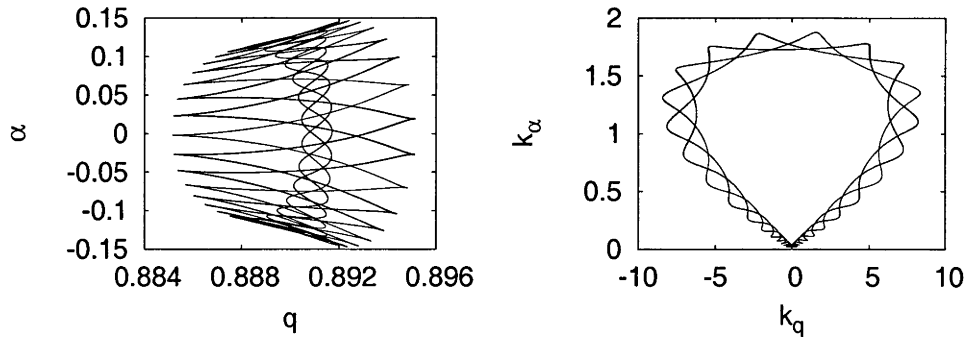


Figure 42: A semiclassical ray trajectory traversing a KAM torus for the H-1 ballooning model with $c = 1$. Two distinct motions are obvious corresponding to a fast and slow traversal of the torus respectively.

8.11 Box quantisation and the Weyl formula

The Weyl formula gives an asymptotic estimate for the number of quantised modes below some frequency ω based on the volume of phase space enclosed by the constant ω contour:

$$N_{\text{Weyl}}(\omega) = \frac{1}{(2\pi)^n} \int dx^n dk^n. \quad (166)$$

It is illustrative to consider its application to the quantisation of a particle in a two-dimensional box. For this case we have the frequency $\omega = \sqrt{k_x^2 + k_y^2}$, where k_x and k_y are the two wavenumbers; and to satisfy the boundary conditions we require that $k_x = \pi(2n - 1)/x$ and $k_y = \pi(2m - 1)/y$ for integers m and n , where x and y are the length and width of the box. The volume of phase space enclosed by a constant ω contour is $\pi xyE/4$.

We consider two differently shaped boxes with (x, y) set to $(0.5, 0.4)$ and $(0.1, 2)$ respectively. The staircase function given by the number of modes with $\omega_i < \omega$ is plotted for each case together with the Weyl estimate. We can see that the staircase function for the nearly square box follows the Weyl asymptotic formula closely, whereas the long, thin box has significant departures from the asymptotic result in this frequency range.

We are mainly interested in the lowest quantised frequency; if the spectrum conforms well to the Weyl formula then a simple estimate for this frequency can be found by requiring $N_{\text{Weyl}} = 1/2$, and in this case the estimate would be $\omega_1 = 1.26$. This is a fairly good estimate for the nearly square box where $\omega_1 = 1.01$, but fairly poor for the thin box, where $\omega_1 = 9.89$. A good estimate

for the lowest eigenmode of the thin box is given by considering quantisation of the short direction only.

If we were to consider the spectrum of a system which exhibits hard semiclassical chaos (all the periodic orbits of such a system are hyperbolically unstable) we would expect to see even smaller deviations from the Weyl spectrum than for our nearly square box. In this regime quantum chaos theory is applicable, and governs the departures from the average level density given by the Weyl formula $\rho(\omega)$. One relevant quantity which can be derived is the probability distribution for the extremal eigenvalue ω_{\min} ; this allows us to determine whether the system is likely to exhibit unstable modes. This probability is approximately Gaussian and the mean is at $N_{\text{Weyl}} = 1/2$, so that the Weyl formula should also give a good estimate for the frequency of the most unstable mode in this case.

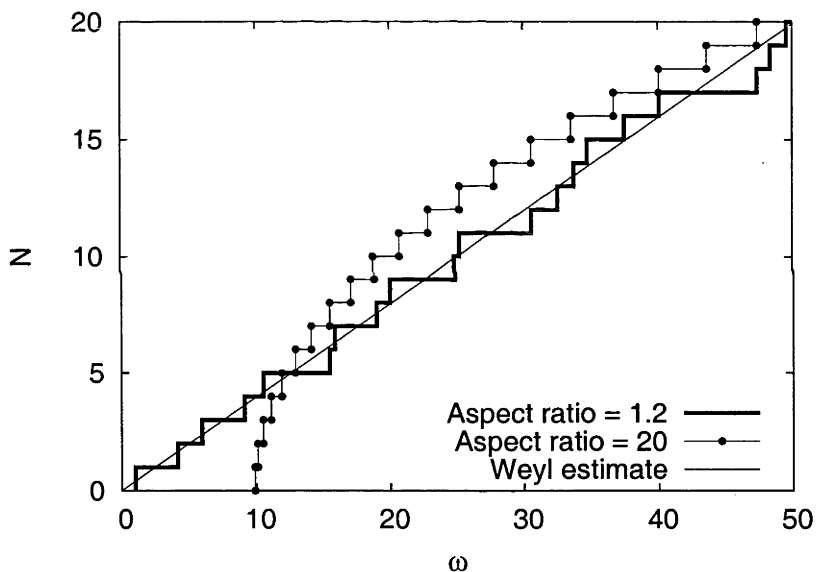


Figure 43: The number of quantised states below a frequency ω for particles in a rectangular box. This is compared with the Weyl estimate for the integrated density of states.

Thus the only situation in which the Weyl formula is likely to give a poor estimate for the lowest frequency mode is where there is a significant timescale separation; and in this limit semiclassical quantisation is easy to apply.

8.12 Applying the Weyl formula to drift stabilised ballooning modes

In the ergodic case, the Weyl estimate of the number of unstable modes should be very close to the true number of unstable modes, as a consequence of the strong level repulsion found in physical systems, and modelled random matrix theory. An approximate condition for marginal stability is then given by requiring that the estimated number of unstable modes be 1/2. This would not have been an appropriate estimate for a case with a separation of timescales where 'level clustering' in the spectrum must be taken into account.

It is first necessary to show that the Weyl formula is applicable even where the dispersion relation is complex in some of the phase space. The simplest way to demonstrate this is to consider the spectrum not with respect to the frequency ω , but with respect to the drift stabilisation parameter Ω_i . The reason is that the relevant dispersion relation, $E = \Omega_i(\omega, \theta, k_\alpha, \alpha, q)$ is real for real $(\theta, k_\alpha, \alpha, q)$, as can be demonstrated by solving equation (157).

The Weyl estimate for the number of modes in the spectrum of Ω_i above Ω_{i0} is then the volume of phase space enclosed by the contours $\Omega_i = \infty$, $\Omega_i = \Omega_{i0}$:

$$N_{\text{Weyl}} = \frac{1}{4\pi^2} \int H(k_\alpha^{\text{max}} - k_\alpha) dV \quad (167)$$

where

$$k_\alpha^{\text{max}} = \frac{1}{\Omega_{i0}} \left(\frac{\Omega^2(\alpha, q, \theta)}{\omega} - \omega \right). \quad (168)$$

Proceeding with the integration we have

$$N_{\text{Weyl}} = \frac{1}{4\pi^2} \int_S \frac{(k_\alpha^{\text{max}})^2}{2} d\theta d\alpha dq \quad (169)$$

$$= \frac{1}{4\pi^2 \Omega_i^2} \int_S \frac{1}{2} \left(\omega - \frac{\Omega^2(\theta, q, \alpha)}{\omega} \right)^2 d\theta d\alpha dq \quad (170)$$

$$= \frac{1}{4\pi^2 \Omega_i^2} cV(\omega), \quad (171)$$

where the volume S is all (q, α, θ) for which $0 < \Omega^2(\theta, q, \alpha) < -\omega$, and we have defined a normalised volume $V(\omega)$. The highest quantised value of Ω_i is approximated by setting $N_{\text{Weyl}} \simeq 1/2$, and therefore

$$\Omega_i = (cV(\omega)/(2\pi^2))^{\frac{1}{2}} \quad (172)$$

for this mode. The marginal stability condition is then found by requiring

$$0 = \frac{\partial \Omega_i}{\partial \omega} = \frac{\partial V}{\partial \omega}. \quad (173)$$

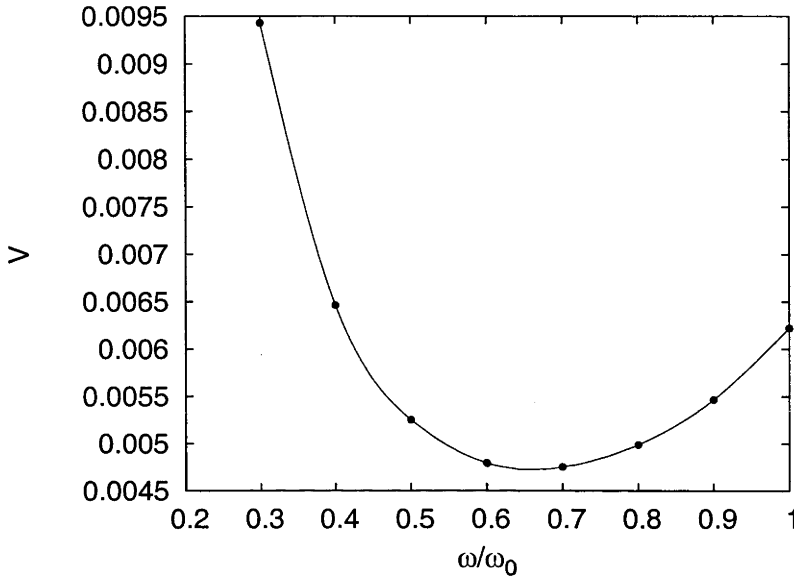


Figure 44: The volume of phase space enclosed by the constant ω surface for $\Omega_i = 1$ and $c = 1$ as a function of ω/ω_0 . $\omega_0^2 = -\Omega_{i\min}^2$.

For our dispersion relation the values of the volume V are plotted in figure 44. Marginal stability is associated with the minimum phase space volume as a function of ω , $V = 0.00473$. Substituting this volume into equation (172) yields the marginal stability condition $\Omega_i = 0.0155c^{1/2}$.

8.13 A quantisation of the mixed regime

It has recently been shown [58] that it is possible to accurately determine semiclassical spectra even in systems which have near-integrable or mixed regular chaotic dynamics. Extensions of the Berry–Tabor formula [68] to near integrable systems [65] have allowed the systematic determination of effects of the breakup of KAM surfaces on the quantum spectrum. This leads to a very simple criterion for determining how much our spectrum will differ from the spectrum of a nearby integrable wave equation; the criterion can be expressed in terms of the difference in action between the pairs of orbits which survive the breakup of KAM tori.

For our model with $c = 2$ we are well into the mixed regime of behaviour, where almost half of the phase space is traced out by ergodic orbits. For this parameter regime, it is still possible to describe the dynamics in most of the phase space in terms of two more or less separate oscillations, even well into the ergodic region. It is therefore reasonable to consider this system as a perturbation to a nearby integrable system. Rather than explicitly finding this nearby system, we proceed based on knowledge of quantities calculated on periodic orbits in the phase space, as in [58].

In an integrable two-dimensional system, the conserved frequency, ω can be expressed in terms of the two independent actions on the KAM tori, I_1 and I_2 , as $\omega = H(I_1, I_2)$. The actions are associated with loop integrals around the two independent angles on the corresponding tori, which can be rather difficult to construct for integrable systems; such tori are difficult to even define in the chaotic region of a near-integrable system. In order to calculate the actions of these tori in our mixed system, we use the method of [66] to find the inverse of ω , the function $g_E(I_1) = I_2$, by considering the parameters of the pairs of periodic orbits which survive the destruction of a resonant torus M . The relevant primitive periodic orbits [stable (s) and hyperbolic unstable (h)] are specified by the winding numbers M_1 and M_2 , and their parameters are related to the function g_E via

$$g'' = \frac{2}{\pi M_2^3 \Delta s} \left[\frac{1}{\sqrt{\det(D_s - 1)}} + \frac{1}{\sqrt{-\det(D_h - 1)}} \right]^{-2}, \quad (174)$$

with

$$\Delta s = \frac{1}{2}(s_h - s_s) \quad (175)$$

the difference between the scaled actions, and D_s and D_h the monodromy matrices of the two orbits. Equation (174) becomes exact in the limit of an integrable system.

We also follow [58] in applying equation (174) deep into the chaotic regime where there are no stable orbits. Here, the remnants of the broken tori are present as a pair of unstable orbits, one hyperbolic and one inverse hyperbolic. This is a natural extension, and is justified in part by the accuracy of the quantisation in [58]. However, we depart from [58] in that we apply a simple EBK quantisation, rather than considering the Berry–Tabor formula, as the two formalisms are equivalent, and for our purposes the EBK quantisation is more straightforward.

The action of each orbit $s = M_1 I_1 + M_2 I_2$ and the quantity g'' are used to find the actions I_1 and I_2 . We have the winding number $q = M_2/M_1 = -\partial I_1/\partial I_2$

M_1	M_2	\bar{s}	Δs	$\det(D_h - 1)$	$\det(D_s - 1)$
3	10	0.93032	3.53 10^{-7}	-0.008356	0.008351
2	7	0.645361	8.943 10^{-6}	-0.053907	0.058636
1	4	0.352544	2.0241 10^{-3}	-2.173502	1.825331
1	5	0.385912	6.6934 10^{-4}	-0.870845	2.156580
1	6	0.399885	1.2069 10^{-3}	-8.503382	4.471618
1	7	0.405856	0.5088 10^{-4}	-3.831766	9.653869
1	8	0.408461	4.8473 10^{-4}	-18.73693	8.659744

Table 2: Parameters for several pairs of periodic orbits which are remnants of KAM tori. The orbits are specified by their winding numbers M_1 and M_2 in each direction around the torus; for each pair of orbits the mean action $\bar{s} = (s_1 + s_2)/2$, the difference in action $\Delta s = s_1 - s_2$ and the stability determinants $\det(D_h - 1)$ and $\det(D_s - 1)$ are tabulated.

from the conservation of action, implying that

$$g'' = \frac{\partial^2 I_2(I_1, E)}{\partial I_1^2} = \frac{\partial q}{\partial I_1} \frac{\partial}{\partial q} \left(\frac{\partial I_2}{\partial I_1} \right) = \frac{\partial q}{\partial I_1} \frac{1}{q^2}. \quad (176)$$

We can then solve for I_1 and I_2

$$I_1(q) = \int_{q_0}^q dq \frac{1}{q^2 g''}, \quad I_2(q) = \frac{s - M_1 I_1(q)}{M_2} \quad (177)$$

since $I_1(q_0) = 0$ for our tori.

The main numerical task is the determination of a representative set of periodic orbits and their associated actions, winding numbers and monodromy matrices. Because of the (stellarator) symmetry $\omega(\theta, x_\alpha) \rightarrow \omega(-\theta, -x_\alpha)$, a large number of the periodic orbits intersect the line $(\theta, x_\alpha) = (0, 0)$ (in particular, those for which $M_2 = 1$), simplifying the search for periodic orbits considerably. In the integrable region of phase space it is possible to find periodic orbits by seeking rational values of the winding number, and visually inspecting the structure of the broken tori. The fixed points can then be iteratively refined. Because we need to find only a small number of relatively short closed orbits, this simple approach is sufficient, unlike, for example, in the evaluation of Gutzwiller's trace formula, where it is often necessary to find a very large number of long closed orbits using sophisticated techniques.

Relatively high numerical accuracy is necessary for some of the calculations, especially for the calculation of the phase difference of the 10/3 resonant fixed points, which is smaller by seven orders of magnitude than the average phase. The fourth order Runge–Kutta algorithm we used is fast enough to produce these results interactively to the precision indicated by the number of significant figures shown.

The difference between the phases of the two remnant orbits Δs is very small ($< 2 \cdot 10^{-3}$) for all the orbits we have considered here. A complete analysis would consider the effects of these phase shifts on the semiclassical quantisation by using the extension of the Berry–Tabor formula to near integrable systems. However, as pointed out in [58]:

For small phase shifts the extension of the Berry–Tabor formula to near-integrable systems ... seems not to affect the *frequencies*, i.e. the semiclassical eigenvalues ω_k ..

In their case, even without considering the corrections due to broken tori, their quantisation is accurate to within a few percent for most of the mode frequencies. The maximum phase splitting in [58] is $\omega\Delta s = 0.44$; the phase splitting of the periodic orbits considered here is no larger than than 0.04 for the frequency of most interest (the first semiclassical frequency), which should be inconsequential.

We therefore proceed with our simple quantisation, and determine the quantity g'' on each of the orbits using equation (176). g'' and s/M_2 are smooth functions of winding number, and we interpolate between these data points with a cubic spline to calculate the approximate values of the two functions in the full range of winding numbers, which are plotted in figure 8.13. We then integrate to obtain the actions I_1 and I_2 .

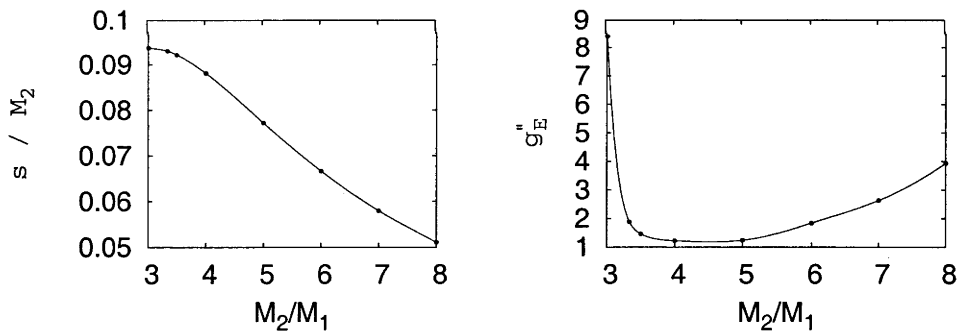


Figure 45: The orbit action per ‘toroidal’ rotation (left) and the quantity g'' (right) as a function of winding number. The data points represent the values calculated on periodic orbits; the smooth curve is a spline fit of this data. The scaling parameter $\Omega_i = 1$.

The quantisation is completed by requiring that the actions $I_1 = (2n_1 - 1)\pi$ and $I_2 = (2n_2 - 1)\pi$. The mode with the lowest frequency has $n_1 = n_2 = 0$ and $I_1/I_2 = 1$, and occurs at $q = M_2/M_1 = 4.45$ with scaled phase $s = 0.0682$.

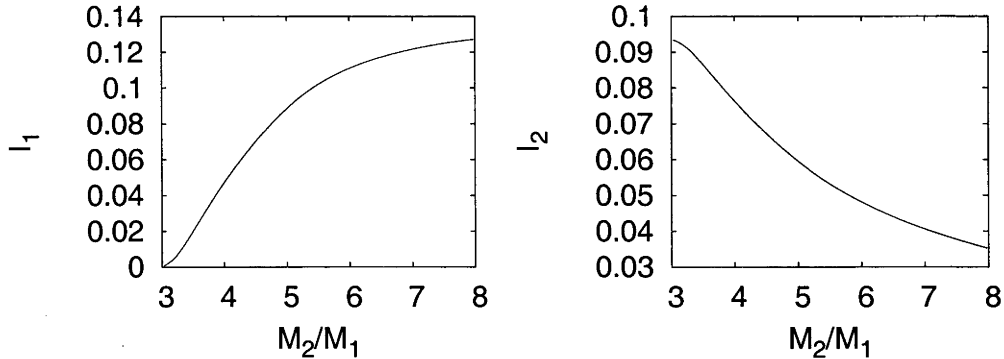


Figure 46: Actions I_1 (left) and I_2 (right) as a function of the winding number. The scaling parameter $\Omega_i = 1$.

The quantised value of the scaling parameter must satisfy $s/\Omega_i = \pi/2$, so $\Omega_i = 0.04342$. The Weyl estimate for the scaling parameter is given by equation (173): for $\omega = \omega_0$ and $c = 2$ we find $\Omega_i = 0.0247$. The Weyl estimate is significantly different from that given by the EBK quantisation, but is still gives a rough guide to the magnitude of this drift stabilisation.

8.14 Conclusions

Strongly localised ballooning modes are often the first instabilities to become evident in a stellarator. In the ideal MHD limit, we expect the plasma to become unstable as soon as the local stability analysis indicates a negative Ω^2 anywhere, but the localised unstable modes predicted by the theory are very singular, and it is not clear how to proceed with quantisation. Instead, we have considered a drift-stabilised model, and approached the ideal MHD limit by setting $\Omega_i \rightarrow 0$.

We have demonstrated that fairly straightforward semiclassical quantisation can be applied to this system even when half of the phase space is ergodic. Interestingly, the ray chaos does not play any significant role in the quantisation of the first few modes. In fact, the qualitative results could all have been obtained from a simple two time-period analysis. The difficulty here was to extract the regular behaviour of the system from the chaotic corrections: we utilised a technique based on quantities on periodic orbits. It is possible that chaos may be important for stable plasma waves which feel the details of the equilibrium more strongly, but that would be the subject of a separate study.

Even the cases with $c > 2$, which have almost their entire phase space ergodic, are not truly examples of ‘hard chaos’, as there are still stable fixed

points and nested tori present in the phase space. This is typical of physical systems; the examples of systems with rigorous hard chaos are few and far between. It is therefore not necessarily appropriate (and certainly not easy) to apply Gutzwiller's trace formula to quantise these systems. However, because there is no strong separation of timescales in these systems, we can be confident that the Weyl formula will give a reasonable estimate for the first unstable mode, and we have demonstrated how this can be applied.

None of these semiclassical techniques can be expected to be precisely accurate for the most unstable modes, which typically have wavelength approximately equal to the scale length of the regions they propagate in. However, they should give good estimates of the approximate amount of drift stabilisation to be expected, and the approximate values of β where the instability should set in. Qualitatively, the result is as expected: configurations with small regions of ballooning instability with low growth rate are expected to be strongly stabilised by these drift effects. The effects of toroidal localisation will be important when $I_2 \gtrsim I_1$ which according to equation (164) occurs when $q^* \theta_k^* \gtrsim 2\alpha^*$. In this case, I_1 is the more difficult quantisation condition to satisfy, and will control the value of drift stabilisation required for marginal stability. In the original H-1NF model we found $I_1 \simeq 2I_2$ for frequencies near marginally stability so the effects of toroidal localisation were of similar importance to the effects of poloidal localisation: this will also be true for other strongly shaped configurations. Modes which are not toroidally localised have an effective $\alpha^* \simeq 2\pi$ compared with $\alpha^* \lesssim 2\pi/(\# \text{ of field periods})$ for localised modes, so that this toroidal quantisation is much more difficult to satisfy for toroidally localised modes, even if they can propagate over most of a field period. As a consequence the first modes to become unstable may be marginally toroidally localised, and will be somewhat difficult to deal with in semiclassical analysis.

9 Conclusions

9.1 A Review

Although the goal of the thesis was an exploration of the physics of strongly three dimensional plasmas, and stellarators in particular, the path of investigations led us through the realms of general plasma physics. In particular, it was necessary to understand how the spectrum of the models being solved was related to that of the actual plasma, and how to use the eigenspectrum to gain insight into the dynamics of physical systems. Such spectra are very powerful tools in most areas of physics, and it is natural to examine the eigenvalue spectra of plasma fluids. However, in ideal and extended MHD models, the relationship of such spectra to the actual plasma behaviour is not always obvious. This is because the eigenmodes of these models are strongly non-normal and the dynamics are often dominated by the interference between these modes, rather than by the individual eigenmodes themselves. We believe concepts like transient behaviour and the pseudospectrum, which were explored in our literature survey, provide a useful link between spectral analysis of plasmas and the initial value problem.

Next, we considered the relationship between the spectra of compressible and incompressible MHD models; demonstrating the qualitative differences between the spectra of these models and explaining the origin of the modes in the spectra through local wave theory and the WKB method. This study was motivated by the need to interpret the results of an incompressible resistive spectral code, and to establish what physical meaning could be assigned to the various eigenmodes. We have demonstrated that in the relevant incompressible limit (where the ratio of specific heats is artificially set to ∞) most of the modes of the cylindrical spectrum bear no direct resemblance to the more physical compressible eigenmodes. This conclusion is not limited to the strongly damped modes, as there are physically spurious weakly damped modes introduced by this particular incompressibility assumption. We expect that a code which formulates incompressibility in this way may still be useful for finding the marginal stability points to non-oscillatory modes, which is the usual purpose of a linear code; it would also be appropriate if there was a need to model conductive fluids which are truly incompressible (like plasmas with $\beta \gg 1$, or conductive liquids). Other ways of introducing incompressibility to the plasma model, like setting the parallel inertia of the plasma to zero, allow for better access to physical plasma modelling, but we have not examined how such a scheme might be implemented in a fully 3D stellarator code.

We were then in a position to consider numerical approaches to three-

dimensional resistive MHD. A flexible formulation was chosen in order to address problems of spectral pollution which have caused difficulty in many numerical approaches to MHD, and which had become apparent in an incompressible formulation of our resistive MHD spectral code. A compressible model was chosen to resolve as much of the physics as possible, and avoid the spurious modes seen in the most straightforward incompressible formulation. We then demonstrated that our new implementation of the code was able to reproduce the instabilities and growth rates found in earlier analyses, and did not suffer from spectral pollution. Next, we looked at cases not explored by earlier studies, which could not resolve the full three-dimensional geometry and the plasma compressibility. First we considered ideal and resistive modes in relatively large-aspect ratio stellarators, where toroidal effects are not strongly important, and reproduce the expected instabilities and the associated compressible growth rates. We also considered a case with strongly toroidally localised instabilities, where codes based on toroidal averaging of the equilibrium are inapplicable: we resolved a toroidally localised resistive instability for a tokamak with strong mirror terms.

In the last section of the plasma we explained how to use semiclassical analysis to determine marginal stability limits for drift stabilised MHD in stellarators. We determined a variational form for the problem, implying the presence of a wave action, and providing a justification for the use of the standard techniques of semiclassical quantisation in this problem. We explain the conditions under which the semiclassical analysis is near-integrable and separates into two separate timescales, and then consider cases in which the semiclassical rays are chaotic. The semiclassical analysis in the presence of chaos involved the use of some recently discovered techniques; with these tools we were able to quantise the system in a significantly non-integrable case, where approximately half the phase space was ergodic. The most strongly chaotic cases are difficult to quantise exactly, but in these cases the Weyl estimate can be used to provide an indication of the expected marginal stability boundary.

We hope that the codes and techniques described in the thesis will find further application to existing stellarator configurations and design studies (the author of the thesis considered the design of stellarator vacuum magnetic fields in [69] and [70], rather than the stability issues explored in the thesis).

9.2 On the use of linear eigenspectra

The growth rates and global structure of unstable eigenmodes are important in practice because they have been found to give useful information about how an instability will affect the plasma, and whether it will be significant for confinement. Such questions can also in principle be addressed by more complete

models, which include the neglected fluid effects, and the nonlinearity of the plasma.

For the stable spectrum, the situation is slightly more complex: the naïve interpretation of the resistive MHD spectrum based on an analogy with the spectrum of Hermitian systems, like quantum mechanics, is misleading. We believe that an analysis based on resonances or pseudospectral theory could be used to extract information about the behaviour of the plasma at different timescales; such models can consider the effects of the isolated oscillatory modes along with those of the continua. It would be possible for instance to make a comparison between the MHD activity seen experimentally and the degree of resonance predicted numerically for a relevant set of perturbing forcings.

The spectrum of linear modes often serves as the zeroth order model for nonlinear studies of plasma, particularly in the weak turbulence approach. In weak turbulence theory, the state of the system can be expressed via the spectrum of wave amplitudes at different length scales; the spatial structure of the plasma is usually not considered. The nonlinear coupling then provides a mechanism for coupling between different scale lengths. The availability of a linear mechanism to transport wave energy from short to long wavelength and back again may be particularly significant for the study of turbulence in these three-dimensional systems; the means for decorrelation of wavepackets through quantum chaos may also be of relevance. Resonances (or pseudomodes) may be more relevant than eigenmodes for nonlinear analysis, because the short decorrelation time and relatively strong forcing often mean that the linear behaviour as $t \rightarrow \infty$ is not explored.

9.3 On further application and enhancement of Spector3D

The determination of stellarator stability is a very mature field, and there are well understood and fairly comprehensive analytical criteria for the classification of equilibria as either stable or unstable. Certain problems still require numerical methods in order to find an accurate boundary of stability, however, especially when models beyond ideal MHD are considered.

We believe that Spector3D in its present form is very useful for the study of global resistive modes: it allows the calculation of physical growth rates for such modes, and a determination of their structure. In particular, we expect that it will allow further study of tearing modes in three dimensional plasmas, which can be difficult to handle analytically, especially where they appear in pairs, or in conjunction with other instabilities. The code could be reasonably easily extended to include other fluid effects, like FLR stabilisation.

In order to be able to address stability for high mode number instabilities

in strongly three dimensional geometries, it will be necessary to represent a much larger number of Fourier coefficients in the perturbation than we have considered here. The practical limit is currently about 50 mode pairs, but in ideal MHD analysis a somewhat larger number of mode pairs is required to accurately resolve the growth rate; for example, for a TERPSICHORE test case [71] with limited toroidal coupling, 94 mode pairs were required to properly resolve the growth rates of moderate wavelength ballooning modes. Although increases in computer memory and speed will presumably improve the resolution limit, a more immediate solution is to improve the parallelisation of the code. There are several sophisticated numerical techniques implemented in similar spectral codes [72]: given enough time these could be reimplemented, or even reused if co-operation was established.

It is also clear that there is a need for further study and hopefully improvement of the accuracy of the code: although the eigenmodes and stability behaviour predicted by the code are qualitatively correct for the testcases under consideration, and show very good convergence and accuracy for one-dimensional cases, some of the calculated 2-D growth rates were only approximately correct, even though the convergence was still fast. Generally accuracy can be improved in plasma codes by more explicitly separating the different physical wavemodes and the forces acting on them, so that cancellation can occur before approximation: there may be some progress to be made in this respect.

9.4 On semiclassical approaches to ballooning modes in 3D systems

There were basically two impediments to the semiclassical analysis of the drift stabilised ballooning equations in stellarators. The first was an incomplete understanding of how semiclassical analysis could be applied to this model, and the second was the additional complication of semiclassical chaos. We believe we have explored these difficulties in sufficient detail to confidently apply the semiclassical technique.

There are a couple of areas where the work could be extended. Firstly, for completeness, the cylindrical surfaces of the ballooning dispersion relation should also be quantised. Secondly, other fluid models may also be amenable to such an analysis. Thirdly, it would be intriguing to explore how the three dimensional effects transport wave energy between wavelengths and between locations in the plasma: this transport may be a rather fundamental difference between stellarators and tokamaks.

As an aside, it seems like the quadratic Lagrangian approach to the drift

stabilised ballooning problem given in section 8.4 could be the basis for a reasonably straightforward numerical formulation of linearised drift stabilised MHD analysis: this polynomial Hermitian eigenvalue problem could be solved using a technique from [49], for example.

References

- [1] Riemann, A., Ku, L., Monticello, D., Hirshman, S., Hudson, S., Kessel, C., Lazarus, E., Mikkelsen, D., Zarnstorff, M., Berry, L. A., Boozer, A., Brooks, A., Cooper, W. A., Drevlak, M., Fredrickson, E., Fu, G., Goldston, R., Hatcher, R., Isaev, M., Jun, C., Knowlton, S., Lewandowski, J., Lin, Z., Lyon, J. F., Merkel, P., Mikhailoc, M., Miner, W., Mynick, H., Neilson, G., Nelson, B. E., Nührenburg, C., Pomphrey, M., Redi, M., Reiersen, W., Rutherford, P., Sanchez, R., Schmidt, J., Spong, D., Strickler, D., Subbotin, A., Valanju, P., and White, R., *Physics of Plasmas*, **8**, 2083–2094 (2001).
- [2] Anderson, D. V., Cooper, A., Schwenn, U., and Gruber, R., “Linear MHD Stability Analysis of Toroidal 3D Equilibria with TERPSICHORE,” in *Theory of Fusion Plasmas*, edited by J. Vaclavic, F. Troyon, and E. Sindoni, Societa Italiana di Fisica (Bologna), 1988, pp. 93–102.
- [3] Kerner, W., Goedbloed, J. P., Huysmans, G. T. A., Poedts, S., and Schwarz, E., *Journal of Computational Physics*, **142**, 271–303 (1998).
- [4] Schwab, C., “Ideal MHD in stellarators: global modes and local theory,” in *Theory of Fusion Plasmas*, edited by J. Vaclavic and E. Sindoni, Societa Italiana di Fisica (Bologna), 1992, pp. 93–102.
- [5] Bruno, O., and Laurence, P., *Comptes Rendus de L’Academie des Sciences, Serie i (Mathematique)*, **317**, 337–41 (1993).
- [6] Hirshman, S. P., and Betancourt, O., *Journal of Computational Physics*, **96**, 99–109 (1991).
- [7] Greenside, H. S., Reiman, A. H., and Salas, A., *Journal of Computational Physics*, **81**, 102–136 (1989).
- [8] Liang, Y., Ida, K., Kado, S., Watanabe, K. Y., Sakakibara, S., Yokoyama, M., Yamada, H., Komori, A., Narihara, K., Tanaka, K., Tokuzawa, T., Nagayama, Y., Nakamura, Y., Ohyabu, N., Kawahata, K., Sudo, S., and experimental group, L., *Plasma Physics and Controlled Fusion*, **44**, 1383–1392 (2002).
- [9] Furth, H. P., Killeen, J., Rosenbluth, M. N., and Coppi, B., *Plasma Physics and Controlled Nuclear Fusion Research*, vol. 1, IAEA, Vienna, 1966.
- [10] Greene, J. M., and Johnson, J. L., *Plasma Physics*, **10**, 729–741 (1968).

- [11] Bateman, G., *MHD Instabilities*, The MIT press, 1978.
- [12] Glasser, A. H., Greene, J. M., and Johnson, J. L., *Physics of Fluids*, **18**, 875–888 (1975).
- [13] Motojima, O., Yamada, H., Komori, A., and Kaneko, O., *Proceeding of the 14th International Stellarator Workshop* (2003).
- [14] Nevins, W. M., and Pearlstein, L. D., *Physics of Fluids*, **31**, 1988–1998 (1988).
- [15] Tang, W. M., Connor, J. W., and Hastie, R. J., *Nuclear Fusion*, **20**, 1439–1453 (1980).
- [16] Dewar, R. L., Cuthbert, P., and Ball, R., *Physical Review Letters*, **86**, 2321–2324 (2001).
- [17] Trefethen, L. N., Trefethen, A. E., Reddy, S. C., and Driscoll, T. A., *Science*, **261**, 578–584 (1993).
- [18] Trefethen, L. N., *SIAM Review*, **39**, 383–406 (1997).
- [19] Borba, D., Reidel, K. S., Kerner, W., Huysmans, G. T. A., Ottaviani, M., and Schmid, P. J., *Physics of Plasmas*, **1**, 3151–3160 (1994).
- [20] Cheremnykh, O. K., and Revenchuk, S. M., *Plasma Physics and Controlled Fusion*, **34**, 55–75 (1992).
- [21] Aurich, R., Sieber, M., and Steiner, F., *Physical Review Letters*, **61**, 483–487 (1988).
- [22] Cvitanović, P., Artuso, R., Mainieri, R., Tanner, G., and Vattay, G., *Chaos: Classical and Quantum*, Niels Bohr Institute, Copenhagen, 2003, chaosBook.org.
- [23] C.Ellegard, Guhr, T., Lindemann, K., Nygørd, J., and Oxborrow, M., *Physical Review Letters*, **77**, 4918–4921 (1996).
- [24] Bohigas, O., Haq, R. U., and Pandley, A., “Fluctuation properties of nuclear energy levels and widths: comparison of theory with experiments,” in *Nuclear Data for Science and Technology*, edited by K. Böckhoff, Reidel Dordrecht, 1983.
- [25] Dewar, R. L., and Hudson, S. R., *Physica D*, **112**, 275–280 (1998).

- [26] Dewar, R. L., Nührenberg, C., and Tatsuno, T., *Journal of Plasma Fusion Research SERIES*, in press. E-Print arXiv:physics/0409070 (2004), proceedings of the 13th International Toki Conference, Toki, Japan, 9-12 December 2003.
- [27] McMillan, B. F., Dewar, R. L., and Storer, R. G., *Plasma Physics and Controlled Fusion*, **46**, 1027–1038 (2004).
- [28] Davies, B., *Phys. Letters*, **100A**, 144–148 (1984).
- [29] Dewar, R. L., and Davies, B., *Journal of Plasma Physics*, **32**, 443–461 (1984).
- [30] Ryu, C. M., and Grimm, R. C., *Journal of Plasma Physics*, **32**, 207–237 (1984).
- [31] Kerner, W., Lerbinger, K., and Reidel, K., *Physics of Fluids*, **29**, 2975–2987 (1986).
- [32] Storer, R. G., *Plasma Physics*, **25**, 1279–1282 (1983).
- [33] Freidberg, J. P., *Ideal Magnetohydrodynamics*, Plenum Press, New York, 1987, 1st edn.
- [34] Kerner, W., Lerbinger, K., Gruber, R., and Tsunematsu, R., *Computer Physics Communications*, **36**, 225–240 (1985).
- [35] Tayler, R. J., *Reviews of Modern Physics*, **32**, 907–913 (1960).
- [36] Breus, S. M., *Zh. Tech. Fiz.*, **30**, 1030–1034 (1960).
- [37] Berk, H. L., and Pfirsch, D., *Journal of Mathematical Physics*, **21**, 2054–2066 (1980).
- [38] Abrahamowitz, M., and Stegun, I. A., *Handbook of Mathematical Functions*, Dover Publications, New York, 1965, 9th edn.
- [39] Hender, T. C., Carreras, B. A., Cooper, W. A., Holmes, J. A., Diamond, P. H., and Similon, P. L., *Physics of Fluids*, **27**, 1439–1448 (1984).
- [40] Sugiyama, L. E., Park, W., Straus, H. R., Hudson, S. R., Stutman, D., and Tang, X.-Z., *Nuclear Fusion*, pp. 739–746 (2001).
- [41] Riemann, A., Ku, L., Monticello, D., and Hirshman, S., *Physics of Plasmas*, **8**, 2083–2094 (2001).

- [42] D'haeseleer, W. D., Hitchon, W. N. G., Callen, J. D., and Shohet, J. L., *Flux Coordinates and Magnetic Field Structure: a Guide to a Fundamental tool of Plasma Theory*, Springer-Verlag, New York, 1991.
- [43] Boozer, A. H., *Physics of Fluids*, **24**, 1999–2003 (1981).
- [44] Seiwald, B., Leitold, G., Kernbichler, W., and Kasilic, S. V. (2001).
- [45] Zienkiewicz, O. C., and Taylor, R. L., *The finite element method*, McGraw-Hill, London, 1991.
- [46] Gruber, R., and Rappaz, J., *Finite Element Methods in Linear Ideal Magnetohydrodynamics*, Springer-Verlag, New York, 1985.
- [47] Nakamura, Y., Matsumoto, T., Wakatani, M., Galkin, S. A., Drozdov, V. V., Martynov, A. A., Poshekhonov, Y. Y., Ichiguchi, K., Garcia, L., Carreras, B. A., Nührenberg, C., Cooper, W. A., and Johnson, J. L., *Journal of Computational Physics*, **128**, 43–57 (1996).
- [48] Sleijpen, G. L. G., and van der Vorst, H. A., *SIAM journal of matrix analysis*, **17**, 401–425 (1996).
- [49] Bai, Z., Demmel, J., Dongarra, J., Ruh, A., and van der Vorst, H., editors, *Templates for the Solution of Algebraic Eigenvalue Problems: A Practical Guide.*, SIAM, Philadelphia, 2000.
- [50] Dorsselaar, J. L. M., *SIAM Journal on Scientific Computing*, **24**, 1031–1053 (2002).
- [51] Solovév, L. S., *Soviet Physics - JETP*, **26**, 400–407 (1968).
- [52] Schellhase, A. R., and Storer, R. G., *Journal of Computational Physics*, **123**, 15–31 (1995).
- [53] Todd, A. M. M., Chance, M. S., Greene, J. M., Johnson, J. L., and Manickam, J., *Physical Review Letters*, **38**, 826–829 (1977).
- [54] Bateman, G., and Peng, Y. K. M., *Physical Review Letters*, **38**, 829–832 (1977).
- [55] Matsuoka, K., Miyamoto, K., Ohasa, K., and Wakatani, M., *Nuclear Fusion*, **17**, 1123–1131 (1977).
- [56] Matsumoto, T., Nakamura, Y., and Wakatani, M., *Nuclear Fusion*, **36**, 1571–1582 (1996).
- [57] Dewar, R. L., and Glasser, A. H., *Physics of Fluids*, **26**, 3038 (1983).

- [58] Main, J., and Wunner, G., *Physical Review Letters*, **82**, 3038–3041 (1999).
- [59] P.Cuthbert, and Dewar, R., *Physics of Plasmas*, **7**, 2302–2305 (2000).
- [60] Tang, W. M., Dewar, R. L., and Manickam, J., *Nuclear Fusion*, **22**, 1079–1081 (1982).
- [61] Low, F. E., *Proceeding of the Royal Society of London. Series A, Mathematical and Physical Sciences*, **248**, 282–287 (1958).
- [62] Brizard, A. J., *Physics of Plasmas*, **7**, 4816–4822 (2000).
- [63] Goldstein, H., *Classical Mechanics*, Addison-Wesley, 1953.
- [64] Gutzwiller, M. C., *Chaos in Classical and Quantum Mechanics*, Springer-Verlag, 1990.
- [65] de Almeida, O., *Hamiltonian Systems: Chaos and Quantisation*, Cambridge University Press, 1988.
- [66] Tomsovic, S., Grinberg, M., and Ullmo, D., *Physical Review Letters*, **75**, 4346–4349 (1995).
- [67] Dewar, R. L., Grimm, R. C., Johnson, J. L., Frieman, E. A., Greene, J. M., and Rutherford, P. H., *Physics of Fluids*, **17**, 930–938 (1974).
- [68] Berry, M. V., and Tabor, M., *Proceedings of the Royal Society of London. Series A, Mathematical and Physical Sciences*, **349**, 101–123 (1976).
- [69] McMillan, B. F., Blackwell, B. D., and Harris, J. H., *Nuclear Fusion*, **42**, 383–387 (2002).
- [70] Blackwell, B. D., McMillan, B. F., Searle, A. C., and Gardner, H. J., *Computer Physics Communications*, **142**, 243–247 (2001).
- [71] Cooper, W. A., Singleton, D. B., and Dewar, R. L., *Physics of Plasmas*, **3**, 275 (1996).
- [72] Nool, M., and van der Ploeg, A., *SIAM journal on Scientific Computing*, **22**, 95–112 (2000).
- [73] Jensen, R. V., *Nature*, **355**, 311–317 (1992).
- [74] Arnold, V. I., *Mathematical Methods in Classical Mechanics*, Springer-Verlag, 1978.
- [75] Berry, M. V., and Tabor, M., *Journal of Physics A: Mathematical and General*, **10**, 371–379 (1977).

- [76] Greene, J. M., and Johnson, J. L., *Physics of Fluids*, **5**, 510–517 (1962).
- [77] Kang, B. K., Lichtenberg, A. J., and Nevins, W. M., *Physics of Fluids*, **30**, 1416–1428 (1987).
- [78] Dewar, R. L., Manickam, J., Grimm, R. C., and Chance, M. S., *Nuclear Fusion*, **21**, 493–498 (1981).
- [79] Charlton, L. A., Leboeuf, J. N., and Lynch, V. E., *Physics of Fluids B*, **3**, 2028–2037 (1991).
- [80] Grimm, R. C., Dewar, R. L., and Manickam, J., *Journal of Computational Physics*, **49**, 94–117 (1983).
- [81] Hughes, M. H., Phillips, M. W., and Storer, R. G., *Computer Physics Communications*, **72**, 76–95 (1992).
- [82] Ichiguchi, K., Nakamura, Y., Wakatani, M., Yanagi, N., and Morimoto, S., *Nuclear Fusion*, **29**, 2093–2106 (1989).
- [83] Ichiguchi, K., Nakajima, N., Okamoto, M., Nakamura, Y., and Wakatani, M., *Nuclear Fusion*, **33**, 481–492 (1993).
- [84] Johnson, J. L., Ichiguchi, K., Nakamura, Y., , M. Okamoto, M. W., and Nakajima, N., *Physics of Plasmas*, **6**, 2513–2522 (1999).
- [85] Garcia, L., Sanchez, R., and Jimenez, J. A., *Journal of Plasma Fusion research*, **1**, 468–471 (1998).
- [86] Ichiguchi, K., Nakamura, Y., and Wakatani, M., *Nuclear Fusion*, **31**, 2073–2085 (1991).
- [87] Tatsuno, T., Wakatani, M., and Ichiguchi, K., *Nuclear Fusion*, **39**, 1391–1402 (1999).
- [88] Solovév, L. S., *Soviet Physics JETP*, **26**, 400–407 (1968).
- [89] Miura, H., Hayashi, T., and Sato, T., *Physics of Plasmas*, **8**, 4870–4878 (2001).
- [90] Wakatani, M., Nakamura, Y., Kondo, K., Nakasuga, M., Besshou, S., Obiki, T., Sano, F., Hanatani, K., Mizuuchi, T., Okada, H., Nagasaki, K., Inoue, N., and Yokoyama, M., *Nuclear Fusion*, **40**, 569–573 (2000).
- [91] Saad, Y., and Schultz, M. H., *SIAM Journal on Scientific and Statistical Computing*, **7**, 856–869 (1986).

- [92] Storer, R. G., and Gardner, H. J., *Computer Physics Communications*, **142**, 343–348 (2001).
- [93] Cuthbert, P., Lewandowski, J. L. V., Gardner, H. J., Pearson, M., Singleton, D. B., Dewar, R. L., Nakajima, N., and Cooper, W. A., *Physics of Plasmas*, **5**, 2921–2931 (1998).
- [94] Yamagishi, O., Nakamura, Y., Kondo, K., and Nakajima, N., *Physics of Plasmas*, **9**, 3429–3439 (2002).
- [95] W VII-A Team, *Nuclear Fusion*, **20**, 1093–1100 (1980).
- [96] Yamagishi, O., Nakamura, Y., and Kondo, K., *Physics of Plasmas*, **8**, 2750–2759 (2001).
- [97] Wolfram, S., *The Mathematica Book*, Wolfram Media/Cambridge University Press, Champagne, Illinois, 1996, 3rd edn.
- [98] Bernstein, I. B., *Physics of Fluids*, **18**, 320–324 (1975).
- [99] Cheng, C. Z., Chen, L., and Chance, M. S., *Annals of Physics*, **161**, 21–47 (1985).
- [100] Kaiser, R., *Nuclear Fusion*, **33**, 1281–1291 (1993).
- [101] Nakajima, N., *Physics of Plasmas*, **3**, 4545–4555 (1996).
- [102] Nakajima, N., *Physics of Plasmas*, **3**, 4556–4567 (1996).
- [103] Depassier, M. C., and Cooper, W. A., *Physics of Fluids*, **29**, 1948–1958 (1986).
- [104] Rewoldt, G., Wakatani, M., and Johnson, J. L., *Plasma Physics and Controlled Fusion*, **29**, 1643–1652 (1987).
- [105] Betancourt, O., Hernegger, F., Merkel, P., J. Nührenburg, R. G., and Troyon, F., *Journal of Computational Physics*, **52**, 187–197 (1983).
- [106] Dewar, R. L., *Journal of Plasma and Fusion Research (japan..)*, **73**, 1123–1134 (1997).
- [107] McMillan, B. F., and Storer, R. G., “Resistive Magnetohydrodynamic Stability for Helical Plasmas,” in *Theory of Fusion Plasmas*, edited by O. S. J. W. Connor and E. Sindoni, Societa Italiana di Fisica (Bologna), submitted 2004.
- [108] Dewar, R. L., Tatsuno, T., Nührenburg, C., and McMillan, B. F., *Physical Review E* (submitted 2004).

- [109] Hain, K., and Lüst, R., *Zeitschrift Naturforsch. A*, **13**, 936–940 (1958).
- [110] G. T. A. Huysmans, J. P. G., and Kerner, W., *Physics of Fluids B*, **5**, 1545–1558 (1993).
- [111] van der Holst, B., Beliën, A. J. C., Goedbloed, J. P., Nool, M., and van der Ploeg, A., *Physics of Plasmas*, **6**, 1554–1561 (1999).
- [112] McMillan, B. F., Dewar, R. L., and Storer, R. G., *AIP. American Institute of Physics Conference Proceedings*, **669**, 577–580 (2003).
- [113] Storer, R. G., and McMillan, B., *Proceedings of the 28th European Physical Society Conference on Controlled Fusion and Plasma Physics* (2003).
- [114] Storer, R. G., Gardner, H. J., and McMillan, B., *Proceedings of the 28th European Physical Society Conference on Controlled Fusion and Plasma Physics* (2001).
- [115] Storer, R. G., and McMillan, B., “Resistive stability for stellarators,” in *Theory of Fusion Plasmas*, edited by J. W. Connor, O. Sauter, and E. Sindoni, Societa Italiana di Fisica (Bologna), 2002, pp. 303–308.

A The matrix elements of Spector3D

We list the coupling terms which comprise the matrices **A** and **B** in terms of the equilibrium quantities. The mode numbers of the relevant weighting and variable elements are (\hat{m}, \hat{n}) and (m, n) , corresponding to the coefficients of $\exp(-i\hat{m}\theta + i\hat{n}\zeta)$ and $\exp(im\theta - in\zeta)$ respectively. The general term is

$$\{A_{ij}, B_{ij}\} = \int ds d\theta d\zeta \hat{f}_i e^{-i\hat{m}\theta + i\hat{n}\zeta} (\text{equi})_{ij} f_j e^{im\theta - in\zeta}, \quad (178)$$

The indices i and j here run from 1 to 7 corresponding to the variables $v_1, v_2, v_3, p, b_1, b_2$ and b_3 . The terms $(\text{equi})_{ij}$ are dependent on the equilibrium shaping and on surface quantities. The finite elements are

$$\hat{f} \in [h, h', H, H'] \quad \text{with} \quad H' = \frac{dH}{ds}, h' = \frac{dh}{ds} \quad \text{and} \quad (179)$$

$$f \in [k, k', K, K'] \quad \text{with} \quad K' = \frac{dK}{ds}, k' = \frac{dk}{ds}. \quad (180)$$

with $\{H, K\}$ corresponding to quadratic finite elements, and $\{h, k\}$ corresponding to cubic elements. We have suppressed for simplicity the radial grid number and the two finite elements at each grid point.

Because the matrix elements which result from finite element analysis in this complex geometry involve fairly complicated equilibrium coupling, the use of the symbolic mathematics program *Mathematica* [97] considerably eased the burden of code implementation. Because it reduces the number of symbolic calculations which have to be performed by hand, it also reduces the likelihood of some kinds of coding errors.

The next few pages show how a mathematica notebook can be used to generate these matrix elements: this notebook is a little tidier than the one actually used for software development, and for the sake of brevity, only a few matrix elements are shown in FORTRAN output form.

In[49]:=

Out[49]=

In[50]:= (* The integrated, linearised,
Resistive MHD equations in an explicit vector component form. The perturbations
to the equilibrium are Fourier transformed, as are the weighting vectors. *)

In[51]:= (* We have only extracted a couple of example terms
in final Fortran form for the sake of brevity. Otherwise,
the symbolic calculation is here in full. Lower case vector quantities
are covariant vectors, or operators with covariant results. Upper case
for contravariant. Vector indices run (1,2,3) on (p,theta,zeta). *)

In[52]:= Off[General::spell]

In[53]:= SetOptions[{\$Output, PageWidth->WindowWidth};

In[54]:= (* The Metric tensor g (which is a lowering operator). $g_{ij} = e_i \cdot e_j$ *)
g[r_, t_, z_] := {{gcomp[1, 1, r, t, z] J[r, t, z],
gcomp[1, 2, r, t, z] J[r, t, z], gcomp[1, 3, r, t, z] J[r, t, z]},
{gcomp[1, 2, r, t, z] J[r, t, z], gcomp[2, 2, r, t, z] J[r, t, z],
gcomp[2, 3, r, t, z] J[r, t, z]}, {gcomp[1, 3, r, t, z] J[r, t, z],
gcomp[2, 3, r, t, z] J[r, t, z], gcomp[3, 3, r, t, z] J[r, t, z]}}

In[55]:= (* Differential and vector operators. Jacobian $J = \text{Sqrt}(\text{Det}[g])$ *)

In[56]:= cros[A_, B_, r_, t_, z_] := {A[[2]]*B[[3]] - A[[3]]*B[[2]],
A[[3]]*B[[1]] - A[[1]]*B[[3]],
A[[1]]*B[[2]] - A[[2]]*B[[1]]} * J[p, t, z]

In[57]:= Curl[a_, p_, t_, z_] := {D[a[[3]], t] - D[a[[2]], z],
D[a[[1]], z] - D[a[[3]], p],
D[a[[2]], p] - D[a[[1]], t]} / J[p, t, z]

In[58]:= grad[a_, p_, t_, z_] := {D[a, p], D[a, t], D[a, z]}

In[59]:= Div[a_, p_, t_, z_] :=
(D[J[p, t, z] * a[[1]], p] + D[J[p, t, z] * a[[2]], t] + D[J[p, t, z] * a[[3]], z]) /
J[p, t, z]

In[60]:= (* Magnetic field in straight field line coordinates - note BT =
deriv of poloidal flux/2 pi,
BZ = deriv of toroidal flux/2 pi*)
B[p, t, z] := {0, BT[p], BZ[p]} / J[p, t, z]

In[61]:= (* perturbed quantities Vprime, aprime,
pprime and weighting quantities Vprimel, Aprimel, pprimel
in Fourier representation. *)

In[62]:= pprime[p, t, z] := press[p] * Exp[I*m*t - I*n*z]

In[63]:= pprimel[p, t, z] := pressl[p] * Exp[-I*mp*t + I*np*z]

In[64]:= (* One velocity component is aligned with the magnetic field. *)

In[65]:= Vprime[p, t, z] := (B[p, t, z] * J[p, t, z] * V3[p] + {0, 1, 0} V2[p] + V1[p] * {1, 0, 0}) *
Exp[I*m*t - I*n*z] / J[p, t, z]

In[66]:= Vprimel[p, t, z] :=
(B[p, t, z] * J[p, t, z] * V3l[p] + {0, 1, 0} V2l[p] + V1l[p] * {1, 0, 0}) *
Exp[-I*mp*t + I*np*z]

```

In[67]:= aprime[p, t, z] := {a1[p], a2[p], a3[p]} * Exp[I*m*t - I*n*z]

In[68]:= Aprime1[p, t, z] := {A11[p], A21[p], A31[p]} * Exp[-I*mp*t + I*np*z]

In[69]:= (*Current in explicit contravariant form. As with magnetic field,
JT = deriv of poloidal current flux/2 pi,
JZ = deriv of toroidal current flux/2 pi *)

Jc[p, t, z] := {0, JT[p] * delta[t, z] - D[nu[p, t, z], z],
JZ[p] * delta[t, z] + D[nu[p, t, z], t]} / J[p, t, z]

In[70]:= (* Equation of motion. The only nonzero contribution to the integral comes from
Fourier components of the equilibrium which have the form
Exp[I*(mp-m)*t - I*(np-n)*z]. *)

EqOfMotionRHS = Simplify[J[p, t, z] * (
-Curl[aprime[p, t, z], p, t, z].
(G[p, t, z].Curl[cros[Vprime1[p, t, z], B[p, t, z], p, t, z], p, t, z])
+ Vprime1[p, t, z].cros[Jc[p, t, z], Curl[aprime[p, t, z], p, t, z], p, t, z]
- Vprime1[p, t, z].grad[pprime[p, t, z], p, t, z] )];

In[71]:= EqOfMotionFourierRHS = Simplify[EqOfMotionRHS * Exp[I*(mp-m)*t - I*(np-n)*z]]

Out[71]= mp n a1[p] BT[p] gcomp[1, 2, p, t, z] V11[p] -
n np a1[p] BZ[p] gcomp[1, 2, p, t, z] V11[p] +
m np a1[p] BT[p] gcomp[1, 3, p, t, z] V11[p] -
m np a1[p] BZ[p] gcomp[1, 3, p, t, z] V11[p] - i m a1[p] delta[t, z] JT[p] V11[p] +
i n a1[p] delta[t, z] JZ[p] V11[p] - n np a1[p] BZ[p] gcomp[2, 2, p, t, z] V21[p] -
m np a1[p] BZ[p] gcomp[2, 3, p, t, z] V21[p] -
m np a1[p] BZ[p] gcomp[2, 3, p, t, z] V21[p] -
m np a1[p] BZ[p] gcomp[3, 3, p, t, z] V21[p] - i m J[p, t, z] press[p] V21[p] -
i m BT[p] J[p, t, z] press[p] V31[p] + i n BZ[p] J[p, t, z] press[p] V31[p] +
i m p BT[p] gcomp[1, 3, p, t, z] V11[p] a2'[p] -
i n p BZ[p] gcomp[1, 3, p, t, z] V11[p] a2'[p] +
delta[t, z] JT[p] V11[p] a2'[p] - i n p BZ[p] gcomp[2, 3, p, t, z] V21[p] a2'[p] -
i m p BZ[p] gcomp[3, 3, p, t, z] V21[p] a2'[p] -
i m p BT[p] gcomp[1, 2, p, t, z] V11[p] a3'[p] +
i n p BZ[p] gcomp[1, 2, p, t, z] V11[p] a3'[p] +
delta[t, z] JZ[p] V11[p] a3'[p] + i n p BZ[p] gcomp[2, 2, p, t, z] V21[p] a3'[p] +
i m p BZ[p] gcomp[2, 3, p, t, z] V21[p] a3'[p] -
i n a1[p] gcomp[2, 2, p, t, z] V11[p] BT'[p] -
i m a1[p] gcomp[2, 3, p, t, z] V11[p] BT'[p] + gcomp[2, 3, p, t, z] V11[p] a2'[p] BT'[p] -
gcomp[2, 2, p, t, z] V11[p] a3'[p] BT'[p] - i n a1[p] gcomp[2, 3, p, t, z] V11[p] BZ'[p] -
i m a1[p] gcomp[3, 3, p, t, z] V11[p] BZ'[p] +
gcomp[3, 3, p, t, z] V11[p] a2'[p] BZ'[p] - gcomp[2, 3, p, t, z] V11[p] a3'[p] BZ'[p] -
J[p, t, z] V11[p] press'[p] - i n a1[p] BT[p] gcomp[2, 2, p, t, z] V11'[p] -
i m a1[p] BT[p] gcomp[2, 3, p, t, z] V11'[p] -
i n a1[p] BZ[p] gcomp[2, 3, p, t, z] V11'[p] -
i m a1[p] BZ[p] gcomp[3, 3, p, t, z] V11'[p] +
BT[p] gcomp[2, 3, p, t, z] a2'[p] V11'[p] + BZ[p] gcomp[3, 3, p, t, z] a2'[p] V11'[p] -
BT[p] gcomp[2, 2, p, t, z] a3'[p] V11'[p] - BZ[p] gcomp[2, 3, p, t, z] a3'[p] V11'[p] +
i m a1[p] V11[p] nu(0,0,1)[p, t, z] - V11[p] a2'[p] nu(0,0,1)[p, t, z] +
i n a1[p] V11[p] nu(0,1,0)[p, t, z] + V11[p] a3'[p] nu(0,1,0)[p, t, z] +
n a2[p] (BZ[p] (np gcomp[1, 1, p, t, z] V11[p] + np gcomp[1, 2, p, t, z] V21[p] +
mp gcomp[1, 3, p, t, z] V21[p] - i delta[t, z] JT[p] V31[p] +
i gcomp[1, 3, p, t, z] V11'[p] + i V31[p] nu(0,0,1)[p, t, z]) +
i (delta[t, z] JZ[p] V21[p] + gcomp[1, 2, p, t, z] V11[p] BT'[p] +
gcomp[1, 3, p, t, z] V11[p] BZ'[p] + V21[p] nu(0,1,0)[p, t, z]) +
BT[p] (-mp gcomp[1, 1, p, t, z] V11[p] + i (delta[t, z] JZ[p] V31[p] +
gcomp[1, 2, p, t, z] V11'[p] + V31[p] nu(0,1,0)[p, t, z])) +
m a3[p] (BZ[p] (np gcomp[1, 1, p, t, z] V11[p] + np gcomp[1, 2, p, t, z] V21[p] +
mp gcomp[1, 3, p, t, z] V21[p] - i delta[t, z] JT[p] V31[p] +
i gcomp[1, 3, p, t, z] V11'[p] + i V31[p] nu(0,0,1)[p, t, z]) +
i (delta[t, z] JZ[p] V21[p] + gcomp[1, 2, p, t, z] V11[p] BT'[p] +
gcomp[1, 3, p, t, z] V11[p] BZ'[p] + V21[p] nu(0,1,0)[p, t, z]) +
BT[p] (-mp gcomp[1, 1, p, t, z] V11[p] + i (delta[t, z] JZ[p] V31[p] +
gcomp[1, 2, p, t, z] V11'[p] + V31[p] nu(0,1,0)[p, t, z]))

```

```

In[72]:= EqOfMotionFourierLHS = Simplify[J[p, t, z] *
Vprime1[p, t, z].g[p, t, z].Vprime[p, t, z] * Exp[I * (mp - m) * t - I * (np - n) * z]]

Out[72]= J[p, t, z] (gcomp[1, 1, p, t, z] V1[p] V11[p] +
gcomp[2, 2, p, t, z] V2[p] V21[p] + BZ[p] gcomp[1, 3, p, t, z] V11[p] V3[p] +
BT[p] gcomp[2, 2, p, t, z] V21[p] V3[p] + BZ[p] gcomp[2, 3, p, t, z] V21[p] V3[p] +
BZ[p] gcomp[1, 3, p, t, z] V1[p] V31[p] + BT[p] gcomp[2, 2, p, t, z] V2[p] V31[p] +
BZ[p] gcomp[2, 3, p, t, z] V2[p] V31[p] + BT[p]^2 gcomp[2, 2, p, t, z] V3[p] V31[p] +
2 BT[p] BZ[p] gcomp[2, 3, p, t, z] V3[p] V31[p] +
BZ[p]^2 gcomp[3, 3, p, t, z] V3[p] V31[p] +
gcomp[1, 2, p, t, z] (V11[p] (V2[p] + BT[p] V3[p]) + V1[p] (V21[p] + BT[p] V31[p])))

In[73]:= (* An example term *)

In[74]:= Expand[Coefficient[EqOfMotionFourierRHS, V11[p] a2[p]]]

Out[74]= -mp n BT[p] gcomp[1, 1, p, t, z] + n np BZ[p] gcomp[1, 1, p, t, z] +
i n gcomp[1, 2, p, t, z] BT'[p] + i n gcomp[1, 3, p, t, z] BZ'[p]

In[75]:= (* We need to replace symbolic derivatives
before we can produce explicit FORTRAN code *)

In[76]:= Bderivlist =
{D[BT[p], p] -> BTprime[p], D[BZ[p], p] -> BZprime[p], BT[p] -> BT[p], BZ[p] -> BZ[p]};

In[77]:= nulist = {nu^(1,0,0)[p, t, z] -> nu100[p, t, z],
nu^(0,1,0)[p, t, z] -> I np nu[p, t, z], nu^(0,0,1)[p, t, z] -> -I np nu[p, t, z]};

In[78]:= SetOptions[$Output, PageWidth -> 72];

In[79]:= (* Next line produces FORTRAN 77
Code: default Mathematica setting is to use "-" sign for continuation
lines. Can use "-fpconstant" in Fortran compiler switches so that
integers like (0,1) are converted to (0.0 d0,1.0 d0). Mathematica
outputs short lines of code without mandatory FORTRAN 77 spaces,
so must be hand edited to add spaces. *)

In[80]:= FortranForm[
Expand[Coefficient[EqOfMotionFourierRHS /. Bderivlist /. nulist, V11[p] a1[p]]]
]

Out[80]//FortranForm=
mp*n*BT(p)*gcomp(1,2,p,t,z) - n*np*BZ(p)*gcomp(1,2,p,t,z) +
- m*mp*BT(p)*gcomp(1,3,p,t,z) - m*np*BZ(p)*gcomp(1,3,p,t,z) -
- (0,1)*n*BTprime(p)*gcomp(2,2,p,t,z) -
- (0,1)*m*BTprime(p)*gcomp(2,3,p,t,z) -
- (0,1)*n*BZprime(p)*gcomp(2,3,p,t,z) -
- (0,1)*m*BZprime(p)*gcomp(3,3,p,t,z) -
- (0,1)*m*delta(t,z)*JT(p) + (0,1)*n*delta(t,z)*JZ(p) -
- mp*n*nu(p,t,z) + m*np*nu(p,t,z)

In[81]:= SetOptions[$Output, PageWidth -> WindowWidth];

In[82]:= Simplify[Aprime1[p, t, z].aprime[p, t, z]]

Out[82]= e^i (m t - mp t + (-n - np) z) (a1[p] A11[p] + a2[p] A21[p] + a3[p] A31[p])

In[83]:= Simplify[Aprime1[p, t, z].(cros[Vprime[p, t, z], B[p, t, z], p, t, z])]

Out[83]= e^i (m t - mp t + (-n - np) z) (A31[p] BT[p] V1[p] + BZ[p] (-A21[p] V1[p] + A11[p] V2[p]))
J[p, t, z]

In[84]:= (* Ampere's law: a large number of terms are generated from the resistive term
(eta*Curl[Curl[a]]) because of the choice of representation of the
weighting vector of the vector potential. Using a covariant weighting
vector simplifies the equations (particularly the Laplacian term)
but leads to a polluted approximation of the ideal problem. *)
AmpereRHS = Simplify[Aprime1[p, t, z].(cros[Vprime[p, t, z], B[p, t, z], p, t, z]
+ g[p, t, z].Curl[g[p, t, z].Curl[aprime[p, t, z], p, t, z], p, t, z])];

In[85]:= AmpereFourierRHS = Expand[Simplify[AmpereRHS * Exp[I * (mp - m) * t - I * (np - n) * z]]]

```

$$\begin{aligned}
\text{Out}[85]= & -n^2 a1[p] A11[p] \text{gcomp}[1, 2, p, t, z]^2 - \\
& n^2 a2[p] A21[p] \text{gcomp}[1, 2, p, t, z]^2 - m n A21[p] a3[p] \text{gcomp}[1, 2, p, t, z]^2 - \\
& 2 m n a1[p] A11[p] \text{gcomp}[1, 2, p, t, z] \text{gcomp}[1, 3, p, t, z] - \\
& m n a2[p] A21[p] \text{gcomp}[1, 2, p, t, z] \text{gcomp}[1, 3, p, t, z] - \\
& m^2 A21[p] a3[p] \text{gcomp}[1, 2, p, t, z] \text{gcomp}[1, 3, p, t, z] - \\
& n^2 a2[p] A31[p] \text{gcomp}[1, 2, p, t, z] \text{gcomp}[1, 3, p, t, z] - \\
& m n a3[p] A31[p] \text{gcomp}[1, 2, p, t, z] \text{gcomp}[1, 3, p, t, z] - \\
& m^2 a1[p] A11[p] \text{gcomp}[1, 3, p, t, z]^2 - \\
& m n a2[p] A31[p] \text{gcomp}[1, 3, p, t, z]^2 - m^2 a3[p] A31[p] \text{gcomp}[1, 3, p, t, z]^2 + \\
& n^2 a1[p] A11[p] \text{gcomp}[1, 1, p, t, z] \text{gcomp}[2, 2, p, t, z] + \\
& n^2 a2[p] A21[p] \text{gcomp}[1, 1, p, t, z] \text{gcomp}[2, 2, p, t, z] + \\
& m n A21[p] a3[p] \text{gcomp}[1, 1, p, t, z] \text{gcomp}[2, 2, p, t, z] - \\
& m n a1[p] A21[p] \text{gcomp}[1, 3, p, t, z] \text{gcomp}[2, 2, p, t, z] + \\
& n^2 a1[p] A31[p] \text{gcomp}[1, 3, p, t, z] \text{gcomp}[2, 2, p, t, z] + \\
& 2 m n a1[p] A11[p] \text{gcomp}[1, 1, p, t, z] \text{gcomp}[2, 3, p, t, z] + \\
& m n a2[p] A21[p] \text{gcomp}[1, 1, p, t, z] \text{gcomp}[2, 3, p, t, z] + \\
& m^2 A21[p] a3[p] \text{gcomp}[1, 1, p, t, z] \text{gcomp}[2, 3, p, t, z] + \\
& n^2 a2[p] A31[p] \text{gcomp}[1, 1, p, t, z] \text{gcomp}[2, 3, p, t, z] + \\
& m n a3[p] A31[p] \text{gcomp}[1, 1, p, t, z] \text{gcomp}[2, 3, p, t, z] + \\
& m n a1[p] A21[p] \text{gcomp}[1, 2, p, t, z] \text{gcomp}[2, 3, p, t, z] - \\
& n^2 a1[p] A31[p] \text{gcomp}[1, 2, p, t, z] \text{gcomp}[2, 3, p, t, z] - \\
& m^2 a1[p] A21[p] \text{gcomp}[1, 3, p, t, z] \text{gcomp}[2, 3, p, t, z] + \\
& m n a1[p] A31[p] \text{gcomp}[1, 3, p, t, z] \text{gcomp}[2, 3, p, t, z] + \\
& m^2 a1[p] A11[p] \text{gcomp}[1, 1, p, t, z] \text{gcomp}[3, 3, p, t, z] + \\
& m n a2[p] A31[p] \text{gcomp}[1, 1, p, t, z] \text{gcomp}[3, 3, p, t, z] + \\
& m^2 a3[p] A31[p] \text{gcomp}[1, 1, p, t, z] \text{gcomp}[3, 3, p, t, z] + \\
& m^2 a1[p] A21[p] \text{gcomp}[1, 2, p, t, z] \text{gcomp}[3, 3, p, t, z] - \\
& m n a1[p] A31[p] \text{gcomp}[1, 2, p, t, z] \text{gcomp}[3, 3, p, t, z] + \\
& \frac{A31[p] \text{BT}[p] V1[p]}{J[p, t, z]} - \frac{A21[p] \text{BZ}[p] V1[p]}{J[p, t, z]} + \frac{A11[p] \text{BZ}[p] V2[p]}{J[p, t, z]} - \\
& i n A11[p] \text{gcomp}[1, 3, p, t, z] \text{gcomp}[2, 2, p, t, z] a1'[p] + \\
& i n A11[p] \text{gcomp}[1, 2, p, t, z] \text{gcomp}[2, 3, p, t, z] a1'[p] - \\
& i m A11[p] \text{gcomp}[1, 3, p, t, z] \text{gcomp}[2, 3, p, t, z] a1'[p] - \\
& i m A21[p] \text{gcomp}[2, 3, p, t, z]^2 a1'[p] + i n A31[p] \text{gcomp}[2, 3, p, t, z]^2 a1'[p] + \\
& i m A11[p] \text{gcomp}[1, 2, p, t, z] \text{gcomp}[3, 3, p, t, z] a1'[p] - \\
& i m A21[p] \text{gcomp}[2, 2, p, t, z] \text{gcomp}[3, 3, p, t, z] a1'[p] - \\
& i n A31[p] \text{gcomp}[2, 2, p, t, z] \text{gcomp}[3, 3, p, t, z] a1'[p] - \\
& i n A11[p] \text{gcomp}[1, 2, p, t, z] \text{gcomp}[1, 3, p, t, z] a2'[p] - \\
& i m A11[p] \text{gcomp}[1, 3, p, t, z]^2 a2'[p] - \\
& 2 i n A21[p] \text{gcomp}[1, 3, p, t, z] \text{gcomp}[2, 2, p, t, z] a2'[p] + \\
& 2 i n A11[p] \text{gcomp}[1, 1, p, t, z] \text{gcomp}[2, 3, p, t, z] a2'[p] + \\
& 2 i m A21[p] \text{gcomp}[1, 2, p, t, z] \text{gcomp}[2, 3, p, t, z] a2'[p] - \\
& i m A21[p] \text{gcomp}[1, 3, p, t, z] \text{gcomp}[2, 3, p, t, z] a2'[p] - \\
& i n A31[p] \text{gcomp}[1, 3, p, t, z] \text{gcomp}[2, 3, p, t, z] a2'[p] + \\
& i m A11[p] \text{gcomp}[1, 1, p, t, z] \text{gcomp}[3, 3, p, t, z] a2'[p] + \\
& i m A21[p] \text{gcomp}[1, 2, p, t, z] \text{gcomp}[3, 3, p, t, z] a2'[p] + \\
& i n A31[p] \text{gcomp}[1, 2, p, t, z] \text{gcomp}[3, 3, p, t, z] a2'[p] + \\
& i n A11[p] \text{gcomp}[1, 2, p, t, z]^2 a3'[p] + \\
& i m A11[p] \text{gcomp}[1, 2, p, t, z] \text{gcomp}[1, 3, p, t, z] a3'[p] - \\
& i n A11[p] \text{gcomp}[1, 1, p, t, z] \text{gcomp}[2, 2, p, t, z] a3'[p] - \\
& i m A21[p] \text{gcomp}[1, 3, p, t, z] \text{gcomp}[2, 2, p, t, z] a3'[p] - \\
& i n A31[p] \text{gcomp}[1, 3, p, t, z] \text{gcomp}[2, 2, p, t, z] a3'[p] - \\
& i m A11[p] \text{gcomp}[1, 1, p, t, z] \text{gcomp}[2, 3, p, t, z] a3'[p] + \\
& i m A21[p] \text{gcomp}[1, 2, p, t, z] \text{gcomp}[2, 3, p, t, z] a3'[p] + \\
& i n A31[p] \text{gcomp}[1, 2, p, t, z] \text{gcomp}[2, 3, p, t, z] a3'[p] - \\
& 2 i m A31[p] \text{gcomp}[1, 3, p, t, z] \text{gcomp}[2, 3, p, t, z] a3'[p] + \\
& 2 i m A31[p] \text{gcomp}[1, 2, p, t, z] \text{gcomp}[3, 3, p, t, z] a3'[p] + \\
& A11[p] \text{gcomp}[1, 3, p, t, z] \text{gcomp}[2, 3, p, t, z] a2''[p] + \\
& A21[p] \text{gcomp}[2, 3, p, t, z]^2 a2''[p] - \\
& A11[p] \text{gcomp}[1, 2, p, t, z] \text{gcomp}[3, 3, p, t, z] a2''[p] - \\
& A21[p] \text{gcomp}[2, 2, p, t, z] \text{gcomp}[3, 3, p, t, z] a2''[p] - \\
& A11[p] \text{gcomp}[1, 3, p, t, z] \text{gcomp}[2, 2, p, t, z] a3''[p] + \\
& A11[p] \text{gcomp}[1, 2, p, t, z] \text{gcomp}[2, 3, p, t, z] a3''[p] + \\
& A31[p] \text{gcomp}[2, 3, p, t, z]^2 a3''[p] - \\
& A31[p] \text{gcomp}[2, 2, p, t, z] \text{gcomp}[3, 3, p, t, z] a3''[p] + \\
& i n A11[p] a2[p] \text{gcomp}[1, 2, p, t, z] \text{gcomp}^{(0,0,0,0,1)}[1, 1, p, t, z] + \\
& i m A11[p] a3[p] \text{gcomp}[1, 2, p, t, z] \text{gcomp}^{(0,0,0,0,1)}[1, 1, p, t, z] +
\end{aligned}$$


```

A21[p] gcomp[1, 2, p, t, z] a3'[p] gcomp(0,0,0,1,0) [2, 3, p, t, z] -
A31[p] gcomp[1, 3, p, t, z] a3'[p] gcomp(0,0,0,1,0) [2, 3, p, t, z] -
i m a1[p] A11[p] gcomp[1, 1, p, t, z] gcomp(0,0,0,1,0) [3, 3, p, t, z] -
i m a1[p] A21[p] gcomp[1, 2, p, t, z] gcomp(0,0,0,1,0) [3, 3, p, t, z] -
i m a1[p] A31[p] gcomp[1, 3, p, t, z] gcomp(0,0,0,1,0) [3, 3, p, t, z] +
A11[p] gcomp[1, 1, p, t, z] a2'[p] gcomp(0,0,0,1,0) [3, 3, p, t, z] +
A21[p] gcomp[1, 2, p, t, z] a2'[p] gcomp(0,0,0,1,0) [3, 3, p, t, z] +
A31[p] gcomp[1, 3, p, t, z] a2'[p] gcomp(0,0,0,1,0) [3, 3, p, t, z] +
i n A11[p] a2[p] gcomp[1, 3, p, t, z] gcomp(0,0,1,0,0) [1, 2, p, t, z] +
i m A11[p] a3[p] gcomp[1, 3, p, t, z] gcomp(0,0,1,0,0) [1, 2, p, t, z] +
i n a2[p] A21[p] gcomp[2, 3, p, t, z] gcomp(0,0,1,0,0) [1, 2, p, t, z] +
i m A21[p] a3[p] gcomp[2, 3, p, t, z] gcomp(0,0,1,0,0) [1, 2, p, t, z] +
i n a2[p] A31[p] gcomp[3, 3, p, t, z] gcomp(0,0,1,0,0) [1, 2, p, t, z] +
i m a3[p] A31[p] gcomp[3, 3, p, t, z] gcomp(0,0,1,0,0) [1, 2, p, t, z] -
i n A11[p] a2[p] gcomp[1, 2, p, t, z] gcomp(0,0,1,0,0) [1, 3, p, t, z] -
i m A11[p] a3[p] gcomp[1, 2, p, t, z] gcomp(0,0,1,0,0) [1, 3, p, t, z] -
i n a2[p] A21[p] gcomp[2, 2, p, t, z] gcomp(0,0,1,0,0) [1, 3, p, t, z] -
i m A21[p] a3[p] gcomp[2, 2, p, t, z] gcomp(0,0,1,0,0) [1, 3, p, t, z] -
i n a2[p] A31[p] gcomp[2, 3, p, t, z] gcomp(0,0,1,0,0) [1, 3, p, t, z] -
i m a3[p] A31[p] gcomp[2, 3, p, t, z] gcomp(0,0,1,0,0) [1, 3, p, t, z] -
i n a1[p] A11[p] gcomp[1, 3, p, t, z] gcomp(0,0,1,0,0) [2, 2, p, t, z] -
i n a1[p] A21[p] gcomp[2, 3, p, t, z] gcomp(0,0,1,0,0) [2, 2, p, t, z] -
i n a1[p] A31[p] gcomp[3, 3, p, t, z] gcomp(0,0,1,0,0) [2, 2, p, t, z] -
A11[p] gcomp[1, 3, p, t, z] a3'[p] gcomp(0,0,1,0,0) [2, 2, p, t, z] -
A21[p] gcomp[2, 3, p, t, z] a3'[p] gcomp(0,0,1,0,0) [2, 2, p, t, z] -
A31[p] gcomp[3, 3, p, t, z] a3'[p] gcomp(0,0,1,0,0) [2, 2, p, t, z] +
i n a1[p] A11[p] gcomp[1, 2, p, t, z] gcomp(0,0,1,0,0) [2, 3, p, t, z] -
i m a1[p] A11[p] gcomp[1, 3, p, t, z] gcomp(0,0,1,0,0) [2, 3, p, t, z] +
i n a1[p] A21[p] gcomp[2, 2, p, t, z] gcomp(0,0,1,0,0) [2, 3, p, t, z] -
i m a1[p] A21[p] gcomp[2, 3, p, t, z] gcomp(0,0,1,0,0) [2, 3, p, t, z] +
i n a1[p] A31[p] gcomp[2, 3, p, t, z] gcomp(0,0,1,0,0) [2, 3, p, t, z] -
i m a1[p] A31[p] gcomp[3, 3, p, t, z] gcomp(0,0,1,0,0) [2, 3, p, t, z] +
A11[p] gcomp[1, 3, p, t, z] a2'[p] gcomp(0,0,1,0,0) [2, 3, p, t, z] +
A21[p] gcomp[2, 3, p, t, z] a2'[p] gcomp(0,0,1,0,0) [2, 3, p, t, z] +
A31[p] gcomp[3, 3, p, t, z] a2'[p] gcomp(0,0,1,0,0) [2, 3, p, t, z] +
A11[p] gcomp[1, 2, p, t, z] a3'[p] gcomp(0,0,1,0,0) [2, 3, p, t, z] +
A21[p] gcomp[2, 2, p, t, z] a3'[p] gcomp(0,0,1,0,0) [2, 3, p, t, z] +
A31[p] gcomp[2, 3, p, t, z] a3'[p] gcomp(0,0,1,0,0) [2, 3, p, t, z] +
i m a1[p] A11[p] gcomp[1, 2, p, t, z] gcomp(0,0,1,0,0) [3, 3, p, t, z] +
i m a1[p] A21[p] gcomp[2, 2, p, t, z] gcomp(0,0,1,0,0) [3, 3, p, t, z] +
i m a1[p] A31[p] gcomp[2, 3, p, t, z] gcomp(0,0,1,0,0) [3, 3, p, t, z] -
A11[p] gcomp[1, 2, p, t, z] a2'[p] gcomp(0,0,1,0,0) [3, 3, p, t, z] -
A21[p] gcomp[2, 2, p, t, z] a2'[p] gcomp(0,0,1,0,0) [3, 3, p, t, z] -
A31[p] gcomp[2, 3, p, t, z] a2'[p] gcomp(0,0,1,0,0) [3, 3, p, t, z]

```

In[86]:= (* An example term *)

In[87]:= Expand[Coefficient[AmpereFourierRHS, A31[p] a2[p]]]

```

Out[87]= -n2 gcomp[1, 2, p, t, z] gcomp[1, 3, p, t, z] -
m n gcomp[1, 3, p, t, z]2 + n2 gcomp[1, 1, p, t, z] gcomp[2, 3, p, t, z] +
m n gcomp[1, 1, p, t, z] gcomp[3, 3, p, t, z] +
i n gcomp[2, 3, p, t, z] gcomp(0,0,0,0,1) [1, 1, p, t, z] -
i n gcomp[1, 3, p, t, z] gcomp(0,0,0,0,1) [1, 2, p, t, z] -
i n gcomp[3, 3, p, t, z] gcomp(0,0,0,1,0) [1, 1, p, t, z] +
i n gcomp[1, 3, p, t, z] gcomp(0,0,0,1,0) [1, 3, p, t, z] +
i n gcomp[3, 3, p, t, z] gcomp(0,0,1,0,0) [1, 2, p, t, z] -
i n gcomp[2, 3, p, t, z] gcomp(0,0,1,0,0) [1, 3, p, t, z]

```

In[88]:= (* Compound metric tensor elements. All terms of a coupling element which have variation on a flux surface need to be grouped together, and reciprocals must be taken before the Fourier transform! *)

```

In[89]:= Rulecomp =
{gcomp[a_, b_, p, t, z] gcomp[c_, d_, p, t, z] → gcompprod[a, b, c, d, p, mnp, nnp],
gcomp[a_, b_, p, t, z]^2 → gcompprod[a, b, a, b, p, mnp, nnp],
gcomp[a_, b_, p, t, z] D[gcomp[c_, d_, p, t, z], p] →
gcompprodpp[a, b, c, d, p, mnp, nnp],
gcomp[a_, b_, p, t, z] D[gcomp[c_, d_, p, t, z], t] →
gcompprodtt[a, b, c, d, p, mnp, nnp], gcomp[a_, b_, p, t, z]
D[gcomp[c_, d_, p, t, z], z] → gcompprodzz[a, b, c, d, p, mnp, nnp],
g[a_, b_, p, t, z] g[c_, d_, p, t, z] → gprod[a, b, c, d, p, mnp, nnp],
g[a_, b_, p, t, z]^2 → gprod[a, b, a, b, p, mnp, nnp]}

Out[89]= {gcomp[a_, b_, p, t, z] gcomp[c_, d_, p, t, z] → gcompprod[a, b, c, d, p, mnp, nnp],
gcomp[a_, b_, p, t, z]^2 → gcompprod[a, b, a, b, p, mnp, nnp],
gcomp[a_, b_, p, t, z] gcomp(0,0,1,0,0)[c_, d_, p, t, z] →
gcompprodpp[a, b, c, d, p, mnp, nnp],
gcomp[a_, b_, p, t, z] gcomp(0,0,0,1,0)[c_, d_, p, t, z] →
gcompprodtt[a, b, c, d, p, mnp, nnp],
gcomp[a_, b_, p, t, z] gcomp(0,0,0,0,1)[c_, d_, p, t, z] →
gcompprodzz[a, b, c, d, p, mnp, nnp],
g[a_, b_, p, t, z] g[c_, d_, p, t, z] → gprod[a, b, c, d, p, mnp, nnp],
g[a_, b_, p, t, z]^2 → gprod[a, b, a, b, p, mnp, nnp]}

In[90]:= SetOptions[$Output, PageWidth → 72];

In[91]:= (* Next line produces FORTRAN 77 code *)

In[92]:= FortranForm[Expand[Coefficient[AmpereFourierRHS, A31[p] a2[p]]] /. Rulecomp]

Out[92]//FortranForm=
n**2*gcompprod(1,1,2,3,p,mnp,nnp) +
- m*n*gcompprod(1,1,3,3,p,mnp,nnp) -
- n**2*gcompprod(1,2,1,3,p,mnp,nnp) -
- m*n*gcompprod(1,3,1,3,p,mnp,nnp) -
- (0,1)*n*gcompprodpp(2,3,1,3,p,mnp,nnp) +
- (0,1)*n*gcompprodpp(3,3,1,2,p,mnp,nnp) +
- (0,1)*n*gcompprodtt(1,3,1,3,p,mnp,nnp) -
- (0,1)*n*gcompprodtt(3,3,1,1,p,mnp,nnp) -
- (0,1)*n*gcompprodzz(1,3,1,2,p,mnp,nnp) +
- (0,1)*n*gcompprodzz(2,3,1,1,p,mnp,nnp)

In[93]:= SetOptions[$Output, PageWidth → WindowWidth];

In[94]:= AmpereFourierLHS =
Simplify[Aprime1[p, t, z].Aprime[p, t, z] * Exp[I*(mp - m)*t - I*(np - n)*z]]

Out[94]= a1[p] All[p] + a2[p] A21[p] + a3[p] A31[p]

In[95]:= (*Equation of state *)
EqOfStateFourierRHS = Simplify[
pprime1[p, t, z] * (-J[p, t, z] * gamma * pressure0[p] * Div[Vprime[p, t, z], p, t, z] -
J[p, t, z] * grad[pressure0[p], p, t, z].Vprime[p, t, z]) *
Exp[I*(mp - m)*t - I*(np - n)*z]]

Out[95]= -press1[p] (V1[p] pressure0'[p] +
gamma pressure0[p] (i m V2[p] + i m BT[p] V3[p] - i n BZ[p] V3[p] + V1'[p]))

In[96]:= EqOfStateFourierLHS = Simplify[
pprime1[p, t, z] * J[p, t, z] * Aprime[p, t, z] * Exp[I*(mp - m)*t - I*(np - n)*z]]

Out[96]= J[p, t, z] press[p] press1[p]

```

B Splining of Equilibrium quantities

The equilibrium quantities output from the mapper are:

$$J, g_{11}, g_{12} = g_{21}, g_{22}, g_{23} = g_{32}, g_{31} = g_{13}, g_{33}, BZ, BT, JZ, JT \quad (181)$$

In the VMEC coordinate system where $s \simeq r^2$ the surface functions are smooth near the magnetic axis, and generally attain some finite value in the limit $r \rightarrow 0$. However, there are possible singularities in the metric tensor elements, particularly in g_{11} , which $\simeq 1/s$ in the limit. Also, $g_{22} \simeq s$, and to ensure accuracy near the origin, we would like to impose $g_{22}|_{s=0} = 0$. Accurate splining of such quantities can be achieved by using a test function; this is equivalent to splining the quantities sg_{11} and g_{22}/s instead of g_{11} and g_{22} .

In testing it has been found that splining the equation coefficients is more accurate than splining the equilibrium quantities; this is because some cancellation of the equilibrium quantities occurs when they are combined into coefficients at the equilibrium grid points. For each coefficient, we determine the leading power of s near the origin and divide this out, and then spline the regularised quantity using unsmoothed cubic splines. The power of s is then recombined.

It is often the case that the Boozer coordinate mapping of the output from the equilibrium code VMEC is not as accurate near the origin as elsewhere. It is sometimes helpful to extrapolate the offending splined quantities from the second or third grid point in order to account for this deviation. Also, in cases where there is no large mode amplitude expected near the axis, the first finite element grid point can be moved slightly away from $r = 0$ with a negligible effect on the predicted eigenfrequencies.

C Eigenvalue solvers for SPECTOR3D

For matrix eigenvalue problems, a direct evaluation of the complete set of eigenvalues and eigenvectors is possible through a diagonalisation technique. However for large problems this is often computationally infeasible and we must use an iterative technique to extract a small number of eigenvectors and eigenvalues. A useful resource for these iterative techniques is [49]. In order to keep the description of our code self contained, and to illustrate how our particular problem influences the choice of eigenvalue solver, we provide a description of the two techniques used in our code.

This is not the first implementation of these methods, but unfortunately as of the time of writing, there were no publicly available codes which suited our needs.

C.1 The Jacobi–Davidson eigenvalue solver: background and implementation

Even though various algorithms for extracting a small portion of the spectrum exist, the relatively new Jacobi–Davidson method [48] combines the most desirable features of these algorithms for our problem:

1. Convergence can be very fast (quadratic) under certain conditions.
2. It includes eigenvector deflation, allowing a significant number of eigenvectors to be found.
3. We can find interior eigenvalues without the need for exact matrix inverses, leading to potentially significant savings on computational resources.
4. It has a good track record for a closely related problem, the 2D linearised resistive MHD code CASTOR [3], where it was also shown to parallelise well.

The technique is a *subspace method*; at each step, the large matrix problem is represented in terms of small matrices acting on low dimensional subspaces and the projections between the full and restricted spaces. The eigenvalue problem can then be easily solved in the small dimensional subspace; the distinguishing feature of the Jacobi–Davidson method is the means used to refine this subspace.

Our problem is a generalised non-Hermitian eigenvalue problem, requiring the solution of

$$\lambda \mathbf{Bx} = \mathbf{Ax} \tag{182}$$

for complex matrices \mathbf{A}, \mathbf{B} , a complex vector \mathbf{x} , and complex λ . It is possible to deal directly with this generalised problem using a variant of the Jacobi–Davidson technique [49], or to convert the problem to a standard eigenvalue problem with a shifted eigenvalue. The disadvantage of converting to a standard eigenproblem is that we must then perform a complete LU decomposition of a matrix, which can be computationally costly. However, we have found this speed penalty is not terribly burdensome, as the most significant limitation seems to be memory requirements, rather than the patience of the investigator. Direct solution of the generalised problem requires considerably more implementation effort as a result of increased algorithmic complexity, especially since a good preconditioner must be found. We implemented the Jacobi–Davidson technique for standard non-Hermitian eigenvalue problems, as described in [49].

The algorithm in SPECTOR3D implements deflation and restart, and involves preconditioning in the inverse solver (using the Generalised Minimal RESidual (GMRES) method [91]), and can be found in pseudocode form as Algorithm 4.17 of [49]. However, the description here is limited to the Jacobi–Davidson method without deflation and restart, for pedagogical purposes: we would like to convey the flavour of the algorithm for those plasma physicists interested in similar problems.

Consider an eigenvalue problem $Au = \lambda u$. To gain an understanding of the Jacobi–Davidson method, we think about how we might refine an approximation u_k to an eigenvector u with eigenvalue λ . The approximation at step k to the eigenvalue λ is θ_k , which is found though $\theta_k = u_k^* A u_k / u_k^* u_k$. Because the magnitude of the eigenvector is irrelevant, there should be a correction, v , perpendicular to u_k which brings it into line with u . We are therefore interested in the projection of \mathbf{A} in this perpendicular direction, $B = (1 - u_k u_k^*) A (1 - u_k u_k^*)$. After some algebra we can find an relation for the correction in terms of the residual $r = Au_k - \theta_k u_k$ and B :

$$(B - \lambda I)v = -r \tag{183}$$

Because we do not know λ , we are forced to replace it by θ_k , the current guess for the eigenvalue. The vector v can then be found, and added to our search space.

The complete method is described by Algorithm 1 in [48]:

1. **Start:** Choose an initial nontrivial vector v
 - Compute $v_1 = v / \|v\|_2$, $w_1 = Av_1$, $h_1 1 = v_1^* w_1$, set $V_1 = [v_1]$, $W_1 = [w_1]$, $H_1 = [h_1 1]$, $u = v_1$, $\theta = h_1 1$, compute $r = w_1 - \theta u$.
2. **Iterate:** Until convergence do:

3. **Inner Loop:** For $k = 1, \dots, m - 1$ do:

- Solve (approximately) $t \perp u$,

$$(1 - uu^*)(A - \theta I)(I - uu^*)t = -r \quad (184)$$

- Orthogonalise t against V_k via modified Gram–Schmidt, and expand V_k with this vector to V_{k+1} .
- Compute $w_{k+1} := Av_{k+1}$ and expand W_k with this vector to W_{k+1} .
- Compute $V_{k+1}^* w_{k+1}$, the last column of $H_{k+1} := V_{k+1}^* A V_{k+1}$, and $v_{k+1}^* W_k$, the last row of H_{k+1} (only if $A \neq A^*$).
- Compute the largest eigenpair (θ, s) of H_{k+1} (with $\|s\|_2 = 1$).
- Compute the Ritz vector $u := V_{k+1}s$, compute $\hat{u} := Au$ ($= W_{k+1}s$), and the associated residual vector $r := \hat{u} - \theta u$.
- Test for convergence. Stop if satisfied.

4. **Restart:** Set $V_1 = [u]$, $W_1 = [\hat{u}]$, $H_1 = [\theta]$, and goto 3.

C.2 Convergence of the eigenvalue solvers.

We illustrate the convergence behaviour of the shift and invert and Jacobi–Davidson algorithms with a test case. The convergence of iterative techniques for non-symmetric problems is generically non-monotonic, and in strongly non-normal problems like resistive MHD, may be considerably slower than expected from simple estimates based on eigenvalue separation.

For the shift and invert solver, we can interpret the behaviour of the iterated approximate eigenvector by formally considering powers of $B(A - \lambda_0 B)^{-1}$. The long term dynamics of these iterates can be given in terms of the eigenvalues of this matrix. For a large number of iterations, n , we expect components in the direction of the largest eigenvector to dominate over the remaining components by $C(\|\lambda_0\|/\|\lambda_1\|)^n$, where λ_0 and λ_1 are the first and second largest eigenvalues, respectively. However, for strongly non-normal matrices, this asymptotic dominance may only occur for very large n , and there may be large transient growth of our iterated eigenvector in other directions [18].

In figure 47, we show a convergence plot for the two methods, used to find an eigenvalue of the resistive MHD spectrum of a simple cylindrical plasma. We should note that the number of iterations is not a good indication of the speed of these two algorithms: the computational expense of each iteration needs to be considered.

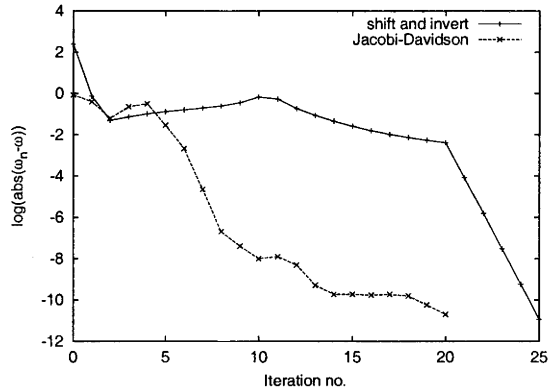


Figure 47: Convergence versus the number of iterations for a well isolated eigenvalue. For the invert and shift method, we choose an optimal shift every 20 iterations. The correction step in the Jacobi–Davidson technique uses 10 GMRES iterations.

For the iterate and shift algorithm, there is no convergence until about the tenth iteration, and fairly slow convergence until the twentieth iteration, where a new shift is applied based on the current approximate eigenvalue. After this shift there is very fast convergence, as the guess ($\omega \simeq 0.274$) is quite close to the true eigenvalue ($\omega \simeq 0.27$), and the corresponding eigenvalue in the shifted and inverted matrix is strongly dominant. It is important that the shift is not made after too few iterations or we may not find the eigenvalue closest to our guess; if we make a shift every 10 inner iterations, this example case converges to a different eigenvalue. The number of inner iterations needed depends both on the problem and the quality of the initial guess. We usually iterate the inner loop 50 times between shifts, which is almost always sufficient in practise.

In the Jacobi–Davidson algorithm, there has been considerable convergence within 10 steps, but the convergence then slows considerably. If we solve the correction equation exactly, we expect quadratic convergence, so slow convergence usually indicates that the correction equation is not being solved accurately. Nevertheless, we converge after 20 steps. The Jacobi–Davidson method almost never converges to a eigenvalue which is not the closest to our initial guess [49], unlike shift and invert, which can miss eigenvalues.

We usually find that shift and invert is the faster of the two algorithms, so this is usually the preferred choice for finding a single eigenvalue. However, being able to find a large number of eigenvalues around a particular point in the complex plane has been of considerable interest, and Jacobi–Davidson is very suitable for this purpose.

C.3 Storage costs and computational issues.

The total memory required to execute SPECTOR3D is strongly dependent on the resolution in radial and Fourier space. Almost all of the storage for a significant test case is consumed by the coupling matrices and the storage of matrix inverses. The coupling matrices are block tridiagonal with blocks of size $N \times N$, so that the full array is $nN \times nN$, where n is the number of radial grid points, and $N =$ number of Fourier modes \times finite elements per grid point \times number of scalar equations. For k Fourier modes, and our specific finite element scheme, $N = 14k$. There are $3n - 2$ blocks in each matrix. Each matrix element is represented by a double precision complex value, requiring 16 bytes of storage. The memory associated with storing each matrix is then $16(3n - 2)(14k)^2$ for k Fourier modes.

SPECTOR3D requires the calculation and storage of a matrix inverse. The original implementation of SPECTOR3D used a blockwise inversion, and the additional storage requirement is then $16(3n)(14k)^2$ leading to a total storage requirement of $16(9n - 2)(14k)^2$. However, we found that the LAPACK band inverse solver (in PZGBTRF and PZGBTRS) was capable of significantly more accurate inverses, which was important for the discrimination of modes with small growth rates. For band storage, we require somewhat more memory, and the total memory requirement is then approximately $16n(14[14k] - 1)(14k)$, an increase in memory requirement of approximately 50%.

Execution time can be divided into two parts: The time taken to set up the finite element coupling coefficients, and the time taken by the eigenvalue solver.

The finite element coupling coefficients took approximately 30 minutes to setup on a single processor for the largest job we have run to date (3GB). It took another 30 minutes to calculate a single eigenvector. The eigenvalue solver is not guaranteed to converge, however, and it is not possible to put an upper bound on the execution time.